# An Adaptive Moving Mesh Finite Element Method and Its Application to Mathematical Models from Physical Sciences and Image Processing

## Yufei Yu

Submitted to the graduate degree program in Department of Mathematics and the Graduate Faculty of the University of Kansas in partial fulfillment of the requirements for the degree of Doctor of Philosophy.

Committee members

<div style="text-align:right">

_____
Weizhang Huang, Chair

_____
Shawn Keshmiri

_____
Weishi Liu

_____
Xuemin Tu

_____
Erik Van Vleck

</div>

Date defended: _____ April 29, 2019

The Dissertation Committee for Yufei Yu certifies
that this is the approved version of the following dissertation :

An Adaptive Moving Mesh Finite Element Method and Its Application to Mathematical Models
from Physical Sciences and Image Processing

_____
Weizhang Huang, Chair

Date approved: _____
April 29, 2019

# Abstract

Moving sharp fronts are an important feature of many mathematical models from physical sciences and cause challenges in numerical computation. In order to obtain accurate solutions, a high resolution of mesh is necessary, which results in high computational cost if a fixed mesh is used. As a solution to this issue, an adaptive mesh method, which is called the moving mesh partial differential equation (MMPDE) method, is described in this work. The MMPDE method has the advantage of adaptively relocating the mesh points to increase the densities around sharp layers of the solutions, without increasing the mesh size. Moreover, this strategy can generate a nonsingular mesh even on non-convex and non-simply connected domains, given that the initial mesh is nonsingular. The focus of this thesis is on the application of the MMPDE method to mathematical models from physical sciences and image segmentation. In particular, this thesis includes the selection of the regularization parameter for the Ambrosio-Tortorelli functional, a simulation of the contact sets in the evolution of the micro-electro mechanical systems, and a numerical study of the flux selectivity in the Poisson-Nernst-Planck model. Sharp interfaces take place in all these three models, bringing interesting features and rich phenomena to study.

# Acknowledgements

I would like to express my sincere gratitude to my advisor, Professor Weizhang Huang, for his continuous support of my Ph.D study and related research, for his patience, motivation, and immense knowledge. His guidance helped me in all the time of research and writing of this thesis.

I would also like to thank the rest of my thesis committee: Professor Shawn Keshmiri, Professor Weishi Liu, Professor Xuemin Tu, and Professor Erik Van Vleck for their insightful comments and encouragement.

My sincere thanks to my collaborators: Professor Ronald Haynes, Professor Weishi Liu, Professor Alan Lindsay, Kelsey Dipietro, and my advisor Professor Weizhang Huang.

I thank all of my friends from KU Math department, for the tough, but also the most wonderful time in life that we have had together pursuing the Ph.D. degree in mathematics.

Last but not least, I would like to thank my family: my parents and my grandparents, for supporting me spiritually throughout writing this thesis and my life in general.

# Contents

# List of Figures

# Chapter 1

# Introduction

Solutions of many partial differential equations (PDEs) arising in physical sciences have large variations within a small portion of the domain. In this work, three models with this feature are described and studied: the Ambrosio-Tortorelli functional as a variational approach to image segmentation, a fourth-order parabolic equation that simulates the deformation of the micro-electro mechanical systems (MEMS), and a quasi-one-dimensional Poisson-Nernst-Planck (PNP) model as a dielectric continuum model of ionic fluxes. The sharp interfaces are a major property of all the three models, and all cause challenge in numerical computation.

A practical approach is to place a high density of mesh points in the regions of sharp interfaces, while much less density in the rest of the domain. In this work, I will present a PDE-based moving mesh strategy that is based on this idea. Rigorous mathematical formulation as well as practical implementation are described. This strategy has been applied to all the three models mentioned above using the linear finite element method. To complement the numerical approach, an asymptotic analysis has been developed regarding to specific aspects of each model.

The outline of this work is as follows. In Chapter 2, the mathematical characterization of an optimal adaptive mesh is derived, as well as the formulation of the corresponding energy functional. The minimization of the energy functional yields a PDE system, which defines the MMPDE method. MMPDE has been used to obtain the numerical results in Chapters 3, 4, and 5. With more nodes concentrated around the sharp layers, the abrupt changes in the solutions are better resolved.

In Chapter 3, a strategy for the selection of the regularization parameter in the Ambrosio-Tortorelli functional is derived and numerical results are presented. The Ambrosio-Tortorelli functional is a phase-field approximation of the Mumford-Shah functional that has been widely used

for image segmentation. It has the advantages of being easy to implement, maintaining the segmentation ability, and Gamma-converging to the Mumford-Shah functional as the regularization parameter goes to zero [1]. However, it has been observed in actual computation that the segmentation ability of the Ambrosio-Tortorelli functional varies significantly with different values of the parameter and even fails to Gamma-converge to the original functional for some cases. In this chapter we present an asymptotic analysis on the gradient flow equation of the Ambrosio-Tortorelli functional, from which a selection strategy for the regularization parameter is derived. An important objective of image segmentation is to locate the edges of the objects in the image, which are typically of small width, and thus high resolution of mesh elements is required. On the other hand, the mesh elements do not have to be that small within each object, as the function of the image is relatively smooth in this region. For this reason, the MMPDE method is highly desired for image segmentation.

In Chapter 4, an investigation of the contact sets in electrostatic-elastic deflections modeling micro-electro mechanical systems is described, approached by both numerical and analytical methods. The model for the membrane deflection is a fourth-order semi-linear PDE and the contact events occur in this system as finite time singularities. Primary research interest is in the dependence of the contact set on model parameters and the geometry of the domain. The adaptive numerical strategy is applied to increase density where the solution has fine scale detail, particularly in the vicinity of forming singularities. To complement the computational tool, a singular perturbation analysis is used to develop a geometric theory for predicting possible contact sets. The validity of these two approaches are demonstrated with a variety of test cases.

In Chapter 5, a numerical investigation of the selectivity of the different fluxes through ionic channels is described and corresponding numerical results are presented. Ionic channels are large proteins that are embedded on cell membranes, through which the ions flux and control biological behaviors. We study the effects of the permanent charge interacting with boundary conditions, on the selectivity of the flux species. The permanent charge is a biological structure typically embedded on a thin neck of an ionic channel. The MMPDE method is critical due to the sharp

2

Debye Layers at the interface between the permanent charge regions and uncharged regions of ion channels caused by the permanent charge. Non-trivial behavior emerges as one varies the permanent charge from small to large, in particular, bifurcations of flux ratios are revealed, showing the rich phenomena of permanent charge effects.

# Chapter 2

# An Adaptive Moving Mesh Method

## Abstract

For many differential equation models from the physical and biological backgrounds, sharp layers and lack of regularity of the solution are a crucial feature and can cause great challenges in numerical computation. In this chapter, we describe an adaptive mesh strategy to increase the accuracy of the solutions. This strategy is a moving mesh partial differential equation (MMPDE) which dynamically relocates the mesh points to increase the density in regions where the solution has fine scale details that require high spatial resolution. A notable strength of this method is the ability to resolve not regular solutions in general geometries including non-convex and non-simply connected geometries. The discussion in this chapter is all based on simplicial meshes.

## 2.1 Characterization of $\mathbb{M}$-Uniform Meshes

In this section, we describe the mathematical characterization of an adaptive mesh, based on an idea that an optimal adaptive mesh is essentially a uniform mesh under a specific metric tensor.

### 2.1.1 Uniform meshes in Euclidean Norm

We first recall the definition of a uniform mesh. Denote the mesh as $\mathscr{T}_h = \{K\}$, where each $K$ refers to a single element. Then $\mathscr{T}_h$ is a uniform mesh if and only if it satisfies these two conditions:

(i) All elements of $\mathscr{T}_h$ have the same size, i.e.,

$$|K| = \frac{|\Omega|}{N}, \qquad \forall K \in \mathscr{T}_h,$$

where $N$ is the mesh size, $|\Omega|$ is the volume of the domain, and *IKI* is the volume of the element $K$.

(ii) Each element of $\mathscr{T}_h$ has the same shape. More specifically, for $\forall K \in \mathscr{T}_h$, $K$ is similar to a reference element $\hat{K}$.

For more specific mathematical description of (ii), note that $K$ and $\hat{K} \in \mathbb{R}^d$ are similar if and only if

$$\|\mathbf{x}_i^K - \mathbf{x}_0^K\| = \theta_K^{\frac{1}{2}} \|\xi_i^K - \xi_0^K\|, \qquad i = 1, \cdots, d \tag{2.1}$$

where $\mathbf{x}_i^K$, $i = 0, 1, \cdots, d$ are the coordinates of the vertices of $K$, and $\xi_i^K$, $i = 0, 1, \cdots, d$ are the coordinates of the corresponding vertices of $\hat{K}$, $\theta_K$ is a constant determined by element $K$. Let $F_K : \hat{K} \to K$ be the linear affine mapping that satisfies $F_K(\xi_i^K) = \mathbf{x}_i^K$. Thus,

$$F_K'(\xi_i^K - \xi_0^K) = \mathbf{x}_i^K - \mathbf{x}_0^K, \qquad i = 1, \cdots, K \tag{2.2}$$

where $F_K'$ is the Jacobian matrix of $F_K$. We then have

$$\|\mathbf{x}_i^K - \mathbf{x}_0^K\|^2 = (\mathbf{x}_i^K - \mathbf{x}_0^K)^T (\mathbf{x}_i^K - \mathbf{x}_0^K) = (\xi_i^K - \xi_0^K)^T F_K'^T F_K'(\xi_i^K - \xi_0^K).$$

On the other hand, by (2.1) we have

$$\|\mathbf{x}_i^K - \mathbf{x}_0^K\|^2 = \theta_K \|\xi_i^K - \xi_0^K\|^2 = \theta_K (\xi_i^K - \xi_0^K)^T (\xi_i^K - \xi_0^K),$$

5

we then have

$$(\xi_i^K - \xi_0^K)^T F_K^{\prime T} F_K^\prime (\xi_i^K - \xi_0^K) = \theta_K (\xi_i^K - \xi_0^K)^T (\xi_i^K - \xi_0^K), \qquad i = 1, \cdots, d. \qquad (2.3)$$

Let

$$E_K = [\xi_1^K - \xi_0^K, \cdots, \xi_d^K - \xi_0^K],$$

as $\xi_i^K - \xi_0^K$, $i = 1, \cdots, d$, are linearly independent, $E_K$ is invertible. By (2.3) we have

$$E_K^T F_K^{\prime T} F_K^\prime E_K = \theta_K E_K^T E_K.$$

As $E_K$ is invertible, this is equivalent to

$$F_K^{\prime T} F_K^\prime = \theta_K I,$$

where $I$ is the $d$ dimensional identity matrix.

**Corollary 2.1.0.1.** *For any symmetric positive definite matrix $A_{d \times d}$,*

$$\frac{\mathrm{tr}(A)}{d} \geq \det(A)^{\frac{1}{d}}.$$

*The equality only holds if $A = \theta I$, where $\theta$ is a constant.*

Corollary 2.1.0.1 is simply a result of arithmetic mean and geometric mean inequality.

As $F_K^\prime$ is a full rank matrix, $F_K^\prime F_K$ is a symmetric positive definite matrix, and the condition (ii) of the uniform meshes can be rewritten as

(ii) For $\forall K \in \mathscr{T}_h$ and the reference element $\hat{K}$, the Jacobian Matrix of $F_K$ satisfies

$$\frac{1}{d} \mathrm{tr}(F_K^{\prime T} F_K^\prime) = \det(F_K^{\prime T} F_K^\prime)^{\frac{1}{d}}.$$

## 2.1.2   Uniform mesh under a general metric $\mathbb{M}$.

The MMPDE method employs a metric tensor $\mathbb{M} = \mathbb{M}(\mathbf{x})$ to specify the size, shape, and orientation of the mesh elements throughout the domain. Here we always assume that $\mathbb{M}$ is symmetric and uniformly positive definite on $\Omega$.

The main idea of the MMPDE method is viewing any adaptive mesh $\mathscr{T}_h$ as a uniform one under the metric tensor $\mathbb{M}$.

The distance between two points $\mathbf{x}$ and $\mathbf{x} + d\mathbf{x}$ under the metric tensor $\mathbb{M}$ is defined as

$$\|(\mathbf{x} + d\mathbf{x}) - \mathbf{x}\|_{\mathbb{M}} = \|d\mathbf{x}\|_{\mathbb{M}} = \sqrt{d\mathbf{x}^T \mathbb{M}(\mathbf{x}) d\mathbf{x}},$$

and the volume of $K$ under metric $\mathbb{M}$ is

$$|K|_{\mathbb{M}} = \int_K \sqrt{\det(\mathbb{M}(\mathbf{x}))} d\mathbf{x}.$$

We now derive the mathematical characterization corresponding to (i), (ii) in Section 2.1.1 in metric $\mathbb{M}$. In practice, we choose $\mathbb{M}$ as a piecewise function for simplicity:

$$\mathbb{M}_K := \frac{1}{|K|} \int_K \mathbb{M}(x) d\mathbf{x}.$$

It is easy to see that (i) becomes

$$|K| \det(\mathbb{M}_K)^{\frac{1}{2}} = \frac{\sigma_h}{N}, \qquad K \in \mathscr{T}_h$$

where

$$\sigma_h = \sum_K |K| \det(\mathbb{M}_K)^{\frac{1}{2}}.$$

Corresponding to the similarity condition for a uniform mesh as described in (ii), similar to (2.3),

we obtain

$$\|\mathbf{x}_i^K - \mathbf{x}_0^K\|_{\mathbb{M}}^2 = (\mathbf{x}_i^K - \mathbf{x}_0^K)^T \mathbb{M}_K (\mathbf{x}_i^K - \mathbf{x}_0^K) = (\xi_i^K - \xi_0^K)^T F_K'^T \mathbb{M}_K F_K' (\xi_i^K - \xi_0^K)$$

$$= \theta_K (\xi_i^K - \xi_0^K)^T (\xi_i^K - \xi_0^K), \qquad i = 1, \cdots, d.$$

As $\xi_i^K - \xi_0^K$, $i = 1, \cdots, d$ are linearly independent,

$$F_K'^T \mathbb{M}_K F_K' = \theta_K I.$$

According to Corollary 2.1.0.1, this is equivalent to $\dfrac{1}{d} \mathrm{tr}(F_K'^T \mathbb{M}_K F_K') = \det(F_K'^T \mathbb{M}_K F_K')^{\frac{1}{d}}$.

We now conclude the conditions for $\mathbb{M}$-uniform mesh:

**Theorem 2.1.1** (Huang and Russel [36]). *The mesh $\mathscr{T}_h$ is uniform in metric tensor $\mathbb{M}$ if and only if satisfies the following two conditions*

$$\text{Equidistribution:} \qquad |K| \det(\mathbb{M}_K)^{\frac{1}{2}} = \frac{\sigma_h}{N}, \qquad K \in \mathscr{T}_h \tag{2.4a}$$

$$\text{Alignment:} \qquad \frac{1}{d} \mathrm{tr}(F_K'^T \mathbb{M}_K F_K') = \det(F_K'^T \mathbb{M}_K F_K')^{\frac{1}{d}}, \qquad K \in \mathscr{T}_h, \tag{2.4b}$$

*where*

$$\sigma_h = \sum_K |K| \det(\mathbb{M}_K)^{\frac{1}{2}}. \tag{2.5}$$

In practice, a typical option of $\mathbb{M}$ is the piecewise constant function

$$\mathbb{M}_K = \det(I + \alpha_h^{-1} |H_K|)^{-\frac{1}{d+4}} (I + \alpha_h^{-1} |H_K|), \qquad K \in \mathscr{T}_h \tag{2.6}$$

where $H_K$ is an approximate Hessian of $u_h$ on element $K$ that is obtained using a least-squares Hessian recovery technique, and $u_h$ is the finite element linear interpolation of the solution $u$. More specifically, $|H_K| = Q \mathrm{diag}(|\lambda_1|, \ldots, |\lambda_d|) Q^T$, with the eigen-decomposition of $H_K$ being

8

$Q\mathrm{diag}(\lambda_1,\ldots,\lambda_d)\,Q^T$, and $\alpha_h$ is chosen such that

$$\sum_{K\in\mathscr{T}_h}|K|\sqrt{\det(\mathbb{M}_K)}=2|\Omega|.$$

The choice (2.6) of $\mathbb{M}$ is known to be optimal with respect to the $L^2$ norm of the linear interpolation error [33], with the expectation that the mesh points will be concentrated around the regions where the recovered Hessian of $u_h$ has a large determinant.

## 2.2 Meshing energy functions

In this section, we describe a variational approach to derive the $\mathbb{M}$-uniform mesh. In practice, it is rather challenging to solve for the nonlinear equations (2.4a) and (2.4b). Instead, we obtain the physical meshes by minimizing energy functionals corresponding to (2.4a) and (2.4b), which is rather easy to implement.

**Lemma 2.2.1** (Huang and Russel [36]). *For any $p > 1$, there holds*

$$\left(\sum_{K}\frac{|K|\det(\mathbb{M}_K)^{\frac{1}{2}}}{\sigma_h}\left(\frac{1}{|K|\det(\mathbb{M}_K)^{\frac{1}{2}}}\right)^p\right)^{\frac{1}{p}}\geq\sum_{K}\frac{|K|\det(\mathbb{M}_K)^{\frac{1}{2}}}{\sigma_h}\left(\frac{1}{|K|\det(\mathbb{M}_K)^{\frac{1}{2}}}\right),\qquad(2.7)$$

*where $\sigma_h$ is as defined in Equation (2.5), and the equality holds if and only if*

$$|K|\det(\mathbb{M}_K)^{\frac{1}{2}}\equiv constant,\qquad\forall K\in\mathscr{T}_h.\qquad(2.8)$$

*Proof.* Let $q > 0$ such that $\frac{1}{p}+\frac{1}{q}=1$. Let

$$f_K=\frac{|K|\det(\mathbb{M}_K)^{\frac{1}{2p}}}{\sigma_h}\frac{1}{|K|\det(\mathbb{M}_K)^{\frac{1}{2}}},\qquad g_K=\left(\frac{|K|\det(\mathbb{M}_K)^{\frac{1}{2}}}{\sigma_h}\right)^{\frac{1}{q}}.$$

Thus, the right-hand-side of (2.7) is $\sum\limits_K f_K g_K$, and the left-hand-side is $(\sum\limits_K (f_K)^p)^{\frac{1}{p}} (\sum\limits_K (g_K)^q)^{\frac{1}{q}}$, where

$$\left( \sum_K (g_K)^q \right)^{\frac{1}{q}} = \left( \sum_K \left( \frac{|K| \det(\mathbb{M}_K)^{\frac{1}{2}}}{\sigma_h} \right)^{\frac{1}{q}*q} \right)^{\frac{1}{q}} = \left( \frac{\sum\limits_K |K| \det(\mathbb{M}_K)^{\frac{1}{2}}}{\sigma_h} \right)^{\frac{1}{q}} = 1.$$

Thus, by Höder's inequality, (2.7) holds. The equality only holds when $f = [f_K]_{K \in \mathscr{T}_h}$ and $g = [g_K]_{K \in \mathscr{T}_h}$ are linearly dependent, i.e., when $\dfrac{f_K}{g_K} \equiv constant$, which is equivalent to

$$|K| \det(\mathbb{M}_K)^{\frac{1}{2}} \equiv constant, \qquad \forall K \in \mathscr{T}_h.$$

$\square$

By Lemma 2.2.1, minimizing the left-hand-side of (2.7) will result in a mesh $\mathscr{T}_h$ that satisfies (2.8), which is the equidistribution condition of $\mathbb{M}$-uniform mesh. With a slight modification of (2.7), we can define an equidistribution energy function as

$$\begin{aligned} I_{eq}(\mathscr{T}_h) &= d^{\frac{dp}{2}} \sum_K |K| \det(\mathbb{M}_K)^{\frac{1}{2}} \left( \frac{1}{|K| \det(\mathbb{M}_K)^{\frac{1}{2}}} \right)^p \\ &= d^{\frac{dp}{2}} \sum_K |K| \det(\mathbb{M}_K)^{\frac{1}{2}} (\det(F_K')^{-1} \det(\mathbb{M}_K)^{-\frac{1}{2}})^p, \end{aligned} \qquad (2.9)$$

where we have used $\det(F_K') \det(\hat{K}) = \det(K)$, and thus $\det(F_K') = |K|/|\hat{K}| = |K|$ (for simplicity, we set $|\hat{K}| = 1$). For purpose of computation, we have dropped $\sigma_h$ from (2.7), which is essentially a Riemann sum of the volume of the domain under the metric tensor $\mathbb{M}$, and only depends on the mesh weakly.

We now derive an energy function for the alignment condition (2.4b). By Corollary 2.1.0.1, we know that

$$\frac{1}{d} \operatorname{tr}((F_K'^T)^{-1} \mathbb{M}_K^{-1} (F_K')^{-1}) \geq \det((F_K'^T)^{-1} \mathbb{M}_K^{-1} (F_K')^{-1})^{\frac{1}{d}},$$

or

$$\frac{1}{d}\operatorname{tr}((F_K'^T)^{-1}\mathbb{M}_K^{-1}(F_K')^{-1}) \geq (\det(F_K')^{-1}\det(\mathbb{M}_K)^{-\frac{1}{2}})^{\frac{2}{d}}. \tag{2.10}$$

Therefore, by minimizing the left-hand-side of (2.10) for all $K \in \mathscr{T}_h$, we can obtain a mesh $\mathscr{T}_h$ that satisfies (2.4b). To obtain the same physical dimension as (2.9), we now define the alignment energy function by rewriting (2.10) as

$$I_{ali}(\mathscr{T}_h) = \sum_K |K|\det(\mathbb{M}_K)^{\frac{1}{2}}[\operatorname{tr}((F_K'^T)^{-1}\mathbb{M}_K^{-1}(F_K')^{-1})^{\frac{dp}{2}} - d^{\frac{dp}{2}}(\det(F_K')^{-1}\det(\mathbb{M}_K)^{-\frac{1}{2}})^p]. \tag{2.11}$$

Note that the second term of (2.11) is the same as (2.9). We now combine $I_{eq}(\mathscr{T}_h)$ and $I_{ali}(\mathscr{T}_h)$ with a weight $\theta \in (0,1)$, and obtain a combined energy function for equidistribution condition ([32]) and alignment condition as

$$I_h(\mathscr{T}_h) = \theta I_{ali}(\mathscr{T}_h) + (1-\theta)I_{eq}(\mathscr{T}_h),$$

which can be rewritten as

$$\begin{aligned} I_h(\mathscr{T}_h) = &\theta\sum_K |K|\det(\mathbb{M}_K)^{\frac{1}{2}}\operatorname{tr}((F_K'^T)^{-1}\mathbb{M}_K^{-1}(F_K')^{-1})^{\frac{dp}{2}} \\ &+ (1-2\theta)d^{\frac{dp}{2}}\sum_K |K|\det(\mathbb{M}_K)^{\frac{1}{2}}(\det(F_K')^{-1}\det(\mathbb{M}_K)^{-\frac{1}{2}})^p. \end{aligned} \tag{2.12}$$

It is easy to see that (2.12) is a Riemann sum of a continuous functional, which has been shown to be coercive and polyconvex and has a minimizer when $p > 1$ and $0 < \theta \leq \frac{1}{2}$. In practice, typical choices for $p$ and $\theta$ are $p = 3/2$ and $\theta = 1/3$.

## 2.3 MMPDEs: x-Formulation and $\xi$-Formulation

In this section we describe the moving mesh equation (MMPDE), which is derived by a gradient descent method to minimize the energy function (2.12). We use here a discrete approach of [34] for the MMPDE method.

11

Let $E_c = [\xi_1 - \xi_0, \cdots, \xi_d - \xi_0]$, where $\xi_0, .., \xi_d$ are vertices of the reference element $\hat{K}$. For simplicity, we neglect the supscript $\hat{K}$. Accordingly, Let $E_K = [\mathbf{x}_1^K - \mathbf{x}_0^K, \cdots, \mathbf{x}_d^K - \mathbf{x}_0^K]$, where $\mathbf{x}_0^K$, $\cdots, \mathbf{x}_d^K$ are the corresponding vertices of the element $K$. Thus $F_K' E_c = E_K$, i.e.,

$$F_K' = E_K E_c^{-1}. \tag{2.13}$$

Thus $F_K'$ is a function of $\mathbf{x}_i^K$, $i = 0, \cdots, d$.

By the definition of metric tensor, $\mathbb{M}_K$ is also a function of $\mathbf{x}_K$. Thus the mesh energy function (2.12) is a function of the mesh nodes, i.e., $I_h = I_h(\mathbf{x}_1, \cdots, \mathbf{x}_{N_v})$, where $N_v$ is the number of total mesh nodes of $\mathscr{T}_h$, and $\mathbf{x}_i$, $i = 1, \cdots, N_v$, are the coordinates of the mesh nodes.

To minimize $I_h$, one need to find solutions to the nonlinear equations

$$\frac{\partial I_h}{\partial \mathbf{x}_i} = 0, \qquad i = 1, \cdots, N_v \tag{2.14}$$

where $\partial I_h / \partial \mathbf{x}_i$ is the row vector

$$\frac{\partial I_h}{\partial \mathbf{x}_i} = [\frac{\partial I_h}{\partial x_i^{(1)}}, \cdots, \frac{\partial I_h}{\partial x_i^{(d)}}].$$

However, (2.14) is typically highly nonlinear and has non-smooth derivatives, thus the convergence of the Newton's method is not guaranteed.

A gradient descent method to minimize $I_h$ has been developed as

$$\frac{\partial \mathbf{x}_i}{\partial t} = -\frac{P_i}{\tau} \left( \frac{\partial I_h}{\partial \mathbf{x}_i} \right)^T, \qquad i = 1, \ldots, N_v, \tag{2.15}$$

where $P_i$ is a positive function chosen to keep (2.15) invariant under the scaling transformation of $\mathbb{M}$, and $\tau > 0$ is a positive parameter used to adjust the response time of mesh movement to the

changes in $\mathbb{M}$. One can see that

$$\frac{\partial I_h}{\partial t} = -\sum_{i=1}^{N_v} \frac{P_i}{\tau} \frac{\partial I_h}{\partial \mathbf{x}_i} \left(\frac{\partial I_h}{\partial \mathbf{x}_i}\right)^T = -\sum_{i=1}^{N_v} \frac{P_i}{\tau} \|\frac{\partial I_h}{\partial \mathbf{x}_i}\|_2^2 \le 0.$$

Equation (2.15) is called the MMPDE mesh equation for **x**-formulation.

It has been proven in [35] that the mesh governed by (2.15) stays non-singular if it is non-singular initially. This result holds for any convex or concave domain in any dimension and for the semi-discrete form (2.15) or a fully-discrete form of (2.15). (In the latter case, the time step is required to be sufficiently small but not diminishing.)

The drawback of this formulation is that $\mathbb{M}$, as a function of **x**, needs to be constantly updated during the integration, which can be costly especially in higher dimensions. In order to avoid this disadvantage, the $\xi$-formula of MMPDE method has been derived.

For the $\xi$-formula, we shall use three meshes, the physical mesh $\mathscr{T}_h = \{\mathbf{x}_1, \ldots, \mathbf{x}_{N_v}\}$, the computational mesh $\mathscr{T}_{c,h} = \{\xi_1, \ldots, \xi_{N_v}\}$, and the reference computational mesh $\hat{\mathscr{T}}_{c,h} = \{\hat{\xi}_1, \ldots, \hat{\xi}_{N_v}\}$, with all of them having the same number of elements and the same connectivity.

Typically, $\hat{\mathscr{T}}_{c,h}$ is chosen to be a mesh as uniform as possible (under the Euclidean Metric) and kept fixed throughout the computation. The computational mesh $\mathscr{T}_{c,h}$ has been included only for computational purpose. For the $\xi$-method, the mesh energy function (2.12) is still used, with $F_K$ being the affine mapping from $K_c \in \mathscr{T}_{c,h}$ to $K \in \mathscr{T}_h$, where $K_c$ is the mesh element in $\mathscr{T}_{c,h}$ that is corresponding to $K$.

In the $\xi$-formula, $I_h$ is a function of both $\mathscr{T}_h$ and $\mathscr{T}_{c,h}$:

$$I_h = I_h(\mathscr{T}_h, \mathscr{T}_{c,h}) \equiv I_h(\mathbf{x}_1, \cdots, \mathbf{x}_{N_v}, \xi_1, \cdots, \xi_{N_v}).$$

The $\xi$-formula performs the gradient descent method with respect to the computational mesh $\mathscr{T}_{c,h}$:

$$\frac{\partial \xi_i}{\partial t} = -\frac{P_i}{\tau} \left(\frac{\partial I_h}{\partial \xi_i}\right)^T, \qquad i = 1, \cdots, N_v. \tag{2.16}$$

13

This equation, with proper modifications for the boundary vertices (to keep them on the boundary), is integrated from the initial mesh $\hat{\mathcal{T}}_{c,h}$. The Matlab function ode15s, a Numerical Differentiation Formula based integrator, is used for this purpose in our computation. Since $\mathcal{T}_h^n$ is fixed during the integration, there is no need of constantly reassigning the metric tensor $\mathbb{M}$. The new computational mesh obtained in this way is denoted by $\mathcal{T}_{c,h}^{n+1}$. Notice that $\mathcal{T}_h^n$ and $\mathcal{T}_{c,h}^{n+1}$ form a correspondence, i.e., $\mathcal{T}_h^n = \Psi_h(\mathcal{T}_{c,h}^{n+1})$. Then, the new physical mesh at $t^{n+1}$ is defined as

$$\mathcal{T}_h^{n+1} = \Psi_h(\hat{\mathcal{T}}_c),$$

which can be approximated readily by linear interpolation.

## 2.4 Scalar-by-matrix differentiation

The partial derivatives $\partial I_h / \partial \mathbf{x}_i$ and $\partial I_h / \partial \xi_i$, $i = 1, \cdots, N_v$, in (2.15) and (2.16), can be found analytically using scalar-by-matrix differentiation.

We first rewrite the energy function (2.12) in the form:

$$I_h = \sum_K |K| G((F_K')^{-1}, \det(F_K')^{-1}, \mathbb{M}(\mathbf{x}_K), \mathbf{x}_K),$$

where $\mathbf{x}_K$ is short for $(\mathbf{x}_0^K, \cdots, \mathbf{x}_d^K)$, $K \in \mathcal{T}_h$. By (2.13), $F_K'$ is a function of both $\xi_K = (\xi_0^K, \cdots, \xi_d^K)$ and $\mathbf{x}_K$.

As the metric tensor $\mathbb{M}_k(\mathbf{x})$ is a function of $\mathbf{x}_K$, the partial derivative $\partial I_h / \partial \mathbf{x}_i$ involves the partial derivatives of $G$ with respect to all these four arguments. On the other hand, the formula of the derivative $\partial I_h / \partial \xi_i$ is relatively simpler, as partial derivatives with respect to the last two arguments are not involved.

For the purpose of deriving $\partial I_h / \partial \xi_i$, $i = 1, \cdots, N_v$, we introduce the scalar-by-matrix notation. For simplicity, we only describe the formulation of $\partial I_h / \partial \xi_i$. $\partial I_h / \partial \mathbf{x}_i$ can also be derived using the tools described in this section.

**Definition 2.4.1.** *The derivative of f with respect to a matrix $A_{m \times n}$ is defined as*

$$\frac{\partial f}{\partial A} = \begin{bmatrix} \frac{\partial f}{\partial A_{11}} & \cdots & \frac{\partial f}{\partial A_{m1}} \\ \vdots & \vdots & \vdots \\ \frac{\partial f}{\partial A_{1n}} & \cdots & \frac{\partial f}{\partial A_{mn}} \end{bmatrix}. \tag{2.17}$$

We now introduce some properties of scalar-by-matrix differentiation.

**Lemma 2.4.2.** *(1) (The Chain Rule) Let t be a scalar variable involved in the matrix $A_{m \times n}$, we then have*

$$\frac{\partial f}{\partial t} = \sum_{i,j} \frac{\partial f}{\partial A_{ij}} = \text{tr}(\frac{\partial f}{\partial A} \frac{\partial A}{\partial t}).$$

*(2) Assume A, B and C are squared matrix, then*

$$\text{tr}(A^T) = \text{tr}(A),$$

$$\text{tr}(AB) = \text{tr}(BA),$$

$$\text{tr}(ABC) = \text{tr}(CAB) = \text{tr}(BCA).$$

*(3) For any square matrix A which involves a scalar variable t, there hold*

$$\frac{\partial \, \text{tr}(A)}{\partial t} = \text{tr}(\frac{\partial A}{\partial t}),$$

$$\frac{\partial \det(A)}{\partial A} = \det(A)A^{-1},$$

$$\frac{\partial \det(A)}{\partial t} = \text{tr}(\det(A)A^{-1}\frac{\partial A}{\partial t}).$$

Recall that for $\xi$-method, $F_K$ is the affine mapping from $K_c \in \mathcal{T}_{c,h}$ to $K \in \mathcal{T}_h$. Let

$$E_K = [\mathbf{x}_1^K - \mathbf{x}_0^K, \cdots, \mathbf{x}_d^K - \mathbf{x}_0^K], \qquad \hat{E}_k = [\xi_1^K - \xi_0^K, \cdots, \xi_d^K - \xi_0^K],$$

where $\xi_0, \cdots, \xi_d$ are the vertices of $K_c$, and $\mathbf{x}_0, \cdots, \mathbf{x}_d$ are the corresponding vertices of $K$, then

the Jacobian matrix $F'_K = E_K^{-1}\hat{E}_K$.

We first show the following observation: for each $K \in \mathcal{T}_h$, there holds

$$\frac{\partial G}{\partial \hat{E}_K} = \frac{\partial G}{\partial \left[\xi_1^K - \xi_0^K, \cdots, \xi_d^K - \xi_0^K\right]} = \begin{bmatrix} \frac{\partial G}{\partial \xi_1^K} \\ \vdots \\ \frac{\partial G}{\partial \xi_d^K} \end{bmatrix}. \tag{2.18}$$

The last step follows from a simple scalar chain rule. Let $\xi_{i,j}^K$ be the $j$th component of $\xi_i^K$, then the $j$th component of $\frac{\partial G}{\partial \xi_i^K}$ is the scalar partial derivative

$$\left(\frac{\partial G}{\partial \xi_i^K}\right)_{[j]} = \frac{\partial G}{\partial \xi_{i,j}^K}.$$

As all elements of $\hat{E}_K$ is independent from $\xi_{i,j}^K$ except the element $\xi_{i,j}^K - \xi_{0,j}^K$,

$$\frac{\partial G}{\partial \xi_{i,j}^K} = \frac{\partial G}{\partial(\xi_{i,j}^K - \xi_{0,j}^K)}\frac{\partial(\xi_{i,j}^K - \xi_{0,j}^K)}{\partial \xi_{i,j}^K} = \frac{\partial G}{\partial(\xi_{i,j}^K - \xi_{0,j}^K)},$$

thus (2.18) holds. Moreover,

$$\frac{\partial G}{\partial \xi_0^K} = \sum_{i=1}^{d} \frac{\partial G}{\partial(\xi_i^K - \xi_0^K)}\frac{\partial(\xi_i^K - \xi_0^K)}{\xi_0^K} = -\sum_{i=1}^{d} \frac{\partial G}{\partial(\xi_i^K - \xi_0^K)} = -e^T\frac{\partial G}{\partial \hat{E}_K},$$

where

$$e = \begin{bmatrix} 1 \\ \vdots \\ 1 \end{bmatrix}.$$

We have derived the matrix formula for $\partial G/\partial \xi_i^K$ for each individual $K \in \mathscr{T}_h$, $i = 0, \cdots, d$:

$$
\begin{bmatrix}
\frac{\partial G}{\partial \xi_0^K} \\
\frac{\partial G}{\partial \xi_1^K} \\
\vdots \\
\frac{\partial G}{\partial \xi_d^K}
\end{bmatrix}
=
\begin{bmatrix}
-e^T \\
I_{d \times d}
\end{bmatrix}
\frac{\partial G}{\partial \hat{E}_K}.
\tag{2.19}
$$

It remains to find $\frac{\partial G}{\partial \hat{E}_K}$. Let $t$ be any element of $\hat{E}_K$, and $\mathbb{J} = (F_K')^{-1} = \hat{E}^K (E^K)^{-1}$, thus $G$ can be rewritten as

$$
G = \sqrt{\det(\mathbb{M}_K)}(\operatorname{tr}(\mathbb{J}\mathbb{M}_K^{-1}\mathbb{J}^T))^{\frac{dp}{2}} - d^{\frac{dp}{2}}\sqrt{\det(\mathbb{M}_K)}\left(\frac{\det(\mathbb{J})}{\sqrt{\det(\mathbb{M}_K)}}\right)^p.
$$

By the train rule in Lemma 2.4.2,

$$
\begin{aligned}
\frac{\partial G}{\partial t} &= \operatorname{tr}\left(\frac{\partial G}{\partial \mathbb{J}}\frac{\partial \mathbb{J}}{\partial t}\right) + \frac{\partial G}{\partial \det(J)}\frac{\partial \det(\mathbb{J})}{\partial t} \\
&= \operatorname{tr}\left(E_K^{-1}\frac{\partial G}{\partial \mathbb{J}}\frac{\partial \hat{E}_K}{\partial t}\right) + \det(E_K^{-1})\frac{\partial G}{\partial \det(\mathbb{J})}\frac{\partial \det(\hat{E}_K)}{\partial t} \\
&= \operatorname{tr}\left(E_K^{-1}\frac{\partial G}{\partial \mathbb{J}}\frac{\partial \hat{E}_K}{\partial t}\right) + \det(E_K^{-1})\frac{\partial G}{\partial \det(\mathbb{J})}\operatorname{tr}\left(\det(\hat{E}_K)\hat{E}_K^{-1}\frac{\partial \hat{E}_K}{\partial t}\right) \\
&= \operatorname{tr}\left(\left(E_K^{-1}\frac{\partial G}{\partial \mathbb{J}} + \det(E_K^{-1})\frac{\partial G}{\partial \det(\mathbb{J})}\det(\hat{E}_K)\hat{E}_K^{-1}\right)\frac{\partial \hat{E}_K}{\partial t}\right).
\end{aligned}
\tag{2.20}
$$

Note that as $t$ is any element of the matrix $\hat{E}_K$, the matrix $\frac{\partial \hat{E}_K}{\partial t}$ is a matrix with all elements 0 except the one corresponding to $t$ being 1. By consequently choosing different $t$, one can observe from the Lemma 2.4.2 that (2.20) indicates that

$$
\frac{\partial G}{\partial \hat{E}_K} = E_K^{-1}\frac{\partial G}{\partial \mathbb{J}} + \frac{\partial G}{\partial \det(\mathbb{J})}\frac{\det(\hat{E}_K)}{\det(E_K)}\hat{E}_K^{-1}.
\tag{2.21}
$$

In order to complete the formula (2.21), the partial derivatives $\partial G/\partial \mathbb{J}$ (a matrix-valued func-

tion) and $\partial G/\partial \det(\mathbb{J})$ can be found as

$$\frac{\partial G}{\partial \mathbb{J}} = dp\theta\sqrt{\det(\mathbb{M}_K)}(\mathrm{tr}(\mathbb{J}\mathbb{M}_K^{-1}\mathbb{J}^T))^{\frac{dp}{2}-1}\mathbb{M}_K^{-1}\mathbb{J}^T,$$

$$\frac{\partial G}{\partial \det(\mathbb{J})} = p(1-2\theta)d^{\frac{dp}{2}}\det(\mathbb{M}_K)^{-\frac{1-p}{2}}\det(\mathbb{J})^{p-1}.$$

We can see that if we choose $P = \det(\mathbb{M})^{\frac{p-1}{2}}$, the $\xi$-method (2.16) is invariant under scaling transformation of $\mathbb{M}$. For complete formula of the $\xi$-method, we can rewrite (2.16) as

$$\frac{\partial \xi_i}{\partial t} = \frac{P_i}{\tau} \sum_{K \in \omega_i} |K| v_{i_K}^K, \qquad i = 1, \ldots, N_v \tag{2.22}$$

where $\omega_i$ is the set of all the elements having $\mathbf{x}_i$ as a vertex and $v_{i_K}^K$ is the local velocity contributed by the element $K$ to vertex $\mathbf{x}_i$, with $i_K$ denoting the local index of $\mathbf{x}_i$ in $K$. The local velocities on element $K$ are given by rewriting (2.19):

$$\begin{bmatrix} (v_1^K)^T \\ \vdots \\ (v_d^K)^T \end{bmatrix} = -E_K^{-1}\frac{\partial G}{\partial \det(\mathbb{J})} - \frac{\partial G}{\partial \det(\mathbb{J})}\frac{\det(\hat{E}_K)}{\det(E_K)}\hat{E}_K^{-1}, \qquad v_0^K = -\sum_{i=1}^{d} v_d^K. \tag{2.23}$$

We note that the MMPDE equation (2.22) is already discrete in space (and thus no further spatial discretization is needed). Moreover, its computation mainly involves the calculation of the edge matrices and matrix inversion and multiplications.

## 2.5 Finite element discretization on a moving mesh

We now describe the finite element approximation on a moving mesh. Suppose we want to integrate the PDE fron time instant $0$ to $T$. Assume that we are given time instants

$$0 = t_0 < t_1 < \ldots < t_{n_f} = T,$$

the physical mesh $\mathscr{T}_h^n$, the numerical solution $u_h^n(\cdot, t)$, and the linear test functions $v_h^n(\cdot, t) \in V_h^0(t)$ defined thereon at $t_n$, where $V_h^0(t)$ is the span of the linear basis functions that are compactly supported on $\mathscr{T}_h(t)$ at $t$. The computation alternates between the integration of the PDE and the mesh equation. The new physical mesh $\mathscr{T}_h^{n+1}$ is first generated by an MMPDE-based strategy described in Section 2.3 and then the physical PDEs are integrated from $t_n$ to $t_{n+1}$. The procedure is repeated until $T$ is reached. The number of the mesh elements and the mesh connectivity are fixed throughout the computation.

To integrate the finite element approximation on a moving mesh, it is necessary to treat the mesh as functions of time $t$. Denote the coordinates of the vertices of $\mathscr{T}_h^n$ and $\mathscr{T}_h^{n+1}$ by $\mathbf{x}_j^n$ and $\mathbf{x}_j^{n+1}$, $j = 1, 2, \ldots, N_v$, respectively. We define the coordinates of the vertices between $t_n$ and $t_{n+1}$ as

$$\mathbf{x}_j(t) = \frac{t - t_n}{t_{n+1} - t_n} \mathbf{x}_j^{n+1} + \frac{t_{n+1} - t}{t_{n+1} - t_n} \mathbf{x}_j^n, \qquad j = 1, \ldots, N_v, \qquad t \in [t_n, t_{n+1}].$$

We use the fourth order parabolic PDE system (4.1) to be described in Section 4.1 as an example. Consider the fourth-order PDE:

$$
\begin{cases}
u_t = -\varepsilon^2 \Delta v - \dfrac{1}{(1+u)^2}, & (\mathbf{x}, t) \in \Omega \times (0, T) \\[2mm]
v = \Delta u, & (\mathbf{x}, t) \in \Omega \times (0, T) \\[2mm]
u = v = 0, & (\mathbf{x}, t) \in \partial\Omega \times (0, T) \\[2mm]
u(\mathbf{x}, 0) = v(\mathbf{x}, 0) = 0, & \mathbf{x} \in \Omega.
\end{cases}
\tag{2.24}
$$

The corresponding mesh at time $t$ is denoted by $\mathscr{T}_h(t)$. Then, a linear finite element approximation for (2.24) is to find $u_h(\cdot, t), v_h(\cdot, t) \in V_h^0(t)$, for $t \in (t_0, T]$, such that

$$
\begin{cases}
\displaystyle\int_\Omega \frac{\partial u_h}{\partial t} \psi \, d\mathbf{x} - \varepsilon^2 \int_\Omega \nabla v_h \cdot \nabla \psi \, d\mathbf{x} + \int_\Omega \frac{\psi}{(1+u_h)^2} d\mathbf{x} = 0, & \forall \psi \in V_h^0(t) \\[4mm]
\displaystyle\int_\Omega v_h \psi \, d\mathbf{x} + \int_\Omega \nabla u_h \cdot \nabla \psi \, d\mathbf{x} = 0, & \forall \psi \in V_h^0(t).
\end{cases}
\tag{2.25}
$$

19

Notice that linear basis functions and the linear finite element function space are time dependent. For simplicity, we assume that the first $N_{v_i}$ out of $N_v$ vertices are interior vertices. Denoting the linear basis function associated with the vertex $\mathbf{x}_j$ by $\psi_j(\cdot,t)$, $V_h^0(t)$ can be expressed as

$$V_h^0(t) = \text{span}\{\psi_1(\cdot,t), \ldots, \psi_{N_{v_i}}(\cdot,t)\}.$$

With the linear basis functions being time dependent, the main difference between the integration of (2.25) from that on a fixed mesh lies in the term $\frac{\partial u_h}{\partial t}$. To see this, expressing $u_h$ as

$$u_h(\mathbf{x},t) = \sum_{i=1}^{N_{v_i}} u_i(t)\psi_i(\mathbf{x},t), \qquad (2.26)$$

and differentiating it with respect to time, we get

$$\frac{\partial u_h(\mathbf{x},t)}{\partial t} = \sum_{i=1}^{N_{v_i}} \frac{du_i}{dt}\psi_i(\mathbf{x},t) + \sum_{i=1}^{N_{v_i}} u_i(t)\frac{\partial \psi_i(\mathbf{x},t)}{\partial t}.$$

It has been proven (e.g., see [36]) that

$$\frac{\partial \psi_i}{\partial t} = -\nabla \psi_i \cdot \dot{\mathbf{X}}, \qquad \text{a.e. in } \Omega$$

where the mesh velocity $\dot{\mathbf{X}}$ is defined as

$$\dot{\mathbf{X}} = \sum_{i=1}^{N_v} \dot{\mathbf{x}}_i \psi_i(\mathbf{x},t),$$

and the term $\dot{\mathbf{x}}_i$ denotes the nodal mesh speed. Combining the results above, we get

$$\frac{\partial u_h}{\partial t} = \sum_{i=1}^{N_{v_i}} \frac{du_i}{dt}\psi_i - \nabla u_h \cdot \dot{\mathbf{X}}.$$

Inserting these into (2.25) and taking $\psi = \psi_j$ successively, we can rewrite (2.25) into a system

of differential-algebraic equations in the form as

$$
\begin{cases}
M(\mathbf{X})\dot{\mathbf{U}} = \varepsilon^2 B(\mathbf{X})\mathbf{V} + F(\mathbf{X},\dot{\mathbf{X}},\mathbf{U}), \\[2ex]
\mathbf{0} = M(\mathbf{X})\mathbf{V} + B(\mathbf{X})\mathbf{U},
\end{cases}
\tag{2.27}
$$

where $\mathbf{X}$ is a vector representing the location of the vertices, $M(\mathbf{X})$ is the mass matrix, $B(\mathbf{X})$ is the stiffness matrix and $\mathbf{U}$, $\mathbf{V}$ are vectors of the unknown nodal values. This system for $\mathbf{U}$ and $\mathbf{V}$ is integrated from $t_n$ to $t_{n+1}$ using the fifth-order Radau IIA method (e.g., see Hairer and Wanner [29]), and the time step is chosen by a standard selection procedure [29] with a two-step error estimate of Gonzalez-Pinto et al. [28].

## 2.6   Conclusions

In this chapter, we have developed a precision numerical tool for exploring the sharp interfaces in physical models. Specifically, we have developed an adaptive moving mesh PDE method which dynamically relocates the mesh points to provide additional resolution in spatial regions with fine scale solution behavior. This method can automatically detect and resolve different types of dynamic features such as sharp interfaces and multiple forming singularities. The method can also accommodate the complex geometries and topological defects, as to be shown in Section 4.3.

It should be pointed out that a number of other moving mesh methods have been developed in the past and there is a vast literature in the area. The interested reader is referred to the books or review articles [2, 3, 11, 36, 75] and references therein.

# Chapter 3

# Selection of Regularization Parameter in the Ambrosio-Tortorelli Approximation of the Mumford-Shah Functional for Image Segmentation

## Abstract

Image segmentation is an important tool of simplifying, characterizing, and preprocessing images in the area of computer vision. It is a process of partitioning a given image into multiple components. It has been widely studied via different approaches, and in this chapter, I would like to describe and investigation of the variational approach. In the variational approach, an optimal image is the minimizer of an image energy functional. An important generalization of such functionals is the Mumford-Shah functional (1989). The Ambrosio-Tortorelli functional is a phase-field approximation of the Mumford-Shah functional that has been widely used for numerical computation. It has the advantages of being easy to implement, maintaining the segmentation ability, and $\Gamma$-converging [1] to the Mumford-Shah functional as the regularization parameter goes to zero.

However, it has been observed in actual computation that the segmentation ability of the Ambrosio-Tortorelli functional varies significantly with different values of the parameter and it even fails to $\Gamma$-converge to the original functional for some cases. In this chapter, an asymptotic analysis on the gradient flow equation of the Ambrosio-Tortorelli functional is presented. The asymptotic analysis shows that the functional can have different segmentation behavior for small but finite values of the regularization parameter, and explains why it loses

its segmentation ability as the parameter goes to zero. A selection strategy for the regularization parameter and a scaling procedure for the solution are devised based on the analysis. Numerical results show that they lead to good segmentation of the Ambrosio-Tortorelli functional for real images.

## 3.1    The Mumford-Shah Functional and the Amboriso-Tortorelli Functional

Segmentation for a given image is a process to find the edges of objects and partitions the image into separate parts that are relatively smooth. It has been achieved in mathematics by minimizing functionals and multiple theories have been developed. One of the most commonly used functionals, proposed by Mumford and Shah [61], takes the form

$$E[u,\Gamma] = \frac{\alpha}{2} \int_{\Omega \setminus \Gamma} |\nabla u|^2 d\mathbf{x} + \beta H^1(\Gamma) + \frac{\gamma}{2} \int_{\Omega} (u-g)^2 d\mathbf{x}, \tag{3.1}$$

where $\Omega$ is a rectangular domain, $\alpha$, $\beta$, and $\gamma$ are positive parameters, $g$ is the grey level of the input image, $u$ is the target image, $\Gamma$ denotes the edges of the objects in the image, and $H^1(\Gamma)$ is the one-dimensional Hausdorff measure. Upon minimization, $u$ is close to $g$, $\nabla u$ is small on $\Omega \setminus \Gamma$, and $\Gamma$ is as short as possible. An optimal image is thus close to the original one and almost piecewise constant. Moreover, the terms in (3.1) represent different and often conflicting objectives, making its minimization a challenging topic to study.

In order to avoid mathematical difficulties caused by the $H^1(\Gamma)$ term, De Giorgi et al. [17] propose an alternative functional as

$$F[u] = \frac{\alpha}{2} \int_{\Omega} |\nabla u|^2 d\mathbf{x} + \beta H^1(S_u) + \frac{\gamma}{2} \int_{\Omega} |u-g|^2 d\mathbf{x}, \tag{3.2}$$

where $S_u$ is the jump set of $u$. They show that (3.2) has minimizers in $SBV(\Omega)$ (the space of special functions of bounded variation) and is equivalent to (3.1) in the sense that if $u \in \Omega$ is a minimizer of (3.2), then $(u, S_u)$ is a minimizer of (3.1).

Although it is a perfectly fine functional to study in mathematics, (3.2) is not easy to implement in actual computation due to the fact that the jump set of the unknown function and its Hausdorff measure are extremely difficult, if not impossible, to compute. To avoid this difficulty, Ambrosio and Tortorelli [1] propose a regularized version as

$$AT_\varepsilon[u, \phi] = \frac{\alpha}{2} \int_\Omega (\phi^2 + k_\varepsilon)|\nabla u|^2 d\mathbf{x} + \beta \int_\Omega \left( \varepsilon|\nabla \phi|^2 + \frac{1}{4\varepsilon}(1-\phi)^2 \right) d\mathbf{x} + \frac{\gamma}{2} \int_\Omega |u - g|^2 d\mathbf{x}, \quad (3.3)$$

where $\varepsilon > 0$ is the regularization parameter, $k_\varepsilon = o(\varepsilon)$ is a parameter used to prevent the functional from becoming degenerate, and $\phi$ is a new unknown variable which ideally is an approximation of the complement of the characteristic function for the jump set of $u$, i.e.,

$$\phi(x) \approx \chi_u(x) \equiv \begin{cases} 0, & \text{if } \mathbf{x} \in S_u \\ 1, & \text{if } \mathbf{x} \notin S_u. \end{cases} \quad (3.4)$$

They show that $AT_\varepsilon$ has minimizers $u \in SBV(\Omega)$ and $\phi \in L^2(\Omega)$ and $\Gamma$-converges to $F(u)$. $\Gamma$-convergence, first introduced by Ennio de Giorgi, is a concept that guarantees the minimizer of a regularized functional converges to that of the original functional as the regularization parameter goes to 0.

The first finite element approximation for the functional $AT_\varepsilon$ is given by Bellettini and Coscia [6]. They seek linear finite element approximations $u_h$ and $\phi_h$ to minimize

$$AT_{\varepsilon,h}[u_h, \phi_h] = \frac{\alpha}{2} \int_\Omega (\phi_h^2 + k_\varepsilon)|\nabla u_h|^2 d\mathbf{x} + \beta \int_\Omega \left( \varepsilon|\nabla \phi_h|^2 + \frac{1}{4\varepsilon}\pi_h((1-\phi_h)^2) \right) d\mathbf{x}$$
$$+ \frac{\gamma}{2} \int_\Omega \pi_h((u_h - g_\varepsilon)^2) d\mathbf{x}, \quad (3.5)$$

where $\pi_h$ is the linear Lagrange interpolation operator and $g_\varepsilon$ is a smooth function which converges to $g$ in the $L^2$ norm as $\varepsilon \to 0$. They show that $AT_{\varepsilon,h}$ $\Gamma$-converges to $F(u)$ when the maximum element diameter is chosen as $h = o(\varepsilon)$. It should be pointed out that Feng and Prohl [23] have established the existence and uniqueness of the solution to an initial-boundary value problem (IBVP)

of the gradient flow equation of (3.3) and proven that a finite element approximation of the IBVP converges to the continuous solution as the mesh is refined.

It is noted that the Ambrosio-Tortorelli functional (3.3) is actually a phase-field approximation of the Mumford-Shah functional (3.1). Phase-field modeling has been used widely in science and engineering to handle sharp interfaces, boundaries, and cracks in numerical simulation of problems such as dendritic crystal growth [44, 80], multiple-fluid hydrodynamics [56, 73, 74, 83], and brittle fracture [9, 24, 60]. It employs a phase-field variable $\phi$, which depends on a regularization parameter $\varepsilon$ describing the actual width of the smeared interfaces, to indicate the location of the interfaces. Phase-field modeling has the advantage of being able to handle complex interfaces without relying on their explicit description. Mathematically, phase-field models such as (3.3) have been studied extensively (e.g., see [1]) for $\Gamma$-convergence. However, few studies have been published for the role of the regularization parameter in actual simulation. It is a common practice that a specific value of $\varepsilon$ is used without discussion or explanation in phase-field modeling. Even worse, it has been observed [59, 66, 79] that a phase-field model for brittle fracture simulation does not $\Gamma$-converge as $\varepsilon \to 0$ and $\varepsilon$ can be interpreted as a material parameter since its choice influences the "critical stress". More recently, $\varepsilon$ has been chosen as a material parameter based on theoretical and experimental analyses of a simplified phase-field model [63].

## 3.2 Behavior of the minimizer of $AT_\varepsilon$ as $\varepsilon \to 0$ for continuous $g$

As smaller $\varepsilon$ values do not increase the segmentation capability of (3.3) as expected, we would like to study the effects of the regularization parameter in (3.3). In this section, We consider the gradient flow equation of the functional $AT_\varepsilon$ subject to a homogeneous Neumann boundary condition and carry out an asymptotic analysis for the solution of the corresponding IBVP as $\varepsilon \to 0$. We present numerical results that complement the asymptotic analysis in Section 3.2.2.

### 3.2.1 An asymptotic analysis

We first explain why we consider $g$ as a continuous function. In image segmentation, the function $g$ represents an image and is given the grey-level values at the pixels. Generally speaking, the values of $g$ at points other than the pixels are needed in finite element computation. These values are computed commonly through (linear) interpolation of the values at the pixels. This means that $g$ is treated as a continuous function in finite element computation and such a treatment is independent of the regularization parameter. Thus we consider $g$ as a continuous function and want to study how the minimizer of $AT_\varepsilon$ behaves as $\varepsilon \to 0$.

To this end, we consider the gradient flow equation of functional (3.3),

$$
\begin{aligned}
u_t &= \alpha \nabla \cdot ((k_\varepsilon + \phi^2)\nabla u) - \gamma(u - g), \\
\phi_t &= 2\beta\varepsilon\Delta\phi - \alpha|\nabla u|^2\phi + \frac{\beta}{2\varepsilon}(1 - \phi),
\end{aligned}
\qquad t > 0,\ \mathbf{x} \in \Omega
\tag{3.6}
$$

subject to the homogeneous Neumann boundary condition

$$
\frac{\partial u}{\partial \mathbf{n}} = \frac{\partial \phi}{\partial \mathbf{n}} = 0 \qquad \text{for} \qquad \mathbf{x} \in \partial\Omega
\tag{3.7}
$$

and the initial condition

$$
u(\mathbf{x}, 0) = u^0(\mathbf{x}), \qquad \phi(\mathbf{x}, 0) = \phi^0(\mathbf{x}), \qquad \mathbf{x} \in \Omega.
\tag{3.8}
$$

This IBVP has been studied and used to find the minimizer of (3.3) (as a steady-state solution) by a number of researchers. For example, Feng and Prohl [23] have established the existence and uniqueness of the solution of the IBVP and proven that a finite element approximation converges to the continuous solution as the mesh is refined.

By assumption, $g \in C^0(\Omega)$. Then we can expect that the solution $u$ and $\phi$ of the IBVP is smooth. To see the behavior of the solution as $\varepsilon \to 0$, we consider the asymptotic expansion of $u$

and $\phi$ as

$$u = u^{(0)} + \varepsilon u^{(1)} + \varepsilon^2 u^{(2)} + \cdots, \tag{3.9}$$

$$\phi = \phi^{(0)} + \varepsilon \phi^{(1)} + \varepsilon^2 \phi^{(2)} + \cdots. \tag{3.10}$$

Inserting these into (3.6), we get

$$u_t^{(0)} + \varepsilon u_t^{(1)} + O(\varepsilon^2) = \alpha \nabla \cdot \left[ \left( o(\varepsilon) + (\phi^{(0)} + \varepsilon \phi^{(1)} + o(\varepsilon))^2 \right) \nabla (u^{(0)} + \varepsilon u^{(1)} + O(\varepsilon^2)) \right]$$
$$- \gamma (u^{(0)} + \varepsilon u^{(1)} + O(\varepsilon^2) - g), \tag{3.11}$$

$$\phi_t^{(0)} + \varepsilon \phi_t^{(1)} + O(\varepsilon^2) = 2\beta \varepsilon (\Delta \phi^{(0)} + \varepsilon \Delta \phi^{(1)} + O(\varepsilon^2))$$
$$- \alpha \left| \nabla u^{(0)} + \varepsilon \nabla u^{(1)} + O(\varepsilon^2) \right|^2 (\phi^{(0)} + \varepsilon \phi^{(1)} + O(\varepsilon^2))$$
$$+ \frac{\beta}{2\varepsilon} (1 - \phi^{(0)} - \varepsilon \phi^{(1)} - O(\varepsilon^2)), \tag{3.12}$$

where we have used $k_\varepsilon = o(\varepsilon)$. Collecting the $O(1)$ terms in (3.11), we have

$$u_t^{(0)} = \alpha \Delta u^{(0)} - \gamma (u^{(0)} - g), \qquad \text{in } \Omega. \tag{3.13}$$

Similarly, collecting the $O(1/\varepsilon)$ terms and $O(1)$ terms in (3.12) we get

$$\frac{\beta}{2} (1 - \phi^{(0)}) = 0, \qquad \phi_t^{(0)} = -\alpha |\nabla u^{(0)}|^2 \phi^{(0)} - \frac{\beta}{2} \phi^{(1)}.$$

From these we obtain

$$\phi = 1 - \varepsilon \frac{2\alpha}{\beta} |\nabla u^{(0)}|^2 + O(\varepsilon^2). \tag{3.14}$$

Like $u$, $u^{(0)}$ also satisfies the homogeneous Neumann boundary condition. Since $g \in C^0(\Omega)$, it can be shown (e.g., see [22]) that $u^{(0)}$ has continuous second-order derivatives and thus $\nabla u^{(0)}$ is bounded. Combining this with (3.14) we conclude that $\phi \to 1$ as $\varepsilon \to 0$. Since the boundaries

between different objects in $u$ are indicated by $\phi = 0$, this implies that $u$ is a single object and there is no segmentation as $\varepsilon \to 0$ when $g$ is continuous. Moreover, $u$ and thus $u^{(0)}$ are kept close to $g$ and we can expect $\nabla u^{(0)}$ to be large in the places where $\nabla g$ is large. From (3.14) we can see that, for small but not infinitesimal $\varepsilon$, $\phi$ can become zero at places where $\nabla g$ is large. In this case, the functional will have good segmentation.

We have seen so far that the choice of the regularization parameter in (3.3) can be crucial for image segmentation: *different values of $\varepsilon$ can lead to very different segmentation behavior of the functional and its segmentation ability will disappear as $\varepsilon \to 0$.*

It should be emphasized that the above observation is not in contradiction with the theoretical analysis made in [1] for the $\Gamma$-convergence and segmentation ability of the functional (3.3). In [1], these properties are analyzed for $u \in SBV(\Omega)$, implicitly implying that $u$ is discontinuous in general. The above analysis has been made under the assumption that $g$, and thus $u$ are continuous although they may have large gradient from place to place.

It is instructive to see some transient behavior of the solution to the gradient flow equation. To simplify, we drop the diffusion term in the second equation in (3.6) and get

$$\phi_t = -\alpha |\nabla u|^2 \phi + \frac{\beta}{2\varepsilon}(1 - \phi). \tag{3.15}$$

It has been proven in [23] that the solution of (3.6) satisfies $0 \leq \phi \leq 1$. From this we see that the first term on the right-hand side of (3.15) is nonpositive, which will make $\phi$ decrease, and the second term is nonnegative, making $\phi$ increase. These two terms will compete and reach an equilibrium state. Moreover, if $\phi = 1$, we have $\phi_t = -\alpha |\nabla u|^2 \leq 0$, meaning that as long as $|\nabla u| \neq 0$, the first term will decrease $\phi$ until $\phi_t = 0$ is reached. Similarly, if $\phi = 0$, we have $\phi_t = \frac{\beta}{2\varepsilon} > 0$, which means $\phi$ will increase until the system reaches its equilibrium. The equilibrium values of $\phi$ can be obtained by setting the right-hand side of (3.15) to be zero, i.e.,

$$\phi \approx \frac{\beta}{\beta + 2\varepsilon\alpha |\nabla u|^2}. \tag{3.16}$$

28

Thus, the equilibrium value of $\phi$ is around 1 for smooth regions where $\nabla u$ is small and around 0 on edges where $\nabla u$ is large.

### 3.2.2 Numerical results: behavior of $(u, \phi)$ as $\varepsilon \to 0$

In this section, we present numerical results which support the analysis in Section 3.2.1. The moving mesh finite element method described in Section 2 has been applied.

We choose two analytical functions for $g$, one of which is of one dimension, and another of two dimensions, to simulate the grey-level values of images. In particular, the sharp jumps in $g$ model the object edges in the image.

**Example 3.2.1** (1D hyperbolic tangent). *In this example, we take*

$$g = 0.5(1 + \tanh(100(x - 0.5))), \qquad x \in (0, 1) \tag{3.17}$$

*which has a sharp interface at $x = 0.5$. This is an oversimplified 1-d image example, with the sharp interface simulating the edge of an object in an image. An ideal segmentation should sharpen this jump while smoothing out the regions divided by the jump.*

We take $N = 200$, $\alpha = 0.01$, $\beta = 10^{-3}$, $\gamma = 10^{-3}$, and $k_\varepsilon = 10^{-9}$. The computed solution at three time instants for $\varepsilon = 0.1$, $0.01$, and $10^{-5}$ is shown in Fig. 3.1.

The first row of Fig. 3.1 shows the evolution of $u$ and $\phi$ for $\varepsilon = 0.1$. One can see that the jump is not sharpened and $u$ is smoothed out on the whole domain as time evolves. This indicates that the Ambrosio-Tortorelli functional with $\varepsilon = 0.1$ does not provide a good segmentation. The result is shown for a smaller $\varepsilon = 0.01$ on the second row of the figure. As time evolves, the jump is getting sharper and $u$ becomes piecewise constant essentially, an indication for good image segmentation. However, when $\varepsilon$ continues to decrease, as shown on the last row ($\varepsilon = 10^{-5}$) of Fig. 3.1, the jump disappears for the time being, $\phi$ approaches to 1, and $u$ becomes smooth over the whole domain. This implies that the Ambrosio-Tortorelli functional loses its segmentation ability for very small $\varepsilon$, consistent with the analysis in Section 3.2.

It is interesting to see the transient behavior of $\phi$. From the simplified equation (3.15), we have $\phi_t = -\alpha|\nabla u|^2\phi$ initially due to the initial condition $\phi = 1$. Thus, we expect that $\phi$ decreases initially and this decrease is more significant in the regions where $\nabla u$ is larger. This is confirmed in the numerical results; see Fig. 3.1(a,d,g). As time evolves, the system reaches an equilibrium state and $\phi$ is approximately given by (3.16). When $\varepsilon$ is not too small and $\nabla u$ is sufficiently large at some places, then $\phi$ can become close to zero at the places and this yields a good segmentation; see the second row of Fig. 3.1. However, when $\varepsilon$ is too small, $\phi$ will essentially become 1 everywhere and the functional loses its segmentation ability (cf. the third row of Fig. 3.1).



(a) $t = 0.005$, $\varepsilon = 0.1$     (b) $t = 1$, $\varepsilon = 0.1$     (c) $t = 20$, $\varepsilon = 0.1$

(d) $t = 0.005$, $\varepsilon = 0.01$     (e) $t = 1$, $\varepsilon = 0.01$     (f) $t = 20$, $\varepsilon = 0.01$

(g) $t = 0.005$, $\varepsilon = 10^{-5}$     (h) $t = 1$, $\varepsilon = 10^{-5}$     (i) $t = 20$, $\varepsilon = 10^{-5}$
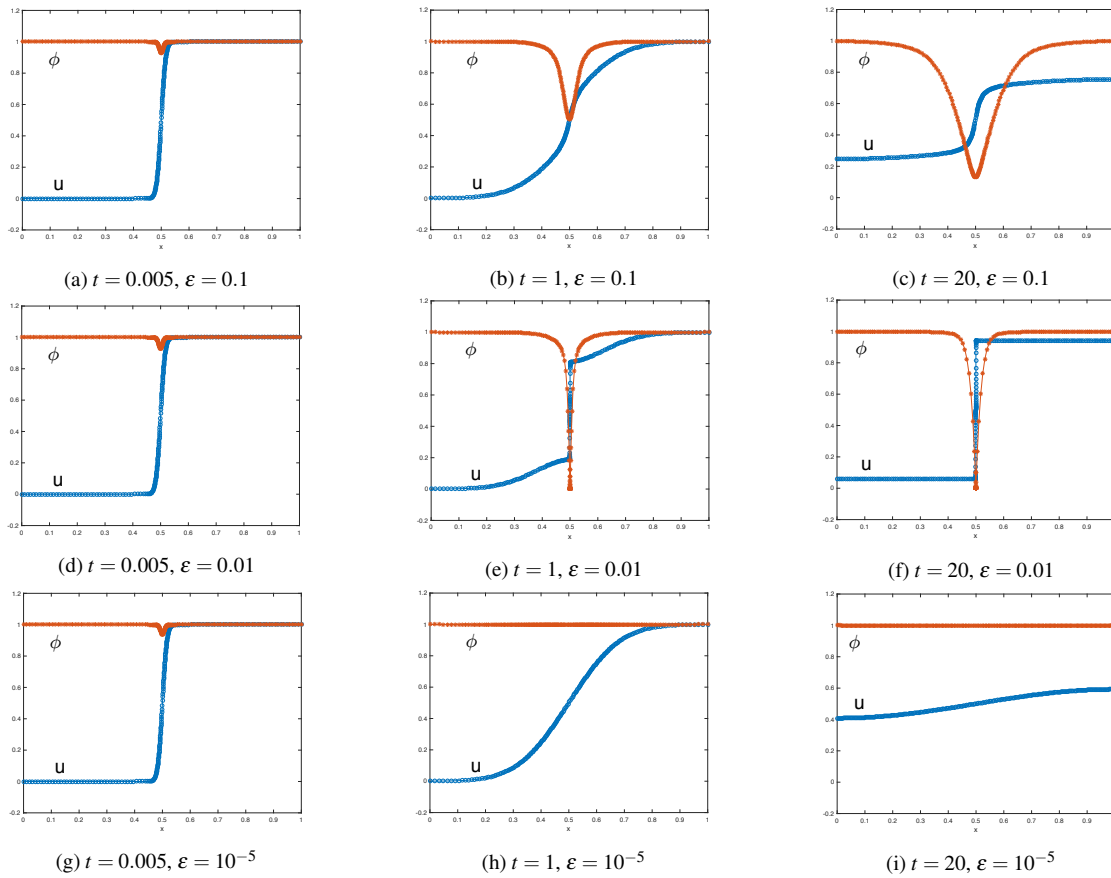
Figure 3.1: Example 3.2.1. The computed solution $u_h$ and $\phi_h$ at three time instants for various values of $\varepsilon$. No scaling has been used on $g$ and $u$.

**Example 3.2.2** (2D hyperbolic tangent). *In this example, we choose*

$$g = 0.49 \left[ 2 + \tanh(50(\sqrt{(x-0.5)^2 + (y-0.5)^2} - 0.05)) \right.$$
$$\left. - \tanh(50(\sqrt{(x-0.5)^2 + (y-0.5)^2} + 0.05)) \right], \qquad (x,y) \in (0,1) \times (0,1)$$

*which models a circle, being close to 0 on the circle and approximately* 1 *elsewhere. For the reasons to be explained in Section 3.3, u and g in the IBVP (3.6) are scaled in this example according to (3.19).*

We take $u^0 = g$, $\phi^0 = 1$, $N = 2 \times 50 \times 50$, $\alpha = 10^{-3}$, $\gamma = 10^{-5}$, $\beta = 10^{-2}$, and $k_\varepsilon = 10^{-10}$. The numerical results obtained with $\varepsilon = 10^{-3}$ and $\varepsilon = 10^{-7}$ are shown in Figs. 3.2 and 3.3, respectively.

Fig. 3.2 shows that the Ambrosio-Tortorelli functional with $\varepsilon = 10^{-3}$ makes a good segmentation. The evolution of $\phi$ is given on the first row, and $\phi$ deceases rapidly to 0 along the circle at $t = 7$. The image of the circle is clear as shown on the third row. However, the situation changes when a smaller $\varepsilon$ is used. As shown in Fig. 3.3 with $\varepsilon = 10^{-7}$, the segmentation ability disappears. As $t$ increases, $\phi$ becomes close to 1 in the whole domain, failing to identify the circle. In the same time, the image of $u$ blurs out. As for Example 3.2.1, the above observation is consistent with the analysis in Section 3.2, that is, when $g$ is continuous, the segmentation ability of the Ambrosio-Tortorelli functional varies for small but finite $\varepsilon$ and disappears as $\varepsilon \to 0$.

## 3.3 Selection of the regularization parameter and scaling of $u$ and $g$

### 3.3.1 Selection of the Regularization Parameter

From the analysis in Section 3.2 and the examples in the previous section, we have seen that it is crucial to choose a proper $\varepsilon$ for the Ambrosio-Tortorelli functional to produce a good segmentation when $g$ is continuous. To see how to choose $\varepsilon$ properly, we recall that $\phi$ is given in (3.14) for small

(a) t = 0.00015          (b) t = 2          (c) t = 7

(d) t = 0.00015          (e) t = 2          (f) t = 7

(g) t = 0.00015          (h) t = 2          (i) t = 7

Figure 3.2: Example 3.2.2. Evolution of the solution for $\varepsilon = 10^{-3}$. The first, second, and third rows show the evolution of $\phi$, the moving mesh, and the image of $u$, respectively.

$\varepsilon$. We want to have $\phi = 0$ on object edges. Taking $\phi = 0$ in (3.14) we get

$$\varepsilon = \frac{\beta}{2\alpha|\nabla u^{(0)}|^2},$$

where $u^{(0)}$ is the solution of (3.13) subject to a homogeneous Neumann boundary condition. Since $u^{(0)}$ is completely determined by its initial value $g$ and an objective of the Ambrosio-Tortorelli functional is to make $u$ (and thus $u^{(0)}$) close to $g$, it is reasonable to replace $u^{(0)}$ by $g$ in the above formula, i.e.,

$$\varepsilon = \frac{\beta}{2\alpha|\nabla g|^2}.$$

(a) t = 0.00015          (b) t = 2          (c) t = 7

(d) t = 0.00015          (e) t = 2          (f) t = 7

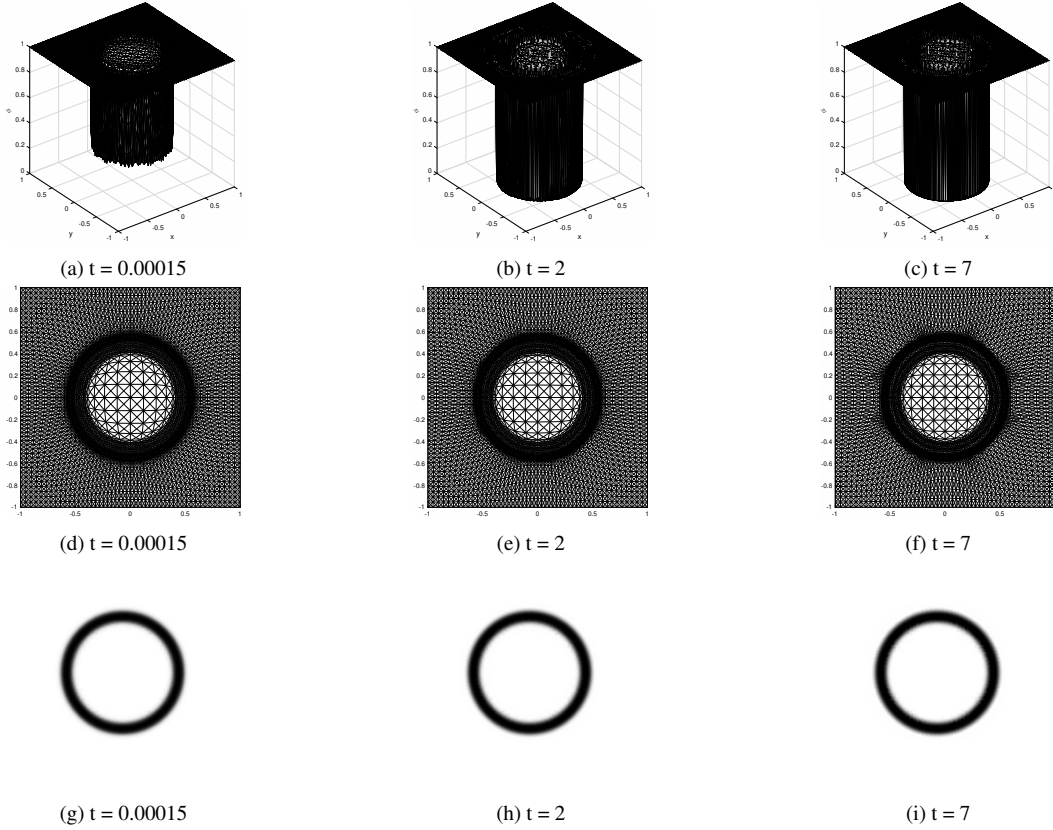(g) t = 0.00015          (h) t = 2          (i) t = 7
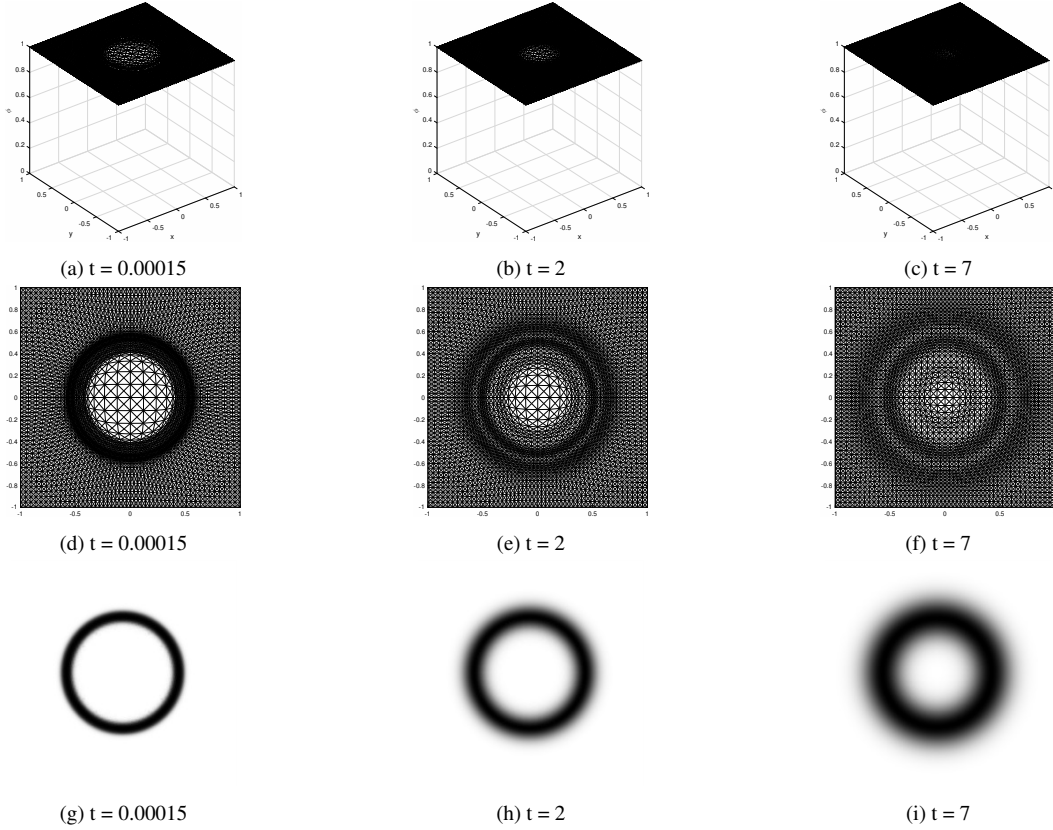
Figure 3.3: Example 3.2.2. Evolution of the solution for $\varepsilon = 10^{-7}$. The first, second, and third rows show the evolution of $\phi$, the moving mesh, and the image of $u$, respectively.

Since $|\nabla g|$ varies from place to place and $\varepsilon$ is a constant, in our computation we replace the former with $(|\nabla g|_{\max} + |\nabla g|_{\min})/2$ and have

$$\varepsilon = \frac{\beta}{2\alpha \left( (|\nabla g|_{\max} + |\nabla g|_{\min})/2 \right)^2}. \tag{3.18}$$

To demonstrate this choice of $\varepsilon$, we apply it to Example 3.2.1 and obtain $\varepsilon = 0.008$. The numerical result obtained with the same initial condition and parameters (other than $\varepsilon$) is shown in Fig. 3.4. One can see that this value of $\varepsilon$ leads to a good segmentation of the image.

### 3.3.2  Scaling of $g$ and $u$

Our experience shows that (3.18) works well when the difference in $\nabla g$ between the objects and their edges is sufficiently large. However, when the change of $\nabla g$ is small, the Ambrosio-Tortorelli

(a) t = 0.005             (b) t = 1             (c) t = 20
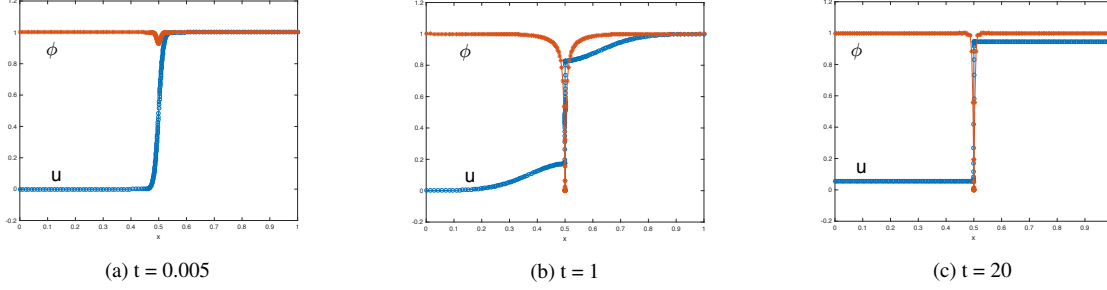
Figure 3.4: Example 3.2.1. The evolution of $u$ and $\phi$ for $\varepsilon = 0.008$ (determined by (3.18)). No scaling has been used on $u$ and $g$.

functional can still fail to produce a segmentation of good quality. To avoid this difficulty, we propose to scale $u$ and $g$ in (3.6), i.e., $u \rightarrow Lu$ and $g \rightarrow Lg$ for some parameter $L \geq 1$. This will make the change of $\nabla g$ from place to place more significant. Moreover, the first equation of (3.6) will stay invariant. The second equation becomes

$$\phi_t = 2\beta\varepsilon\Delta\phi - L^2\alpha|\nabla u|^2\phi + \frac{\beta}{2\varepsilon}(1 - \phi),$$

where the second term on the right-hand side is made larger, helping decrease $\phi$. We choose

$$L = \max\left\{1, \frac{|\nabla g|_{\mathrm{cr}}}{|\nabla g|_{\mathrm{max}}}\right\}, \tag{3.19}$$

where $|\nabla g|_{\mathrm{cr}}$ is a parameter. Generally speaking, the larger $|\nabla g|_{\mathrm{cr}}$ (and $L$) is, the more likely the segmentation works, but this will also make (3.6) harder to integrate. We take $|\nabla g|_{\mathrm{cr}} = 3 \times 10^3$ (by trial and error) in our computation, unless stated otherwise.

To demonstrate the effects of the scaling, we recompute Example 3.2.1 with $u^0 = g = 0.5(1 + \tanh(20(x - 0.5)))$, which has a less steep jump at $x = 0.5$ than the function (3.17). Results with and without scaling are shown in Fig. 3.5. It can be seen that scaling improves the segmentation ability of the Ambrosio-Tortorelli functional.

34

(a) $t = 0.005$       (b) $t = 1$       (c) $t = 20$

(d) $t = 0.005$       (e) $t = 1$       (f) $t = 20$
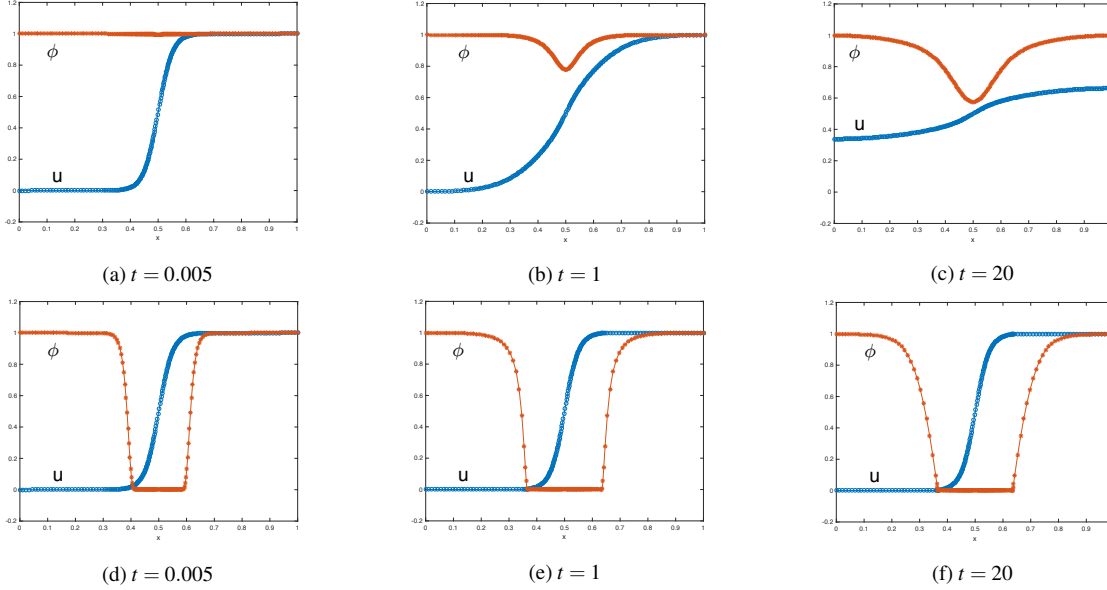
Figure 3.5: Example 3.2.1 with $g = 0.5(1 + \tanh(20(x - 0.5)))$ and $u^0 = g$. $\varepsilon$ is chosen as in (3.18) and other parameters are the same as in Example 3.2.1. No scaling is used for the top row while the scaling with (3.19) for $u$ and $g$ is used for the bottom row.

### 3.3.3 Segmentation for real images

To further demonstrate the effects of the selection strategy (3.18) and the scaling (3.19) we present results obtained for four real images. The results are shown in Figs. 3.6, 3.8, and 3.10 and the corresponding meshes are shown in Figs. 3.7, 3.9, and 3.11, respectively. In these four experiments, $N = 2 \times 70 \times 70$, $\alpha = 10^{-3}$, $\gamma = 10^{-5}$, $\beta = 10^{-2}$, and $k_\varepsilon = 10^{-10}$ are used. A random field in the range $(-0.25, 0.25)$ is added to $g$ as well as $u^0$. One can observe that the selection strategy (3.18) for the regularization parameter significantly improves segmentation for all cases.

## 3.4 Conclusions

The Mumford-Shah functional has been widely used for image segmentation. Its Ambrosio-Tortorelli Approximation has been known for its relative ease in implementation, segmentation ability, and $\Gamma$-convergence to the Mumford-Shah functional as the regularization parameter $\varepsilon$ goes to zero. The segmentation ability is based on the assumption that the input image $g$ is discontinuous across the boundaries between different objects, and this discontinuity must be maintained in

(a) $t = 0.005$, $\varepsilon = 10^{-5}$     (b) $t = 0.16$, $\varepsilon = 10^{-5}$     (c) $t = 0.6$, $\varepsilon = 10^{-5}$

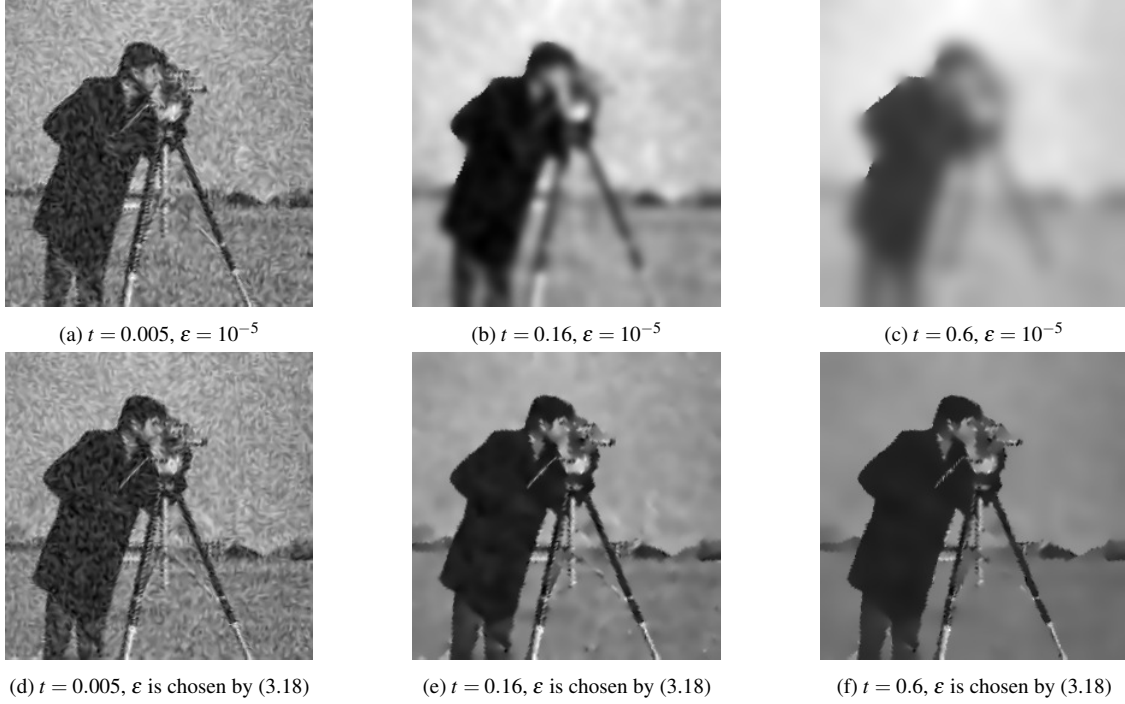(d) $t = 0.005$, $\varepsilon$ is chosen by (3.18)     (e) $t = 0.16$, $\varepsilon$ is chosen by (3.18)     (f) $t = 0.6$, $\varepsilon$ is chosen by (3.18)

Figure 3.6: A comparison of the image segmentation with different $\varepsilon$ values.

the limit of $\varepsilon \to 0$ during numerical computation to retain the $\Gamma$-convergence and the segmentation ability for infinitesimal $\varepsilon$ (e.g., see [6]). However, the maintenance of discontinuity in $g$ is often forgotten and $g$ is treated implicitly as a continuous function in actual computation. As a consequence, it has been observed that the segmentation ability of the Ambrosio-Tortorelli functional varies significantly with different values of $\varepsilon$ and the functional can even fail to $\Gamma$-converge to the original functional for some cases. Moreover, there exist very few published numerical studies on the behavior of the functional as $\varepsilon \to 0$.

We have presented in Section 3.2 an asymptotic analysis on the gradient flow equation of the Ambrosio-Tortorelli functional as $\varepsilon \to 0$ for continuous $g$. The analysis shows that the functional can have different segmentation behavior for small but finite $\varepsilon$ and eventually loses its segmentation ability for infinitesimal $\varepsilon$. This is consistent with the existing observations in the literature and the numerical examples in one and two spatial dimensions presented in Section 3.2.2 and Section 3.3.3. Based on the analysis, we have proposed a selection strategy for $\varepsilon$ and a scaling procedure for $u$ and $g$ in Section 3.3. Numerical results with real images show that they lead to a good segmentation of

(a) $t = 0.005$, $\varepsilon = 10^{-5}$      (b) $t = 0.6$, $\varepsilon = 10^{-5}$      (c) $t = 0.6$, $\varepsilon = 10^{-5}$

(d) $t = 0.005$, $\varepsilon$ is chosen by (3.18)      (e) $t = 0.16$, $\varepsilon$ is chosen by (3.18)      (f) $t = 0.6$, $\varepsilon$ is chosen by (3.18)
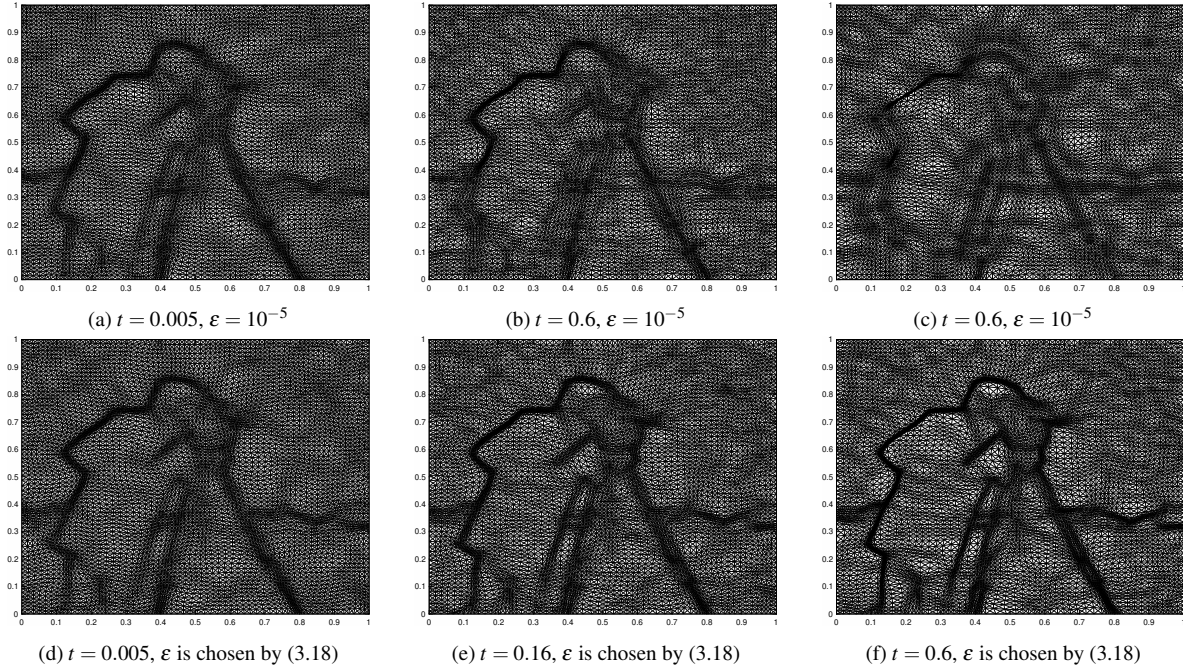
Figure 3.7: The meshes corresponding to Fig. 3.6.

the Ambrosio-Tortorelli functional.

Finally, we recall that the Ambrosio-Tortorelli functional is a special example of phase-field modeling for image segmentation. We hope that the analysis and the selection strategy for the regularization parameter presented in this work can also apply to other phase-field models. We are specially interested in the phase-field modeling of brittle fracture (e.g., see [9, 24, 60]).

(a) $t = 0.002$, $\varepsilon = 10^{-7}$   (b) $t = 0.008$, $\varepsilon = 10^{-7}$   (c) $t = 0.2$, $\varepsilon = 10^{-7}$

(d) $t = 0.002$, $\varepsilon$ is chosen by (3.18)   (e) $t = 0.008$, $\varepsilon$ is chosen by (3.18)   (f) $t = 0.2$, $\varepsilon$ is chosen by (3.18)
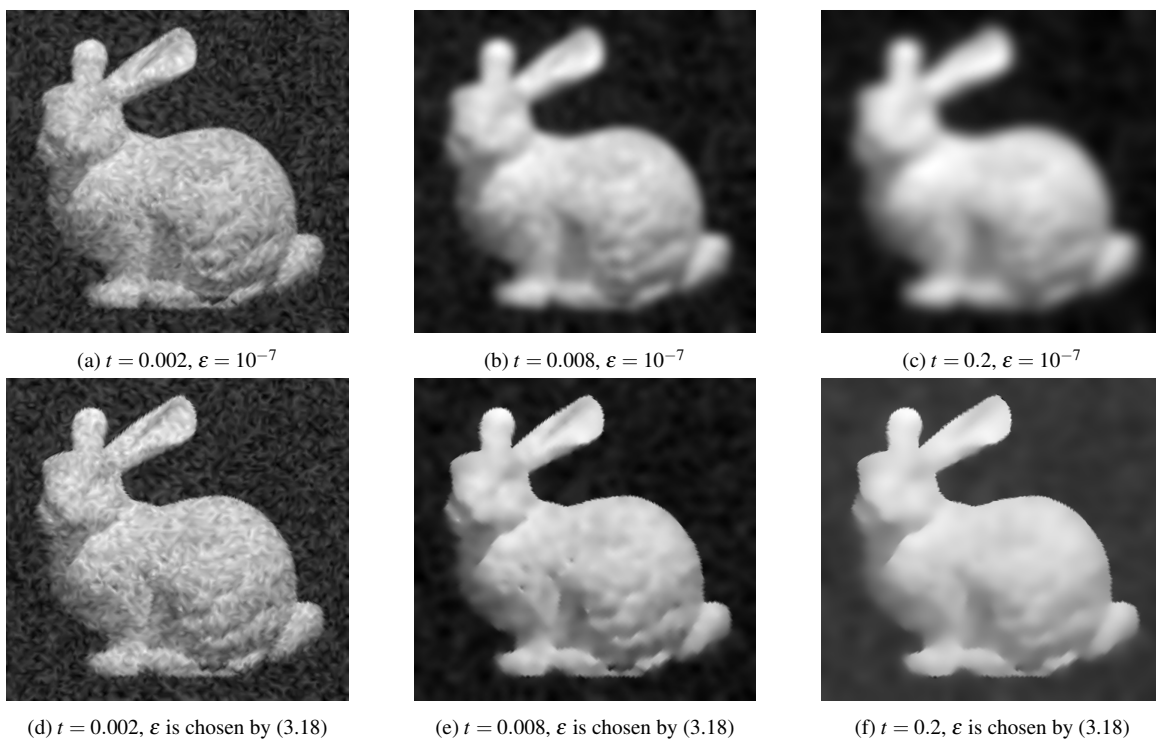
Figure 3.8: Evolution of the image.



(a) $t = 0.002$, $\varepsilon = 10^{-7}$   (b) $t = 0.008$, $\varepsilon = 10^{-7}$   (c) $t = 0.2$, $\varepsilon = 10^{-7}$

(d) $t = 0.002$, $\varepsilon$ is chosen by (3.18)   (e) $t = 0.008$, $\varepsilon$ is chosen by (3.18)   (f) $t = 0.2$, $\varepsilon$ is chosen by (3.18)
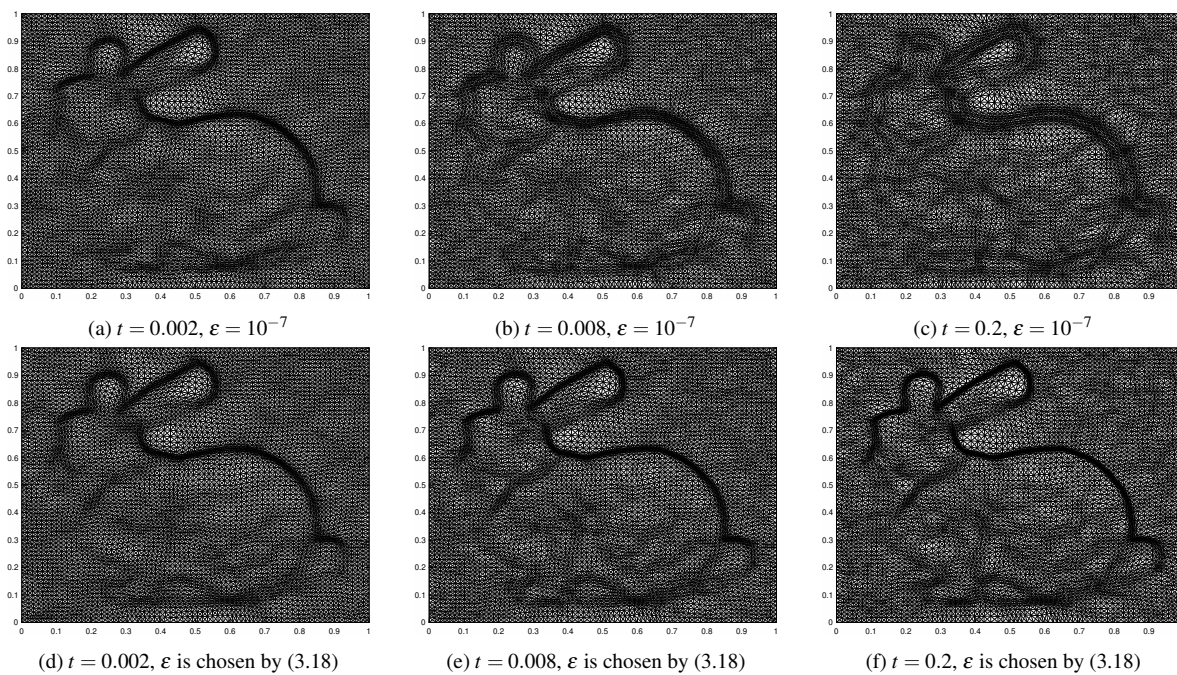
Figure 3.9: The meshes corresponding to Fig. 3.8.

(a) $t = 0.00013, \varepsilon = 10^{-7}$

(b) $t = 0.08, \varepsilon = 10^{-7}$

(c) $t = 0.3, \varepsilon = 10^{-7}$

(d) $t = 0.00013, \varepsilon$ is chosen by (3.18)

(e) $t = 0.08, \varepsilon$ is chosen by (3.18)

(f) $t = 0.3, \varepsilon$ is chosen by (3.18)

Figure 3.10: Evolution of the image.



(a) $t = 0.00013, \varepsilon = 10^{-7}$

(b) $t = 0.08, \varepsilon = 10^{-7}$

(c) $t = 0.3, \varepsilon = 10^{-7}$

(d) $t = 0.00013, \varepsilon$ is chosen by (3.18)

(e) $t = 0.08, \varepsilon$ is chosen by (3.18)

(f) $t = 0.3, \varepsilon$ is chosen by (3.18)

Figure 3.11: The meshes corresponding to Fig. 3.10.

# Chapter 4

# Contact Sets in Two Dimensional Models of Elastic-Electrostatic Deflection Models

## Abstract

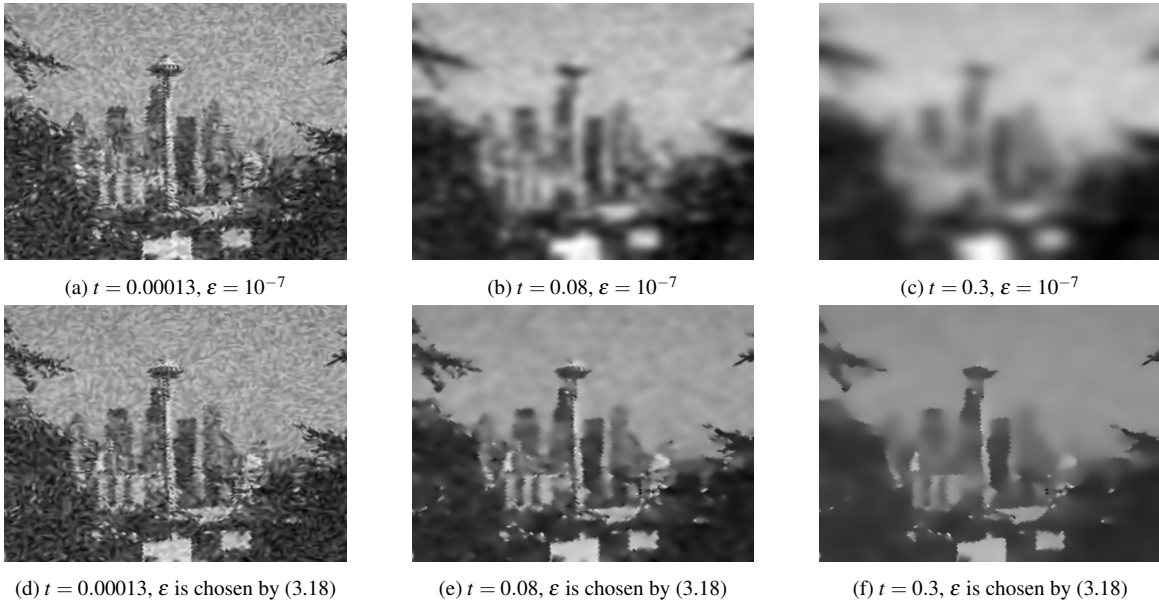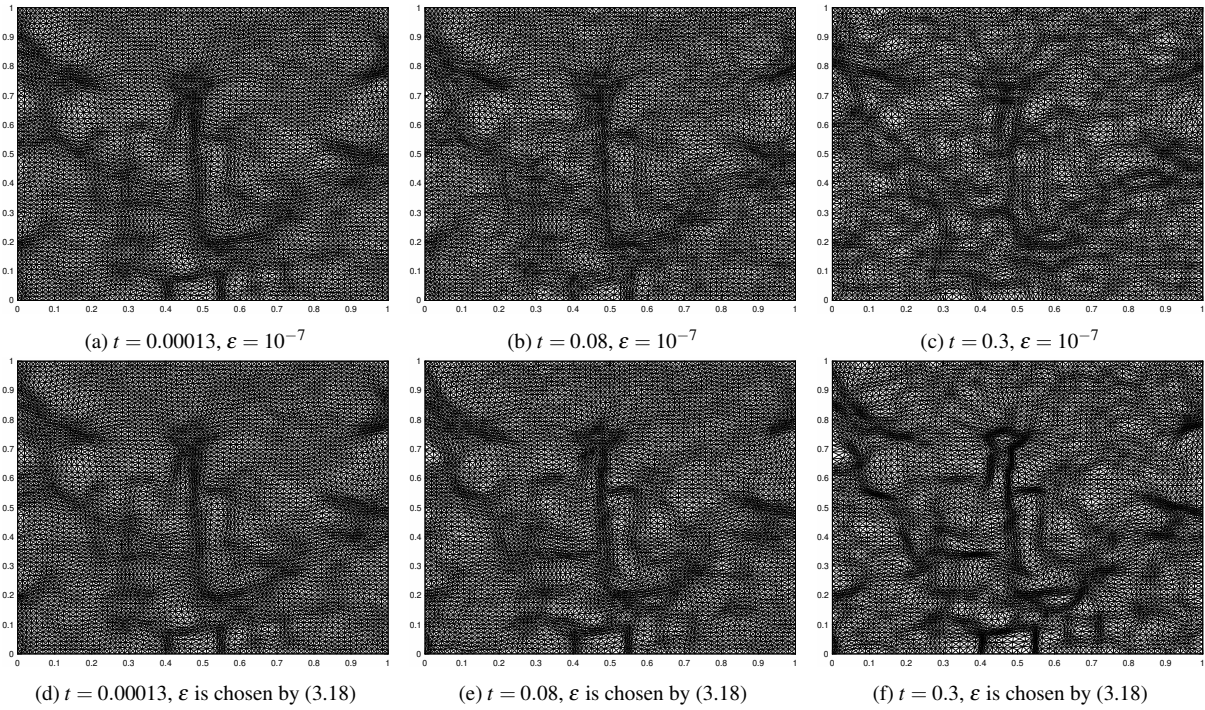The micro-electro mechanical systems capacitor is a key component of modern nanotechnology [76, 77, 5]. It features a deformable elastic membrane held fixed above a rigid substrate. The model for the membrane deflection is a fourth-order semi-linear partial differential equation and the contact events occur in this system as finite time singularities. Our primary research interest is in the dependence of the contact set on model parameters and the geometry of the domain. An increase in mesh density is necessary where the solution has fine scale detail, particularly in the vicinity of forming singularities. As such, the moving mesh partial differential equation (MMPDE) method has been applied for the numerical simulation. To complement this computational tool, a singular perturbation analysis is used to develop a geometric theory for predicting the possible contact sets. As will be shown later in this chapter, the validity of these two approaches are demonstrated with a variety of test cases.

## 4.1 Introduction

The fourth-order parabolic partial differential equation system 4.1 models the deflection of a micro-electro mechanical systems (MEMS) capacitor [52, 65, 64]:

$$
\begin{cases}
u_t = -\varepsilon^2 \Delta^2 u - \dfrac{1}{(1+u)^2}, & (\mathbf{x},t) \in \Omega \times (0,T); \\[2mm]
u = \Delta u = 0, & (\mathbf{x},t) \in \partial\Omega \times (0,T); \\[2mm]
u(\mathbf{x},0) = 0, & \mathbf{x} \in \Omega;
\end{cases}
\tag{4.1}
$$

where $\mathbf{x} = (x,y) \in \Omega$ can be a variety of bounded two dimensional geometries, and $z = u(\mathbf{x})$ is the non-dimensional vertical deflection. When an electric potential is applied between the deflecting plates, the top surface deforms towards the substrate (see Fig. 4.1a). In equation (4.1), the parameter $\varepsilon$ quantifies the relative importance of electrostatic and elastic forces in the system. If the restorative elastic forces are too weak, the attractive Coulomb forces between the two surfaces will bring them into physical contact. More specifically, if $\varepsilon$ is close to 0 in (4.1), the second term on the right is dominating, decreasing $u$ close to its limit $-1$ (but never reaches $-1$) in a finite time $T$, while $u_t(\mathbf{x},t)$ diverges as $t \to T$. This event, called *touchdown* or snap-through, can be useful or deleterious to operation, depending on the design of particular MEMS. The mechanism of the pull-in phenomenon has been studied extensively and many references can be found in the reviews [5, 85]. The design and operation of MEMS can be aided by placing physical limiters or con-
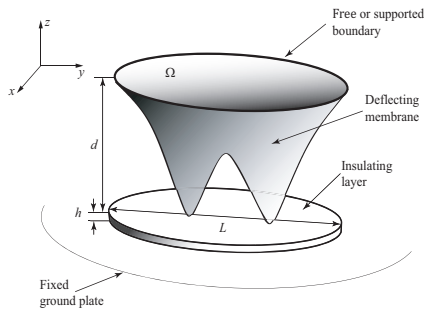


(a) Schematic diagram.
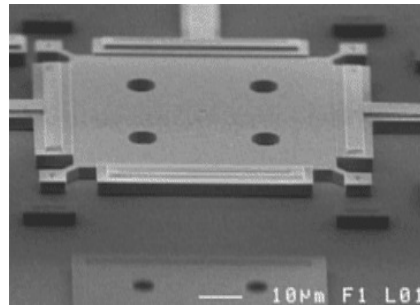
(b) A MEMS device (source: [71])

Figure 4.1: A MEMS device (right) and a schematic (left) around which models are formulated.

straints at locations where contact between the two membranes is more likely [45]. These limiters can prevent damage to the device that could occur when the two surfaces meet (see Fig. 4.1b). In addition, they allow for bistability in the system by creating stable large deflection configurations [52, 50, 69, 46, 47].

Therefore, it is important to know at which location(s) in $\Omega$ singularities can form. In the one-dimensional case with $\Omega = (-1,1)$, equation (4.1) can form one singularity at the origin or two singularities located symmetrically about the origin, depending on the particular value of $\varepsilon$ [51]. In the physically relevant two-dimensional scenario, the details of the geometry $\Omega$ and the dependence on the parameter $\varepsilon$ combine to make the set of possible singularity locations much more complex [53, 49].

Touchdown is a very rapid process in which energy is rapidly focussed in small spatial regions of $\Omega$. This process is manifested in the governing equations (4.1) by a finite time *quenching* singularity. The term quenching refers to the fact that $u(\mathbf{x},t)$ is finite at the point of singularity while $u_t(\mathbf{x},t)$ diverges as $t \to T$. Theoretical results on the quenching behavior of fourth-order parabolic equations such as (4.1) have established conditions under which quenching may occur [51, 48], studied the local form of the profile near singularity [53, 51, 10, 26] and given upper and lower estimates of the singularity time [25, 51, 67]. For reviews on the extensive literature on blow-up/quenching for parabolic PDEs, see [27] and references therein.

In previous computational studies of singularity formation in second-order PDEs, moving mesh methods based on parabolic Monge-Ampére (PMA) discretization have been successfully employed in one-dimensional [14] or rectangular two-dimensional domains [12, 15, 13]. The PMA moving mesh approach has recently [16] been extended to the fourth-order PDE problem (4.1) by constructing a high regularity mapping between the computational and physical domains. The study [16] was based on a finite difference discretization of the PMA equation that restricted computations to rectangular domains. As will be shown later, the MMPDE approach is a robust method that can resolve the singularities of (4.1) in general non-simply connected two-dimensional regions such as those utilized in real MEMS devices (cf. Fig. 4.1b).

## 4.2 A geometric theory for singularity set prediction

In this section, we outline a geometric theory for predicting the location of singularities based on a singular perturbation analysis of (4.1) as $\varepsilon \to 0$. We use asymptotic analysis in the limit as $\varepsilon \to 0$ to establish a prediction of the singularity set of (4.1). This theory explains the sensitivity of the contact set and the multiplicity of touchdown points on the parameter $\varepsilon$ and the geometry $\Omega$.

We find that singularities are more likely to form on a set $S_\Omega \subset \Omega$ known as the *skeleton*. The skeleton of $\Omega$ is defined roughly as the collection of points $\mathbf{x} \in \Omega$ at which inward facing normal vectors meet at points equidistant to $\partial\Omega$. This geometric construction is a unique minimal representation of the domain $\Omega$ and is widely used in computer vision to store two- or three-dimensional objects [58].

### 4.2.1 Asymptotic analysis.

In the leading order analysis of (4.1) as $\varepsilon \to 0$, it is assumed that the term $-\varepsilon^2 \Delta^2 u$ is negligible almost everywhere, except in the vicinity of $\partial\Omega$. This suggests that the solution is largely spatially uniform satisfying $u(\mathbf{x},t) \sim u_0(t)$, where $u_0(t)$ is the solution of the initial value problem

$$\frac{du_0}{dt} = -\frac{1}{(1+u_0)^2}, \qquad t \in (0, T_0), \qquad u_0(0) = 0. \tag{4.2a}$$

The solution of (4.2a) is

$$u_0(t) = -1 + (1 - 3t)^{\frac{1}{3}}, \qquad t \in \left(0, \frac{1}{3}\right). \tag{4.2b}$$

This gives a leading order approximation of the singularity time as $T_0 = \frac{1}{3}$. We remark upon the quenching phenomenon whereby $u_0$ is finite as $t \to T_0^-$ while $u_{0t}$ diverges. Clearly (4.2b) does not satisfy the boundary condition $u = 0$ on $\partial\Omega$ which must be enforced in a boundary layer. To analyze this layer for a general geometry, we introduce an orthogonal coordinate system $(\rho, s)$ where $\rho = \text{dist}(\mathbf{x}, \partial\Omega) > 0$, while $s$, for $\mathbf{x} \in \partial\Omega$, denotes the arc-length along $\partial\Omega$. In this coordinate

system, (4.1) becomes

$$u_t = -\varepsilon^2 \left[ \partial_{\rho\rho} - \frac{\kappa}{1-\kappa\rho} \partial_\rho + \frac{1}{1-\kappa\rho} \partial_s \left( \frac{1}{1-\kappa\rho} \partial_s \right) \right]^2 u - \frac{1}{(1+u)^2}, \qquad \rho > 0; \qquad (4.3a)$$

$$u = \left[ \partial_{\rho\rho} - \frac{\kappa}{1-\kappa\rho} \partial_\rho + \frac{1}{1-\kappa\rho} \partial_s \left( \frac{1}{1-\kappa\rho} \partial_s \right) \right] u = 0, \qquad \rho = 0, \qquad (4.3b)$$

where $\kappa = \kappa(s)$ is the curvature of $\partial\Omega$. To analyze the boundary layer in this new coordinate system, we introduce the stretched variables

$$u = f(t)\,w(z), \qquad z = \frac{\rho}{\phi(t;\varepsilon)}, \qquad \phi(t;\varepsilon) = \varepsilon^{\frac{1}{2}} f(t)^{\frac{1}{4}}, \qquad f(t) = -u_0(t) = 1 - (1-3t)^{\frac{1}{3}}. \quad (4.4)$$

The variables (4.4) are substituted into (4.3) and the resulting system is expanded in the form

$$w(z) = w_0(z) + \phi\,w_1(z) + \cdots. \qquad (4.5)$$

Collecting terms at each order gives a sequence of problems for $\{w_0, w_1, \ldots\}$. At leading order we have

$$w_{0zzzz} - \frac{z}{4} w_{0z} + w_0 = -1, \qquad z > 0; \qquad (4.6a)$$

$$w_0 = w_{0zz} = 0, \qquad z = 0; \qquad w_0 \sim -1, \qquad z \to \infty. \qquad (4.6b)$$

While the solution of (4.6) can be developed in terms of hypergeometric functions, the resulting expression is quite cumbersome and not particularly useful. The most important property is the behavior of $w_0(z)$ as $z \to \infty$ which can be derived from a WKB analysis [49]. In particular,

$$w_0(z) \sim -1 + A e^{-\omega z^{\frac{4}{3}}} \sin[\sqrt{3}\,\omega z^{\frac{4}{3}} + \psi] + \cdots, \qquad z \to \infty, \qquad (4.6c)$$

where $\omega = 3 \cdot 2^{-\frac{11}{3}}$ and $A, \psi$ are constants. The crucial observation from the limiting behavior (4.6c) is the oscillatory decay for $z$ large. This phenomenon is a manifestation of the lack of a

44

maximum principle for fourth-order equations. In particular, $w_0(z)$ attains its global minimum at a finite value, which can be approximated numerically as $z_0 \approx 2.89$ - see Fig. 4.2.

At the next order, we apply the decomposition $w_1(z,s) = \kappa(s)\bar{w}_1(z)$ and find that $\bar{w}_1(z)$ satisfies

$$\bar{w}_{1zzzz} - \frac{z}{4}\bar{w}_{1z} + \frac{5}{4}\bar{w}_1 = 2w_{0zzz}, \qquad z > 0; \tag{4.7a}$$

$$\bar{w}_1 = \bar{w}_{1zz} - w_{0z} = 0, \qquad z = 0; \qquad \bar{w}_1 \sim 0, \qquad z \to \infty. \tag{4.7b}$$

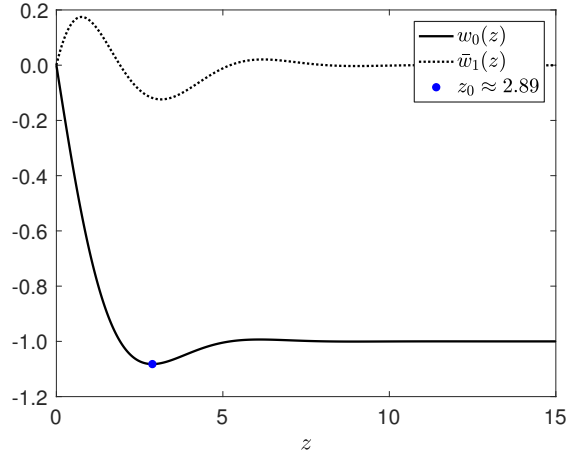The two profiles $w_0(z)$ and $\bar{w}_1(z)$ are shown in Fig. 4.2.



Figure 4.2: The two profiles $w_0(z)$ and $\bar{w}_1(z)$ satisfying (4.6) and (4.7).

The lack of monotonicity in the profiles of the stretching boundary layer lowers the value of the solution at certain points. By superimposing the boundary layer solution with the flat solution $u_0(t)$, and subtracting the overlap term, the following global solution at a particular $\mathbf{x} \in \Omega$ is

$$u(\mathbf{x},t) = u_0(t) - u_0(t) \sum_{j=1}^{N} \left( 1 + w_0 \left( \frac{|\mathbf{x} - \mathbf{y}_j|}{\phi} \right) + \phi \, \kappa(\mathbf{y}_j)\bar{w}_1 \left( \frac{|\mathbf{x} - \mathbf{y}_j|}{\phi} \right) + \cdots \right), \tag{4.8}$$

where $\phi = \varepsilon^{\frac{1}{2}}|u_0(t)|^{\frac{1}{4}}$. For each $\mathbf{x} \in \Omega$, the boundary points $\{\mathbf{y}_1, \dots, \mathbf{y}_N\} \in \partial\Omega$ are those with inward facing normal vectors that pass through $\mathbf{x}$, i.e., points such that the straight line between $\mathbf{x}$ and $\mathbf{y}_j$ is contained in $\Omega$ and meets $\partial\Omega$ orthogonally. The quantity $\kappa(\mathbf{y}_j)$ is the local boundary

curvature at the point $\mathbf{y}_j$. The asymptotic expansion (4.8) is valid for $\phi \ll 1$ which corresponds to short times $t \ll 1$. In this regime, the solution is composed of a flat central region coupled to propagating boundary interfaces.

## 4.2.2 The skeleton of the domain.

We now use the asymptotic solution (4.8) to develop a predictive theory for how the geometry $\Omega$ and $\varepsilon$ combine to select possible singularity locations. As shown in Fig. 4.2, the profile $w_0(z)$ has a unique global minimum at $z = z_0$ whose value can be estimated numerically as $z_0 \approx 2.89$. In light of this, and the arguments of the solution (4.8), the set of points

$$\omega(t) = \{\mathbf{x} \in \Omega \mid \text{dist}(\mathbf{x}, \partial\Omega) = z_0 \phi(t; \varepsilon)\} \tag{4.9}$$

are particularly important. The condition (4.9) describes a curve of points (cf. Fig. 4.3a) that extend inwards from $\partial\Omega$ a distance $z_0 \phi(t; \varepsilon)$ and along which the solution of (4.1) is, to first order in $\phi$, at a local minimum. In computer vision literature [58], this set is known as the *firefront*. In a radially
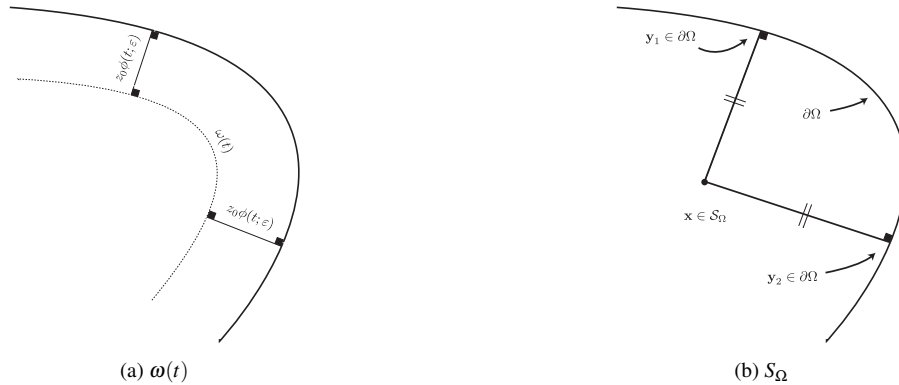


(a) $\omega(t)$           (b) $S_\Omega$

Figure 4.3: The two sets $\omega(t)$ and $S_\Omega$ on which touchdown may occur.

symmetric scenario for which the boundary is of uniform curvature, the singularities may form simultaneously along a ring of points [81, 49]. For domains whose boundaries have non-uniform curvature, the effect is to promote touchdown at certain points rather than along entire curves. This can be deduced from the asymptotic solution (4.8) by seeking a regular expansion solution

$z_{\min} = z_0 + \phi z_1 + \cdots$ of the equation $\nabla u = 0$. This reveals that

$$z_{\min} = z_0 - \alpha\phi\frac{1}{N}\sum_{j=1}^{N}\kappa(\mathbf{y}_j) + \mathcal{O}(\phi^2), \qquad \alpha = -\frac{\bar{w}_{1z}(z_0)}{w_{0zz}(z_0)} \approx 0.3533. \qquad (4.10\text{a})$$

The corresponding asymptotic prediction of the minimum is found from (4.8) to be

$$u(\mathbf{x},t)\mid_{z=z_{\min}} = u_0(t) - u_0(t)\sum_{j=1}^{N}\left(1 + w_0(z_0) + \phi\,\kappa(\mathbf{y}_j)\bar{w}_1(z_0) + \cdots\right), \qquad (4.10\text{b})$$

where numerically we determine the values

$$w_0(z_0) = -1.0822, \qquad \bar{w}_1(z_0) = -0.1186. \qquad (4.10\text{c})$$

Since $\bar{w}_1(z_0) < 0$, we conclude that the solution will take lower values at points of $\omega(t)$ whose contributing boundary points correspond to maxima of the boundary curvature $\kappa(s)$.

As $t$ increases and the curve $\omega(t)$ propagates, it may self-intersect at some time $t = t_S$. If this occurs, the solution minimum (4.10b) goes through a distinct change since the number of contributing boundary points, $N$, increases. For example, in the scenario displayed in Fig. 4.3, the set $\omega(t)$ eventually intersects the point $\mathbf{x} \in \Omega$ which receives boundary contributions from the two points $\{\mathbf{y}_1, \mathbf{y}_2\}$ and the number of boundary contributions increases from $N = 1$ to $N = 2$. These points are important as multiple boundary contributions arrive simultaneously and superimpose to lower the value of (4.10b) further - this set of points is called the *skeleton* of the domain and denoted $S_\Omega$. The time $t_S$ is then known as *the skeleton arrival time* and can be defined explicitly as

$$t_S = \inf_{t \geq 0}\left\{t \mid \exists \mathbf{x} \in S_\Omega,\ \text{dist}(\mathbf{x}, \partial\Omega) = z_0\phi(t;\varepsilon)\right\}. \qquad (4.11)$$

As indicted in Fig. 4.3b, a point $\mathbf{x} \in S_\Omega$ if it has at least two closest boundary points, i.e., $\text{dist}(\mathbf{x}, \partial\Omega) = \text{dist}(\mathbf{x}, \mathbf{y}_j)$ for $\{\mathbf{y}_1, \ldots, \mathbf{y}_N\} \in \partial\Omega$ and $N \geq 2$. The skeleton $S_\Omega \subset \Omega$ is a minimal representation of the domain $\Omega$. They are homotopic to one another so that each $\Omega$ defines a

unique $S_\Omega$ and vice-versa [58]. A particular point $\mathbf{x} \in S_\Omega$ can potentially be associated with multiple boundary distances in which case the most pertinent one is the shortest as that is where the trough associated with $w_0(z)$ will reach first.

In summary the asymptotic analysis makes the following prediction for the touchdown set. Let $S_\Omega$ be the skeleton of the domain, $t_S \geq 0$ be the skeleton arrival time and define $T$ to be maximum global existence time of (4.1). Then, the leading order asymptotic analysis predicts the following the dichotomy of possibilities:

1. If $T < t_S$, the singularities form on $\omega(t)$ at point(s) corresponding to maximum boundary curvature.

2. If $T \geq t_S$, the singularities form on $S_\Omega$ at points $\mathbf{x} \in S_\Omega$ satisfying $\text{dist}(\mathbf{x}, \partial\Omega) = \phi(T; \varepsilon)$.

## 4.3  Numerical results

In this section, we demonstrate the efficacy of adaptive numerical methodology and the asymptotic predictions on a variety of examples. For each of the domains $\Omega$ considered, we first calculate the skeleton $S_\Omega$ of the region defined in Sec. 4.2.2. The numerical integration of the PDE system (4.1) is performed until $\min_{\mathbf{x} \in \Omega} u_h = -0.99$.

**Example 4.3.1** (Rectangular domain). We first consider the rectangular domain $\Omega = (-1, 1) \times (-0.8, 0.8)$.

In Fig. 4.4 we show $\Omega$ and the skeleton $S_\Omega$ together with numerically obtained touchdown points for the parameter range $\varepsilon \in (10^{-4}, 10^{-1})$. In Fig. 4.4a and Fig. 4.4b results are shown for meshes of size $N = 6240 \, (40 \times 39)$ and $N = 15680 \, (70 \times 56)$, respectively. We observe the location of touchdown is robust as the mesh size increases. The set $S_\Omega$ meets the boundary $\partial\Omega$ and so the skeleton arrival time satisfies $t_S = 0$.

As predicted by the analytical skeleton, there are four singularities close to each corner for small $\varepsilon$. As $\varepsilon$ increases, the four singularities move inwards along $S_\Omega$ merging first into two

(a) Skeleton with mesh size
$N = 6240 \ (40 \times 39)$.

(b) Skeleton with mesh size
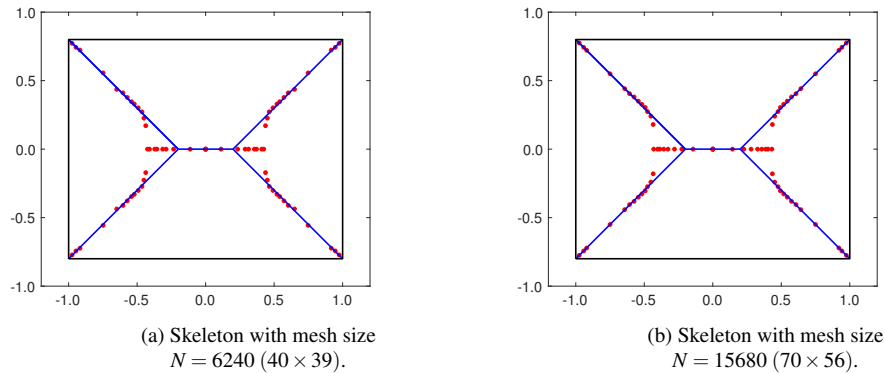$N = 15680 \ (70 \times 56)$.

Figure 4.4: Skeleton for rectangular domain (solid blue) with numerically obtained touchdown locations (red dots). Figs. 4.4a and 4.4b show results obtained with mesh sizes $N = 6240 \ (40 \times 39)$ and $N = 15680 \ (70 \times 56)$ respectively.



(a) Mesh at touchdown,
$\varepsilon = 0.02$.

(b) Mesh at touchdown,
$\varepsilon = 0.068$.

(c) Mesh at touchdown,
$\varepsilon = 0.1$.

(d) Solution at touchdown, $\varepsilon = 0.02$.

(e) Solution at touchdown, $\varepsilon = 0.068$.

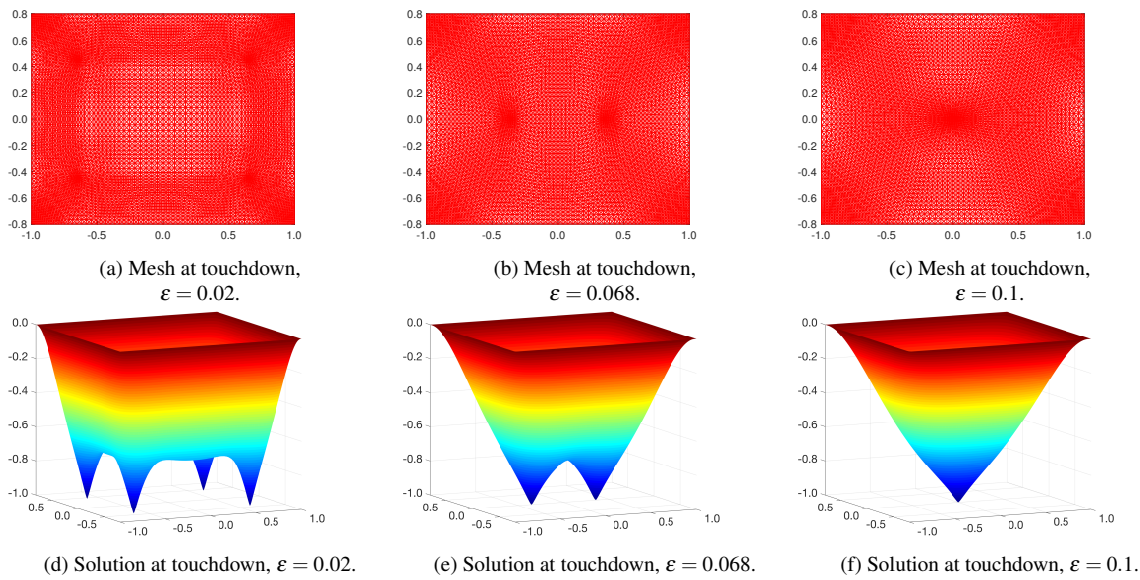(f) Solution at touchdown, $\varepsilon = 0.1$.

Figure 4.5: The profiles $u(\mathbf{x}, t)$ of (4.1) and associated meshes very close to singularity for $\varepsilon = 0.02$, $\varepsilon = 0.068$ and $\varepsilon = 0.1$ in the rectangle $(-1, 1) \times (-0.8, 0.8)$. The mesh size is $N = 15680 \ (70 \times 56)$.
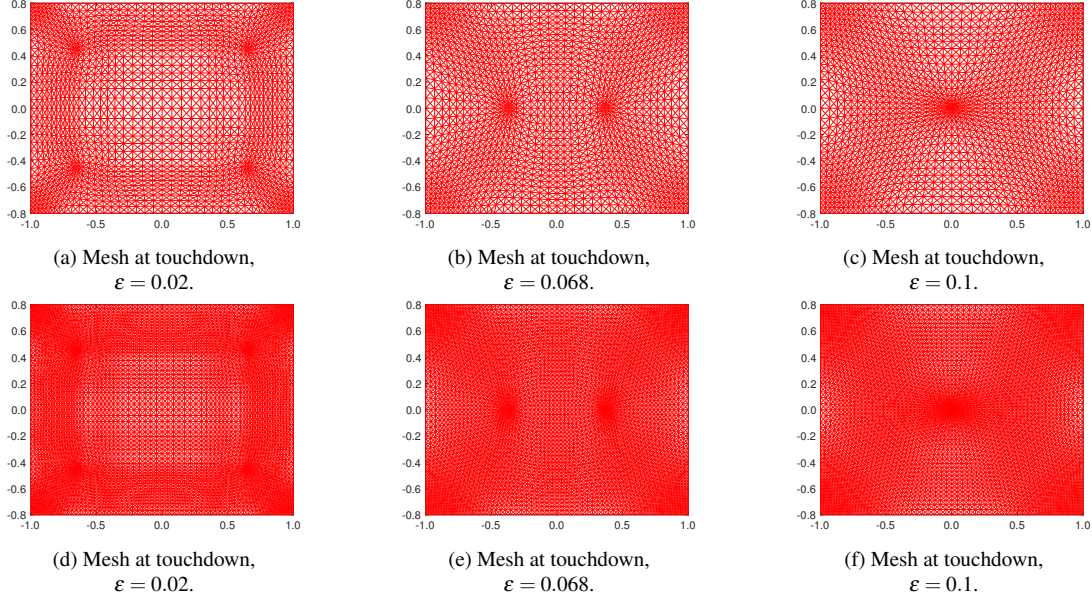
Figure 4.6: The profiles $u(\mathbf{x},t)$ of (4.1) and associated meshes very close to singularity for $\varepsilon = 0.02$, $\varepsilon = 0.068$ and $\varepsilon = 0.1$ in the rectangle $(-1,1) \times (-0.8,0.8)$. The top row is obtained by mesh size $N = 6240\,(40 \times 39)$, and the bottom row is obtained by mesh size $N = 15680\,(70 \times 56)$.

singularities and, as $\varepsilon$ increases, eventually into one. The final mesh and solution for values $\varepsilon = 0.02$, 0.068 and 0.1 are shown in Fig. 4.5. In each case shown in Figs. 4.5d-4.5f, the numerical algorithm correctly locates the position and multiplicity of the forming singularities and increases local mesh density in their vicinity to accurately resolve the solution. To demonstrate that the solution is robust with respect to grid refinement, we present the final mesh for $\varepsilon = 0.02$, 0.068 and 0.1 obtained with mesh size $N = 6240\,(40 \times 39)$ and $N = 15680\,(70 \times 56)$ in Fig. 4.6.

In comparing $S_\Omega$ with the numerical touchdown points, we see that at smaller values of $\varepsilon$ (for which the singularities are confined to the corners) the set $S_\Omega$ accurately predicts the touchdown set. At larger values of $\varepsilon$, in particular those at which the four singularities merge into two, we observe that $S_\Omega$ has reduced accuracy in predicting the contact set. This reduction in the quality of the prediction is not surprising considering the asymptotic formulation relies on the peaks being well separated at touchdown which is not valid for larger $\varepsilon$ values. Nevertheless, the skeleton theory gives a qualitatively accurate description of the possible touchdown locations and multiplicities.

In Fig. 4.7 we display the evolution of the solution to (4.1) for the fixed value $\varepsilon = 0.02$ and several temporal snapshots with the accompanying mesh. For this value of $\varepsilon$, touchdown is ob-

served at four points simultaneously. At short times (Fig. 4.7a), the computational mesh is adapted to the propagating boundary layers emanating around $\partial \Omega$. By the touchdown time (Fig. 4.7f), the mesh generation algorithm allocates resources between each of the four forming singularities and the sharp ridges that join them.
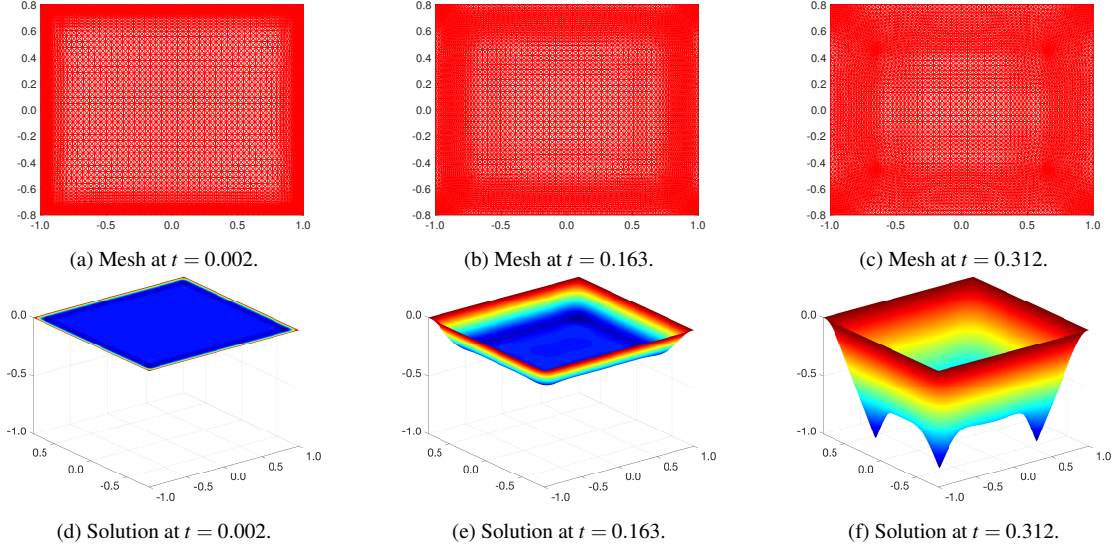


(a) Mesh at $t = 0.002$.

(b) Mesh at $t = 0.163$.

(c) Mesh at $t = 0.312$.

(d) Solution at $t = 0.002$.

(e) Solution at $t = 0.163$.

(f) Solution at $t = 0.312$.

Figure 4.7: Evolution of the solution of (4.1) and the associated mesh for $\varepsilon = 0.02$ in the rectangular domain for three time instants.

**Example 4.3.2** (Rectangular domain with a hole). Here we consider the rectangular domain $\Omega = (-1,1) \times (-0.8, 0.8)$, with a circular hole of radius 0.2, centered at $(0.2, 0.3)$. In this example $\Omega$ is non-convex.

For this example, we have found that it is important to keep a level of mesh concentration around the hole. To this end, we modify the metric tensor as

$$\tilde{\mathbb{M}}_K = \mathbb{M}_K + \beta I, \tag{4.12}$$

where $\mathbb{M}_K$ is defined as

$$\beta = \left[ e^{4(\sqrt{(x-0.2)^2 + (y-0.3)^2} - 0.2)} - 1 + \frac{2}{\max_{K \in \mathscr{T}_h} \sqrt{\det(\mathbb{M}_K)}} \right]^{-1}.$$

Notice that for $(x, y)$ on the circle, this gives

$$\tilde{\mathbb{M}}_K = \mathbb{M}_K + \frac{1}{2} \max_{K \in \mathscr{T}_h} \sqrt{\det(\mathbb{M}_K)} \, I,$$

which will give a level of mesh concentration around the circle comparable to that in the regions with largest $\sqrt{\det(\mathbb{M}_K)}$. The exponential term makes $\beta$ decrease sufficiently fast such that the mesh elements are not over concentrated near the circle.

The skeleton $S_\Omega$ of the domain which is displayed in Fig. 4.8. In this example $S_\Omega$ is formed from straight line segments that originate from each corner and are linked by four curved segments contorted around the hole. The expressions for the parabolic segments of $S_\Omega$ are found analytically by considering the points that are equidistant from the boundary of the outer rectangle and the perturbing hole.

The presence of the hole breaks the symmetry of the domain. In simulations, we observe that this precludes touchdown at multiple points simultaneously, except for certain fixed values of $\varepsilon$. Simultaneous touchdown at multiple points, as observed in the previous example of the rectangle with no hole, relies on the symmetric properties of the domain. In the absence of such symmetries, single point touchdown is the expectation for solutions of equation (4.1). However, as is clear from the solution profile of (4.1) for $\varepsilon = 0.044$ shown in Fig. 4.9e, the solution may be forming multiple troughs. When there are multiple troughs present, the singularity location will be selected by the trough which has the lowest value as the singularity is approached. In terms of applications to MEMS, each of these troughs can form contacts between the two surfaces and are important to track. We remark that $S_\Omega$ describes a set of potential points at which the asymptotic solution has a local minimum and therefore considers all potential contact locations.

One interesting observation from the skeleton and singularity points shown in Fig. 4.8 is that the track of the first touchdown point does not vary continuously with $\varepsilon$. We observe that the first singularity point switches between branches several times suggesting that multiple simultaneous singularities are possible only at fixed values of $\varepsilon$. In Figs. 4.9 and 4.10, single point touchdown
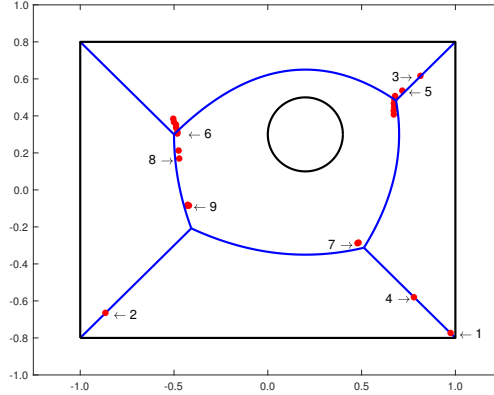
Figure 4.8: Skeleton of rectangular domain hole (blue solid line) and numerically computed touchdown locations (red dots). The points marked $1-9$ correspond to the first touchdown location for solutions of (4.1) for values $\varepsilon = 10^{-4}$, $2.662 \times 10^{-3}$, $5.2 \times 10^{-3}$, $7.78 \times 10^{-3}$, $0.01$, $0.036$, $0.044$, $0.051$, and $0.06$, respectively. The solution and mesh for Mark 5 ($\varepsilon = 0.01$), Mark 7 ($\varepsilon = 0.044$), and Mark 9 ($\varepsilon = 0.06$) are shown in Fig. 4.9.

is observed, however, other troughs in the solution are also very close to singularity which helps explain the sensitivity of the touchdown set on $\varepsilon$.



(a) Mesh at touchdown, $\varepsilon = 0.01$.



(b) Mesh at touchdown, $\varepsilon = 0.044$.



(c) Mesh at touchdown, $\varepsilon = 0.06$.



(d) Solution at touchdown, $\varepsilon = 0.01$.



(e) Solution at touchdown, $\varepsilon = 0.044$.



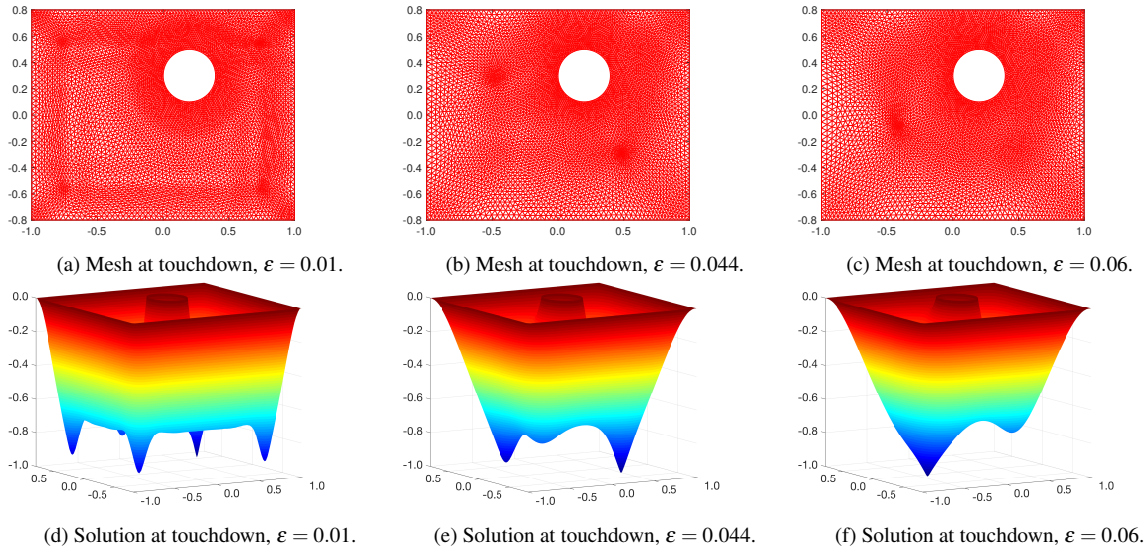(f) Solution at touchdown, $\varepsilon = 0.06$.

Figure 4.9: Solutions of (4.1) and meshes at singularity for values $\varepsilon = 0.01, 0.044, 0.1$ in the rectangular domain with hole.

**Example 4.3.3** (Asymmetric Domain). We consider the asymmetric domain given in polar coordinates by

$$(x, y) = r(\theta)(\cos\theta, \sin\theta), \qquad r(\theta) = 1 + (0.15 \sin 2\theta + 0.3 \cos 3\theta). \tag{4.13}$$

(a) Mesh at $t = 0.035$.　　　　(b) Mesh at $t = 0.275$.　　　　(c) Mesh at $t = 0.311$.



(d) Solution at $t = 0.035$.　　　　(e) Mesh at $t = 0.275$.　　　　(f) Mesh at $t = 0.311$.
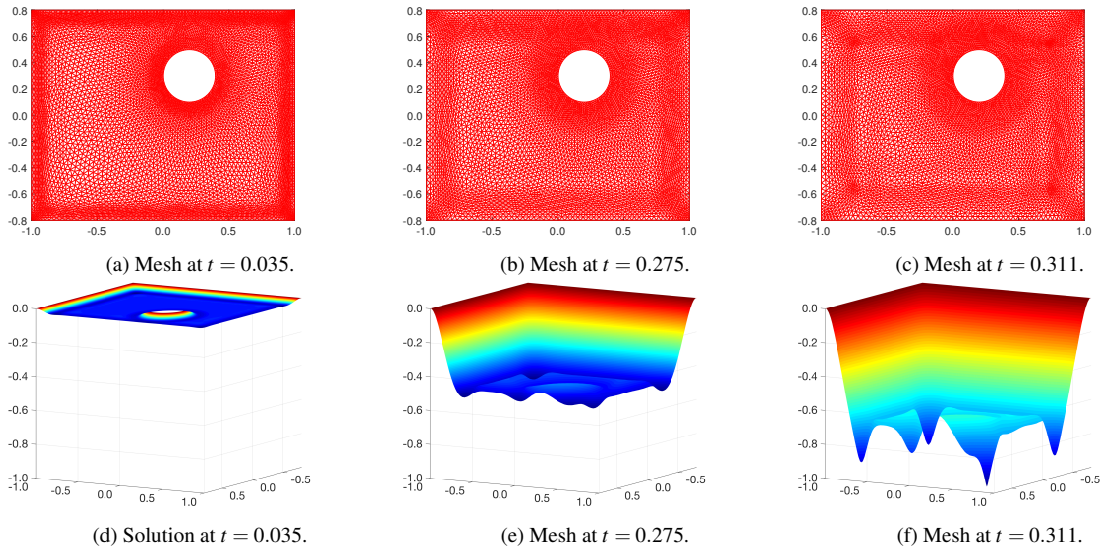
Figure 4.10: The evolution of the solution for $\varepsilon = 0.01$. The mesh size is $N = 11658$.
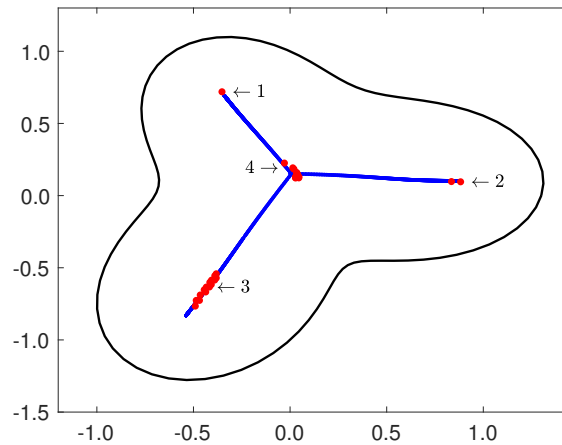


Figure 4.11: Skeleton and touchdown points for the non-symmetric domain (4.13). The points marked $1-4$ correspond to the first touchdown location for solutions of (4.1) for values $\varepsilon = 0.02, 0.024, 0.04, 0.092$, respectively.

In Fig. 4.11 the skeleton $S_\Omega$ for the domain is displayed along with the first touchdown locations that arise from the parameter values $\varepsilon \in (0.02, 0.1)$. As $\varepsilon$ increases, the singularity moves along each of the three branches of the skeleton before becoming fixed near the center of the domain. As with Example 4.3.2, we see that the track of the first touchdown location does not vary continuously with $\varepsilon$. For the parameter values $\varepsilon = 0.02\,(\text{Mark }1), 0.024\,(\text{Mark }2), 0.04\,(\text{Mark }3), 0.092\,(\text{Mark }4)$ marked on Fig. 4.11, we show snapshots of the evolution of the solution in Figs. 4.12-4.15, respectively.

In Fig. 4.12f the solution of (4.1) close to singularity is shown for $\varepsilon = 0.02$ and three distinct troughs in the solution are clear. The trough with the lowest value, and the one that contacts first, is centered at Mark 1 in Fig. 4.11. For the slightly increased parameter value $\varepsilon = 0.024$ the solution close to touchdown is shown in Fig. 4.13f. At this value, the qualitative solution features look very similar, however, the center of the lowest trough is now shifted to Mark 2 on a separate branch of $S_\Omega$. At the value $\varepsilon = 0.04$, with final profile shown in Fig. 4.14f, the lowest point has shifted again and is now centered on the third arm of $S_\Omega$ at Mark 3 on Fig. 4.11. These observations suggest that in this asymmetric case simultaneous two point touchdown can occur for particular fixed values of $\varepsilon$ in the ranges $(0.02, 0.024)$ and $(0.024, 0.4)$.

At the larger value $\varepsilon = 0.092$, the snapshots in Fig. 4.15 show that the three peaks merge very quickly in the evolution of the solution. By the time the solution of (4.1) is close to singularity at this value of $\varepsilon$, the solution has only one trough which is centered close to the geometric center of the domain at Mark 4 in Fig. 4.11.

In each of the intermediary evolution plots in Figs. 4.12-4.15, the mesh is seen to be accurately capturing the firestorm set $\omega(t)$. In this solution regime, the adaptive algorithm allocates grid resolution to the vicinity of $\partial\Omega$ in order to capture this expanding boundary layer. The third snapshot of the solution is taken very close to touchdown and the mesh has adapted to increase the resolution in the vicinity of the forming singularities. This shows the numerical method capturing multiple types of dynamic fine scale solution modalities.

## 4.4 Conclusions

In this chapter, we have presented an investigation into the influence of geometry and parameter values on the location of singularities in a fourth-order PDE system modeling microscopic elastic-electrostatic deflections. The MMPDE method can automatically detect and resolve different types of dynamic features such as sharp interfaces and multiple forming singularities, with the advantage of being capable of accommodating the complex geometries and topological defects common in the design of real MEMS devices (cf. Fig. 4.1b).

(a) Mesh at $t = 0.010$.  (b) Mesh at $t = 0.232$.  (c) Mesh at $t = 0.310$.

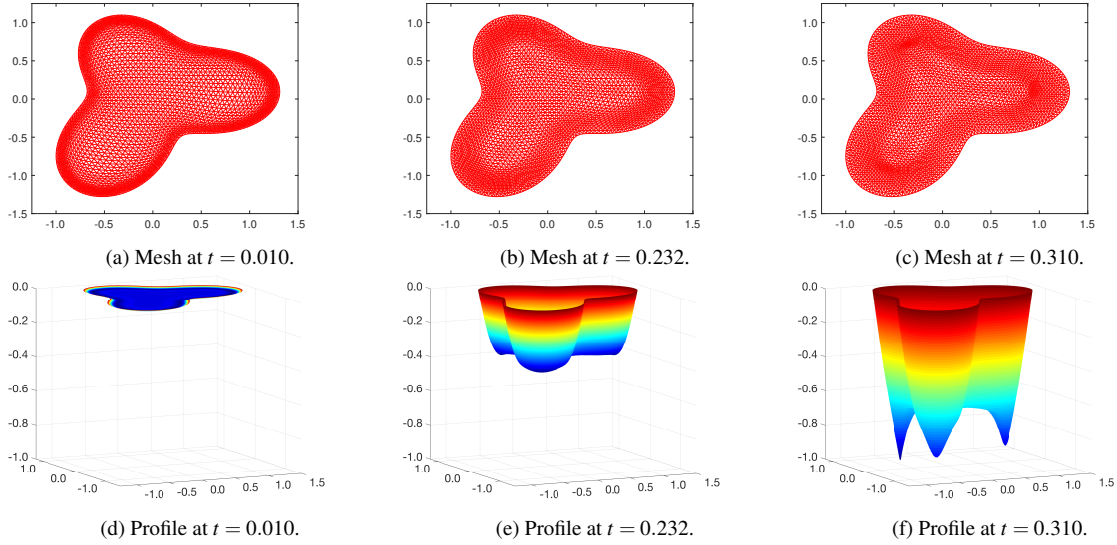(d) Profile at $t = 0.010$.  (e) Profile at $t = 0.232$.  (f) Profile at $t = 0.310$.

Figure 4.12: Three snapshots of the evolution of the solution of (4.1) and the mesh for $\varepsilon = 0.02$ (Mark 1 in Fig. 4.11). The mesh size is $N = 5244$.

To complement this numerical tool, we have used an asymptotic analysis to obtain the skeleton - a reduced representation of the domain which gives an estimate of the potential singularity locations. This analysis also reveals that the sensitive dependence of the contact set on the equation parameters and the shape of the domain $\Omega$ is due to a non-monotone boundary layer profile. The superposition of the solution along rays emanating from $\partial\Omega$ lowers the value of the solution at
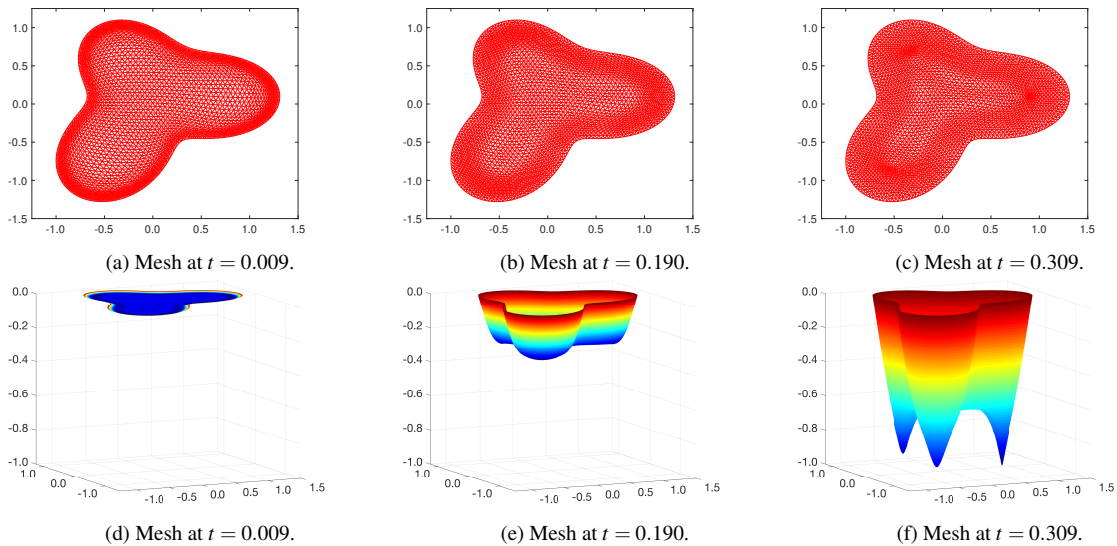


(a) Mesh at $t = 0.009$.  (b) Mesh at $t = 0.190$.  (c) Mesh at $t = 0.309$.

(d) Mesh at $t = 0.009$.  (e) Mesh at $t = 0.190$.  (f) Mesh at $t = 0.309$.

Figure 4.13: Three snapshots of the evolution of the solution of (4.1) and the mesh for $\varepsilon = 0.024$ (Mark 2 in Fig. 4.11). The mesh size is $N = 5244$.

(a) Mesh at $t = 0.009$.     (b) Mesh at $t = 0.280$.     (c) Mesh at $t = 0.303$.

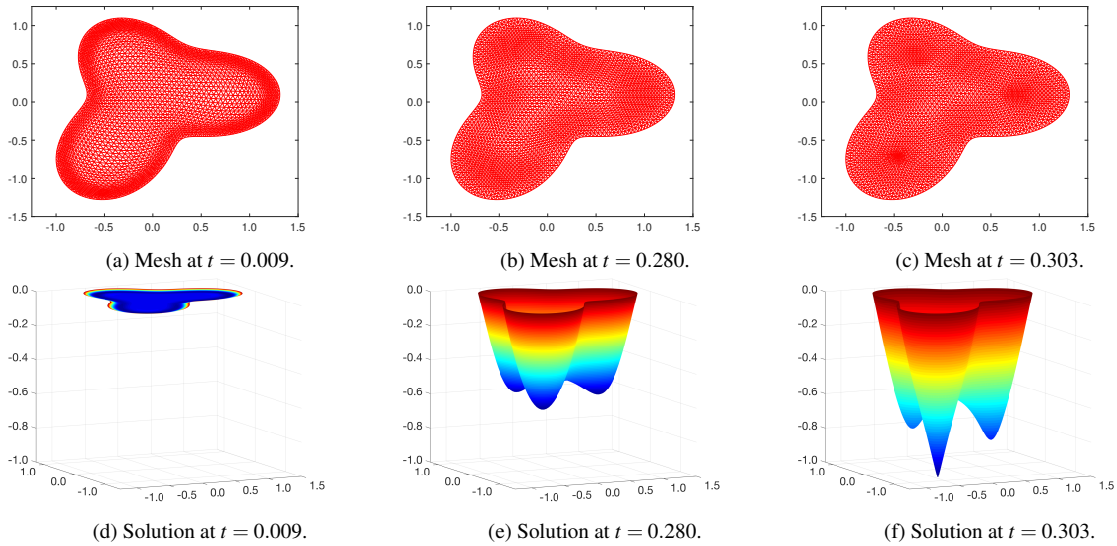(d) Solution at $t = 0.009$.     (e) Solution at $t = 0.280$.     (f) Solution at $t = 0.303$.

Figure 4.14: The evolution of the solution of (4.1) and the mesh for $\varepsilon = 0.04$. The mesh size is $N = 5244$.

certain points in the domain which then become more likely to be singularity locations. We find that the skeleton gives a good qualitative description of the possible contact sets. The quantitative accuracy of the skeleton is variable and in particular we find it to be diminished in non-simply connected domains. For engineers seeking to prevent the two surfaces coming into physical contact through the placement of deflection limiters [45], the skeleton provides a good estimate of the points at which these should be centered.
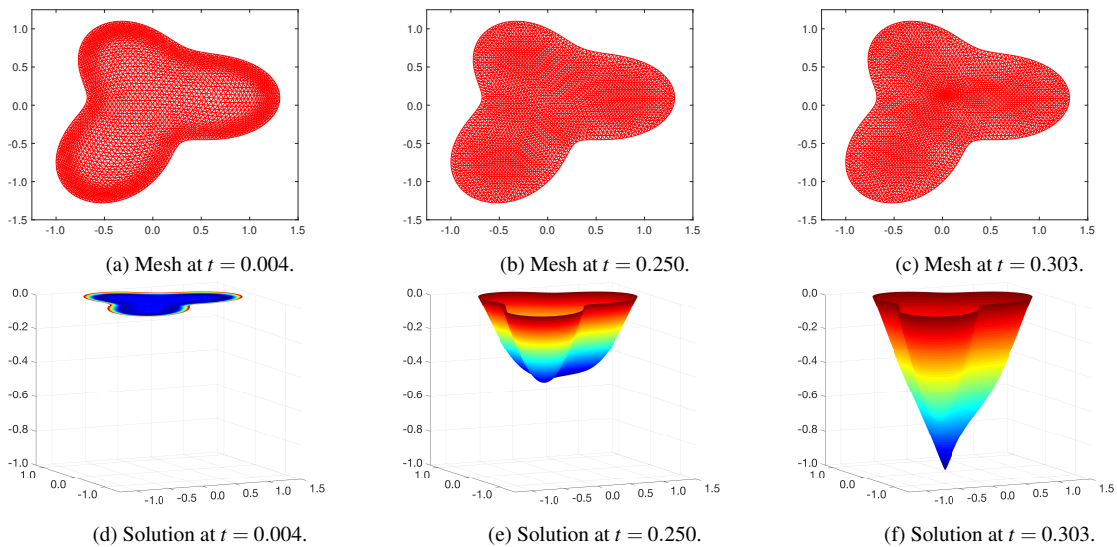


(a) Mesh at $t = 0.004$.     (b) Mesh at $t = 0.250$.     (c) Mesh at $t = 0.303$.

(d) Solution at $t = 0.004$.     (e) Solution at $t = 0.250$.     (f) Solution at $t = 0.303$.

Figure 4.15: The evolution of the solution of (4.1) and the mesh for $\varepsilon = 0.092$. The mesh size is $N = 5244$.

# Chapter 5

# Permanent Charge Effects on Ionic Flow: a Numerical Study of a Flux Ratio and Bifurcation

## Abstract

Ionic flow, transportation of ions through ion channels across cell membrane, carries electric signals for cells to communicate with each other. The permanent charge of an ion channel is the crucial structure for ionic flow properties of the channel while boundary conditions are the driving force for the ionic flow. The effects of permanent charges interacting with boundary conditions have been studied analytically via a quasi-one-dimensional Poisson-Nernst-Planck model for small permanent charges and for large permanent charges. The analytical studies lead to an introduction of a flux ratio which seems to be appropriate for the purpose. The flux ratio has a number of specifics for the interacting of permanent charges with boundary conditions and a universal property. The objective of our work is to combine the advantages of analysis and numerics to examine the effects of permanent charges on individual fluxes, extending the results to general permanent charge cases. In this chapter, I will present results of numerical investigation on the flux ratio to bridge between the two extrema of small and large permanent charges. As expected, our numerical results verify the analytical predictions for the two extrema. On the other hand, non-trivial behavior emerges as one varies the permanent charge from small to large, in particular, bifurcations of flux ratios are revealed, showing the rich phenomena of permanent charge effects by the power of combining the analytical and numerical studies. The MMPDE method has been applied which is critical due to the presence of Debye layers at the interface between the permanent

charge regions and uncharged regions of ion channels.

## 5.1  Ion channels and Poisson-Nernst-Planck type models

Ion channels are large proteins embedded on the membrane of cells. They serve as a major way for cells to interact with each other and connect to the outside world. Once the channels are open, ions flow from one side to the other, producing electric signals that control many biological functions. Within an ion channel, amino acid side chains are distributed, with acidic side chains contributing negative charges, and basic side chains contributing positive charges. For example, the ionic flow can create trans-membrane potentials that carry nerve signals. Two key structures of an ion channel are the channel shape and the permanent charge. The ion channels typically have a relatively narrow neck, where the permanent charge is distributed.

The basic models for electrodiffusion are self-consistent Poisson-Nernst-Planck (PNP) type models. The PNP type models consider open stage of channels, and treat the medium implicitly as dielectric continuum. These systems are continuum models, not direct limits of molecular dynamic models. PNP type models miss details of motions of individual ions but capture all thermodynamic quantities of the ionic mixture, such as, fluxes, pressure, and energy. PNP systems can be viewed as the Fokker-Planck systems from molecular dynamic models ([72]), and they can be also derived from Boltzmann equations ([4]) and from variational principles ([37, 39, 40]).

The movements of various types of ions through membrane channels with different structures involves multiple physical parameters that interact with each other nonlinearly and globally. Analysis based on PNP has revealed a number of interesting, some counterintuitive, phenomena of permanent charges effects, for two extremum situations, small permanent charge and large permanent charge cases. It is interesting to mention that it used to be taken as granted, that the permanent charge always promotes the ion species with opposite charge signs, and decreases the ion species with the same charge sign as the permanent charge. However, it has been analytically proven via a quasi-one-dimensional PNP model in [43] that for small permanent charge, the selectivity of ion species are not monotone with respect to permanent charge. Besides, many biologists believe that

59

if the gradient of electrochemical potential across the channel is increased in magnitude, the flux through the channel should increase. This has been proven false in [84], where the effects of large permanent charge on flux selectivity has been studied analytically. The *declining phenomenon* has been observed, i.e., the flux of ions with the opposite sign as the permanent charge in a channel can decrease dramatically as the driving force increases.

PNP type systems are primitive models for ionic flows that treat the aqueous medium (where salts are dissolved into free ions and ions are migrating) as dielectric continuum. PNP systems can be derived as reduced continuum models from molecular dynamic Langevin models [72], from Boltzmann equations [4], and from variational principles [38, 41, 31, 82]. For an ionic mixture with $n$ ion species, PNP reads

$$
\nabla \cdot \left( \varepsilon_r(\mathbf{r}) \varepsilon_0 \nabla \Phi \right) = -e_0 \Big( \sum_{s=1}^{n} z_s C_s + \mathscr{Q}(\mathbf{r}) \Big),
$$

$$
\nabla \cdot \vec{\mathscr{J}}_k = 0, \qquad -\vec{\mathscr{J}}_k = \frac{1}{k_B T} \mathscr{D}_k(\mathbf{r}) C_k \nabla \mu_k, \qquad k = 1, 2, \cdots, n
$$

(5.1)

where $\Omega$ is a three-dimensional cylindrical-like domain representing the channel, $\mathbf{r} \in \Omega$, $\mathscr{Q}(\mathbf{r})$ is the permanent charge density, $\varepsilon_r(\mathbf{r})$ is the relative dielectric coefficient, $\varepsilon_0$ is the vacuum permittivity, $e_0$ is the elementary charge, $k_B$ is the Boltzmann constant, $T$ is the absolute temperature, $\Phi$ is the electric potential, and, for the $k$th ion species, $C_k$ is the concentration, $z_k$ is the valence (the number of charges per particle), $\mu_k$ is the electrochemical potential depending on $\Phi$ and $\{C_j\}$, $\vec{\mathscr{J}}_k$ is the flux density vector, and $\mathscr{D}_k(\mathbf{r})$ is the diffusion coefficient.

The Poisson equation for the electrical potential $\Phi$ (the first equation in (5.1)) is the continuum version of Coulomb's Law. The Nernst-Planck equation (the second equation in (5.1)) describes the steady state of the conservation of mass of the ionic flow. The major modeling component is the electrochemical potential $\mu_k$. It is often expressed into two terms $\mu_k = \mu_k^{id} + \mu_k^{ex}$, where $\mu_k^{id}$ and $\mu_k^{ex}$ ideal and excess components, respectively. The ideal component is

$$
\mu_k^{id}(X) = z_k e_0 \Phi(X) + k_B T \ln \frac{C_k(X)}{C_0},
$$

where $C_0$ is a characteristic concentration. The first term is the electric potential while the second term is the ideal "gas" potential. The excess component $\mu_k^{ex}$ accounts for ion-to-ion interactions and ion size effects, and multiple models for $\mu_k^{ex}$ have been established. Unless specified, we consider only the ideal component $\mu_k^{id}$ of the electrical potential.

Since ion channels have narrow cross-sections relative to their lengths, the three-dimensional systems (5.1) can further be reduced to quasi-one-dimensional models, which are first proposed in [62], and a special case of the reduction is justified in [57]. The quasi-one-dimensional PNP boundary value problem reads as

$$\frac{1}{A(X)}\frac{d}{dX}\left(\varepsilon_r(X)\varepsilon_0 A(X)\frac{d\Phi(X)}{dX}\right) = -e_0\left(\sum_{s=1}^{n} z_s C_s(X) + \mathcal{Q}(X)\right),$$

$$\frac{d\mathcal{J}_k}{dX} = 0, \qquad -\mathcal{J}_k = \frac{1}{k_B T}\mathcal{D}_k(X)\mathscr{A}(X)C_k(X)\frac{d\mu_k}{dX}, \qquad k = 1,...,n \tag{5.2}$$

subject to the boundary conditions (see [19])

$$\Phi(a_0) = \mathscr{V}, \qquad C_k(a_0) = \mathscr{L}_k > 0; \qquad \Phi(b_0) = 0, \qquad C_k(b_0) = \mathscr{R}_k > 0, \tag{5.3}$$

where $X \in [a_0, b_0]$ is the coordinate along the axis of the channel, and $A(X)$ is the area of the cross section at location $X$.

To non-dimensionalize the quasi-one-dimension PNP, we introduce the dimensionless variables as

$$\varepsilon^2 = \frac{\varepsilon_r \varepsilon_0 k_B T}{e_0^2(b_0 - a_0)^2 C_0}, \qquad x = \frac{X - a_0}{b_0 - a_0}, \qquad h(x) = \frac{A(X)}{(b_0 - a_0)^2}, \qquad Q(x) = \frac{\mathcal{Q}(X)}{C_0},$$

$$D(x) = \mathcal{D}(X), \qquad \phi(x) = \frac{e_0}{k_B T}\phi(X), \qquad c_k = \frac{C_k(x)}{C_0}, \qquad J_k = \frac{\mathcal{J}_k}{(b_0 - a_0)C_0 \mathcal{D}_k}, \tag{5.4}$$

$$\bar{\mu}_k(x) = \frac{1}{k_B T}\mu_k(X), \qquad V = \frac{e_0}{k_B T}\mathscr{V}, \qquad L_k = \frac{\mathscr{L}_k}{C_0}, \qquad R_k = \frac{\mathscr{R}_k}{C_0}.$$

61

The dimensionless quasi-one-dimension PNP reads as

$$-\frac{d}{dx}\left(\varepsilon^2 h(x)\frac{d\phi}{dx}\right) = h(x)\left(z_1 c_1 + z_2 c_2 + Q(x)\right),$$

$$\frac{dJ_k}{dx} = 0, \qquad -J_k = D_k(x)h(x)c_k\frac{d\bar{\mu}_k}{dx}, \qquad k = 1,2$$

(5.5)

with the boundary conditions at $x = 0$ and $x = 1$

$$\phi(0) = V, \qquad c_k(0) = L_k; \qquad \phi(1) = 0 \qquad c_k(1) = R_k. \tag{5.6}$$

In this work, we consider an ionic mixture of two ion species with $z_1 > 0 > z_2$. We also assume that the dielectric coefficient $\varepsilon$ is a constant and there hold the electroneutrality boundary conditions

$$z_1 L_1 + z_2 L_2 = 0 = z_1 R_1 + z_2 R_2.$$

The reason for the electroneutrality boundary conditions is that, otherwise, there will be sharp boundary layers which cause significant changes (large gradients) of the electric potential and concentrations near the boundaries so that a measurement of these values has non-trivial uncertainties. We point out that the geometric singular perturbation framework for PNP type models developed in [19, 55] can treat the case without the electroneutrality assumption; in fact, at the "foot" of the boundary layers the concentrations can be determined by the boundary conditions directly and satisfy electroneutrality condition.

Ideally, the experimental designs should not affect the intrinsic ionic flow properties. Thus the electroneutral boundary conditions are enforced. Without the electroneutrality boundary conditions, sharp boundary layers which cause significant changes of electric potential and concentrations near the boundaries. On the other hand, the "landing point" of the $\varepsilon = 0$-limiting boundary layer meets the electroneutrality condition and can be determined directly from the original boundary conditions.

In the dimensionless form, $\bar{\mu}_k$ can also be written as $\bar{\mu}_k = \mu_k^{id} + \mu_k^{ex}$, where $\mu_k^{id} = z_k\phi + \ln c_k$

and $\mu_k^{ex}$ is taken to be zero for most cases.

The variable cross-section area is chosen to reflect the fact that the channel is much narrow in the neck ($\frac{1}{3} < x < \frac{2}{3}$) than other region [43]. In this work, we choose the channel geometry as

$$
h(x) = \begin{cases}
3\left(0.4x + 20(\frac{1}{3} - x)\right), & 0 \leq x < \frac{1}{3} \\
3\left(0.4(x - \frac{1}{3}) + 0.4(\frac{2}{3} - x)\right), & \frac{1}{3} \leq x < \frac{2}{3} \\
3\left(20(x - \frac{2}{3}) + 0.4(1 - x)\right), & \frac{2}{3} \leq x < 1.
\end{cases}
\tag{5.7}
$$

As in [43], we assume the permanent charge is distributed on the neck of the channel as

$$
Q(x) = \begin{cases}
0, & 0 < x < \frac{1}{3} \\
Q_0, & \frac{1}{3} < x < \frac{2}{3} \\
0, & \frac{2}{3} < x < 1.
\end{cases}
\tag{5.8}
$$

In addition, we choose $D_1 = D_2 = 1$, $z_1 = 1$, $z_2 = -1$, $\varepsilon = 10^{-5}$, and $L_1 = L_2 = L$, $R_1 = R_2 = R$.

In computation, the discontinuity of $Q(x)$ and $h(x)$ at $a = \frac{1}{3}$ and $b = \frac{2}{3}$ is likely to cause divergence when applying Newton's method to solve for the nonlinear system resulting from discretization of (5.5). To avoid this difficulty, we apply a regularization on $Q(x)$ and $h(x)$ as

$$
Q_\delta(x) = Q_0\left(\tanh\left(\delta(x - \frac{1}{3})\right) - \tanh\left(\delta(x - \frac{2}{3})\right)\right),
\tag{5.9}
$$

and

$$
h_{\delta_x}(x) = \begin{cases}
3[0.4x + 20(\frac{1}{3} - x)], & 0 \leq x < \frac{1}{3} - \delta_x \\
\tilde{a}(x - \frac{1}{3} - \delta_x) + 0.4, & \frac{1}{3} - \delta_x \leq x < \frac{1}{3} + \delta_x \\
3[0.4(x - \frac{1}{3}) + 0.4(\frac{2}{3} - x)], & \frac{1}{3} + \delta_x \leq x < \frac{2}{3} - \delta_x \\
\tilde{a}(x - \frac{2}{3} + \delta_x) + 0.4, & \frac{2}{3} - \delta_x \leq x < \frac{2}{3} + \delta_x \\
3[20(x - \frac{2}{3}) + 0.4(1 - x)], & \frac{2}{3} + \delta_x \leq x < 1
\end{cases}
\tag{5.10}
$$

where $\delta > 0$ and $\delta_x > 0$ are regularization parameters and

$$\tilde{a} = \frac{y_1 - 0.4}{4\delta_x^2}, \qquad y_1 = 3[0.4(\frac{1}{3} - \delta_x) + 20\delta_x].$$

It can be verified that as $\delta \to \infty$, $Q_\delta(x) \to Q(x)$ in $L^2$ norm, and $h_{\delta_x}(x) \to h(x)$ for $x \in [0,1]$ as $\delta_x \to 0$.

## 5.2   A flux raatio for permanent charge effects

The major concern for an ion channel is the fluxes $J_k$'s of individual ion species. More precisely, one would like to understand how individual fluxes depend on the channel structure and boundary conditions. On the other hand, only the total current $\mathscr{I} = \sum_{k=1}^n z_k \mathscr{J}_k$ is measured in most experiments and individual ionic fluxes $J_k$'s are difficult to measure directly. In fact, to measure the flux of sodium in the sodium-chloride ($Na^+Cl^-$) solutions, a small amount of a radioactive isotope of sodium is typically added, the flux of this isotope is measured by its radioactivity, and the flux of sodium is then estimated using the flux of the isotope; see, for example, [30, 42, 78] for detail. As such, analytical and numerical studies of the PNP systems are crucial for understanding and gaining insights to flux dynamics, channel properties, and effects of permanent charge on each single species.

To study the effects of permanent charge on fluxes, the flux ratios have been recently introduced in [54] as

$$\lambda_k(Q; V, L, R, h) = \frac{J_k(Q; V, L, R, h)}{J_k(0; V, L, R, h)}, \qquad k = 1, 2 \tag{5.11}$$

where $J_k(Q; V, L, R, h)$ is the flux of the $k$th species with permanent charge density $Q$ and the boundary conditions (5.6), and $J_k(0; V, L, R, h)$ is the flux given the same boundary conditions and 0 permanent charge. It has been observed in [20] that $J_k(Q; V, L, R, h)$ and $J_k(0; V, L, R, h)$ have the same sign as $(\bar{\mu}_k(0) - \bar{\mu}_k(1))$, which is determined by the boundary condition $(V, L, R)$ and independent of the permanent charge, and so $\lambda_k > 0$ for any $Q$.

It follows from the definition that the permanent charge promotes the flux when $\lambda_k > 1$, and vice versa. Thus the relation $\lambda_k = 1$ determines the boundary sets of the parameter space $(Q,V,L,R,h)$ separating the region over which the permanent charge promotes the flux $J_k$ from that over which the permanent charge reduces the flux $J_k$. Note that, with $L$, $R$, and $h$ fixed, $\lambda_k$ is a function of $Q$ and $V$. One major research interest is to understand how the selectivity of each single species is affected by different permanent charge densities and voltages. Therefore, we study the effects of $Q$ and $V$ on $\lambda_1$ and $\lambda_2$, with fixed boundary conditions $L$, $R$ and channel geometry $h$. In addition, it is crucial to study the threshold where the selectivity of the species is changed. For this purpose, we take the advantage of numerical approach to locate the the parameter boundaries defined by $\lambda_k = 1$, which partitions the $Q - V$ space into regions defined by $\lambda_1 < \lambda_2 < 1$, $\lambda_1 < 1 < \lambda_2$, and $1 < \lambda_1 < \lambda_2$, which can hardly be obtained via analytical appraoch.

A universal property about the effects of permanent charges on fluxes of cation and anion has been established in [54] that, for general $Q(x) > 0$ (not necessarily the permanent charges of the form in (5.8)) and $z_1 > 0 > z_2$, as one would expect, the permanent charge always promotes the negative charged species more than the positive species, i.e., $\lambda_1(Q) < \lambda_2(Q)$, independent of boundary conditions and channel geometry. However, what could be against one's intuition is that $\lambda_1 < 1 < \lambda_2$ is not always the case.

Existing works have studied analytically how $\lambda_1$ and $\lambda_2$ depend on the combination of the channel geometry and the boundary conditions for small $Q_0$ ($0 < Q_0 \ll 1$) and for large $Q_0$, with $z_1 < 0 < z_2$. In [43], a singular perturbation analysis has been studied via a connecting problem of (5.5). The connecting problem has been constructed due to the jumps in $Q(x)$ and the conservation of the flux densities $J_k$ and first brought up in [19]. $J_k$ has been expanded in small $|Q_0|$ as

$$J_k = J_{k0} + J_{k1}Q_0 + J_{k2}Q_0^2 + o(Q_0^2), \tag{5.12}$$

and the zero order term $J_{k0}$ and first order term $J_{k1}$ have been derived via the connecting problem in [19]. By the definition of $\lambda_k$ as in (5.11), if $J_{k1}J_{k0} > 0$, the $k$th species is enhanced, and vice

versa.

It has been shown that the space of the parameters $(V, L, R, \alpha, \beta)$ is the union of three regions, $\Omega_1$ with $1 < \lambda_1 < \lambda_2$, $\Omega_2$ with $\lambda_1 < 1 < \lambda_2$, and $\Omega_3$ with $\lambda_1 < \lambda_2 < 1$. Conditions of $(V, L, R)$ corresponding to each specific situation has been derived. The critical potential, $V_q^k$, of the $k$th ion species, has been derived as a function of the boundary conditions and the channel geometry. More specifically, with $L$ and $R$ fixed, along the curves $\lambda_k(Q_0, V) = 1$ in the $(Q_0, V)$ space, we have $V \to V_q^k$ as $Q_0 \to 0$.

We now present the results in details from [43]. Let $L_1 = L_2 = L$ and $R_1 = R_2 = R$, and

$$t = L/R, \qquad \gamma(t) = \frac{t \ln t - t + 1}{(t-1) \ln t}, \qquad H(x) = \int_0^x h^{-1}(s) ds, \qquad \alpha = \frac{H(a)}{H(1)},$$

$$\beta = \frac{H(b)}{H(1)}, \qquad A = \frac{(\beta - \alpha)(L - R)^2}{((1-\alpha)L + \alpha R)((1-\beta)L + \beta R)}, \qquad (5.13)$$

$$B = \frac{(1-\beta)L + \beta R - \ln((1-\alpha)L + \alpha R)}{A}.$$

It has been proven that for $t > 1$,

- if $\alpha < \gamma(t)$, there exists a unique $\beta_1 \in (\alpha, 1)$, such that

  - $1 - B < 0$, for $\beta \in (\alpha, \beta_1)$,

  - $1 - B > 0$, for $\beta \in (\beta_1, 1)$,

- if $\alpha \geq \gamma(t)$, then $1 - B > 0$.

The critical potentials $V_q^1$ and $V_q^2$ are given by

$$V_q^1 = V_q^1(L, R) = -\frac{\ln L - \ln R}{z_2 (1 - B)}, \qquad V_q^2 = V_q^2(L, R) = -\frac{\ln L - \ln R}{z_1 (1 - B)}. \qquad (5.14)$$

We then have the following conclusion for small $Q_0$ values with $t = L/R > 1$:

- if $\alpha < \gamma(t)$, and $\beta \in (\alpha, \beta_1)$, then $V_q^1 < 0 < V_q^2$, and

66

- if $V < V_q^1$, $1 < \lambda_1 < \lambda_2$,

- if $V_q^1 < V < V_q^2$, $\lambda_1 < 1 < \lambda_2$.

- If $V > V_q^2$, $\lambda_1 < \lambda_2 < 1$,

• if $\alpha < \gamma(t)$ and $\beta > \beta_1$ or $\alpha \geq \gamma(t)$, then $V_q^1 > 0 > V_q^2$, and

- if $V > V_q^1$, $1 < \lambda_1 < \lambda_2$,

- if $V_q^2 < V < V_q^1$, $\lambda_1 < 1 < \lambda_2$,

- if $V < V_q^2$, $\lambda_1 < \lambda_2 < 1$.

Similar analytical results for $t = L/R < 1$ have been rigorously developed and justified. For more details, interested readers are referred to [43].

The above approach for small permanent charge $|Q|$ does not work for the case for large permanent charge $|Q|$. Using a significantly different approach, in [84], the properties of $\lambda_1$ and $\lambda_2$ with large $Q_0$ ($Q \gg 1$) have been studied via singular perturbation analysis. An expansion of the flux $J_k$ with respect to $v$, where $v = 1/Q_0$, has been brought up as

$$J_k(v) = J_{k0} + J_{k1}v + O(v^2). \tag{5.15}$$

The mathematical formulas of $J_{10}$, $J_{11}$, $J_{20}$, and $J_{21}$ have been derived. In particular,

$$J_{10} = 0, \qquad J_{20} = \frac{2\sqrt{LR}}{H(1)} \frac{1}{(1-\beta)\sqrt{L} + \alpha\sqrt{e^{-V}R}} (\sqrt{e^{-V}L} - \sqrt{R}). \tag{5.16}$$

and it has been proven that the following limits exist:

$$
\begin{aligned}
J_{10} = 0 \qquad & \lim_{V \to \infty} J_{20} = -\frac{1}{1-\beta}\frac{2R}{H(1)}, \qquad \lim_{V \to -\infty} J_{20} = \frac{1}{\alpha}\frac{2L}{H(1)}, \\
& \lim_{V \to \infty} J_{11} = -\lim_{V \to \infty} J_{21} = \frac{1}{(1-\beta)^2}\frac{((1-\beta)L + \alpha R)^2}{2H(1)(\beta - \alpha)}, \\
& \lim_{V \to -\infty} J_{11} = -\lim_{V \to -\infty} J_{21} = \frac{1}{\alpha^2}\frac{((1-\beta)L + \alpha R)^2}{2H(1)(\beta - \alpha)},
\end{aligned}
\tag{5.17}
$$

67

where $\alpha$, $\beta$ are defined in (5.13). In particular, the fact that $J_2$ is convergent is an indication of the saturation effect. As a result, $\lambda_k \to 0$ as $Q_0 \to \infty$, $V \to \pm\infty$.

Moreover, combining the results from [84] and [43], analytical asymptotes of the parametric boundaries $\lambda_2 = 1$ can be derived on the $Q_0 - V$ space. More specifically, by setting the ratio of the zero order terms in (5.15) and (5.12) equal to 1 as

$$-\frac{2z_2\sqrt{LR}(\sqrt{e^{-V}L} - \sqrt{R})(\ln L - \ln R)}{((1-\beta)\sqrt{L} + \alpha\sqrt{e^{-V}R})(L-R)(z_2V + \ln L - \ln R)} = 1, \tag{5.18}$$

one can obtain the critical potentials corresponding to the parameter boundaries $\lambda_2 = 1$. In other words, along each curve defined by $\lambda_2 = 1$ in the $Q_0 - V$ space, as $Q_0 \to \infty$, $V$ will converge to one of the solutions of equation (5.18).

## 5.3 New results (Numerical) for fixed $L$, $R$ and $h(x)$

Our major research interest is to extend the flux ratio studies to any value of $Q_0$. In this section, we study numerically how flux selectivity depends on the permanent charge density and the gradient of electrical potential. Consistent to the existing results, permanent charge does not necessarily restrain species with same sign or promote species with opposite sign. It is difficult, in most cases, to predict the region of magnitudes of permanent charge or boundary condition of $\phi$ that promotes or reduces any specie. A complete diagram of the flux selectivity is given based on these studies, where a couple of saddle-node bifurcations observed, which associates to the fact that the selectivity is usually not monotone with respect to $Q_0$ or $V$. Throughout this section, unless specified, we let $L = 0.008$, and $R = 0.001$. Note that these are scaled boundary values that are associated to the boundary values of the concentration that can are common in practice.

### 5.3.1 Dependence of $\lambda_1$ and $\lambda_2$ on $Q_0$ for fixed $V$

As described in the Sec 5.2, it is critical to identify boundaries separating the regions with different cases of $\lambda_1$ and $\lambda_2$, (i.e., $1 < \lambda_1 < \lambda_2$, $\lambda_1 < 1 < \lambda_2$, or $\lambda_1 < \lambda_2 < 1$). However, due to the difficulty in

analytics, it is not realistic to expect that the effects of permanent charge coupling with the driving force for electrodiffusion is fully studied analytically for all magnitudes of permanent charge. For this reason, we take the advantage of numerical methods, more specifically, the adaptive moving mesh finite element method, to derive a complete diagram of the effects of the permanent charge interacting with the gradient of the electrical potential. We have observed that the partition of different selectivities is rather complicated, with several saddle-node bifurcations taking place. We emphasize that no specific boundary conditions are chosen to obtain this complication.

In fact, we have observed the same bifurcation phenomenon, though different in quantities, for multiple different boundary conditions.

For this section, we will fix $(L, R, h)$ and examine how permanent charge effects on fluxes are interacted with the role of the electric potential $V$. Here we choose two values for $V$ and examine the dependence of $\lambda_k$ on $Q_0$. Fig. 5.1a, 5.1b, 5.1c and 5.1d show the trend of $\lambda_1$ and $\lambda_2$ for $V = 10$, $V = 50$, $V = -60$ and $V = -110$, respectively.

In Fig. 5.1a, starting from $\lambda_1 = \lambda_2 = 1$, one can observe that $\lambda_1 < 1$ and $\lambda_2 > 1$ for $Q_0 \in [0, 1]$. This is the case coinciding with one's intuition: the positive permanent charge helps promote the negative ion species, and inhibits the positive ion species. However, Fig. 5.1b, 5.1c and 5.1d demonstrates that $\lambda_1 < 1 < \lambda_2$ is not the only case that we can possibly obtain. For example, with $V = -110$, and for small $Q_0$, $\lambda_1 < \lambda_2 < 1$. As $Q_0$ increases, the graph of $\lambda_1$ and $\lambda_2$ can cross the value 1 multiple times. Indeed, we have observed all the three possibilities as described in Section 5.2: $\lambda_1 < \lambda_2 < 1$, $\lambda_1 < 1 < \lambda_2$, as well as $1 < \lambda_1 < \lambda_2$.

We remark that, for $Q_0 > 0$ small, Fig. 5.1 is consistent with the analytical prediction in [43] that has been described in Section 5.2. With $L = 0.008$, $R = 0.001$, $a = 1/3$, and $b = 2/3$, we have $V_q^1 = -V_q^2 = 18.97$, where $V_q^1$ and $V_q^2$ are defined as in (5.14). One can compute that $\alpha = 0.07$, $\beta = 0.93$, and $\beta_1 = 0.89$, where $\alpha$, $\beta$ and $\beta_1$ are as described in (5.13). Thus the set of boundary conditions corresponds to the case where $L/R > 1$, $\alpha < \gamma(L/R)$ (see (5.13)), and $\beta > \beta_1$. As described in Section 5.2, for small $Q_0$:
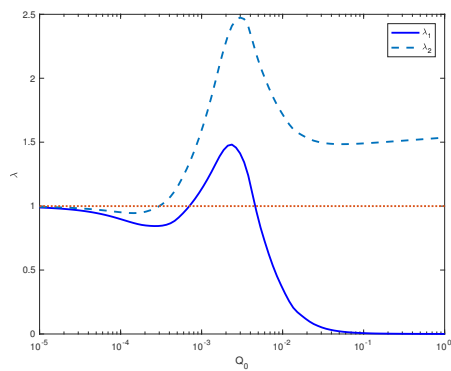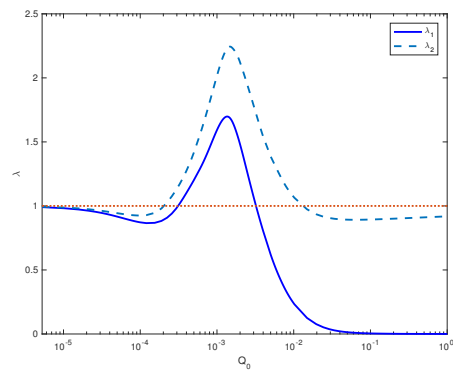
- If $V > 18.97$, $\lambda_2 > \lambda_1 > 1$,
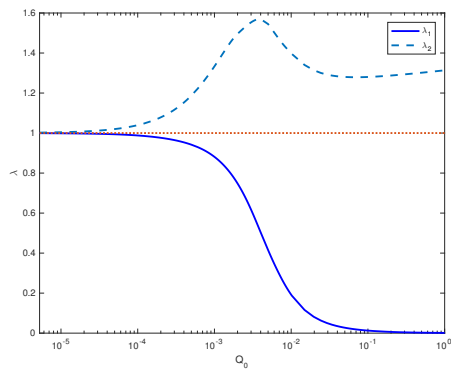
(a) $V = 10$.
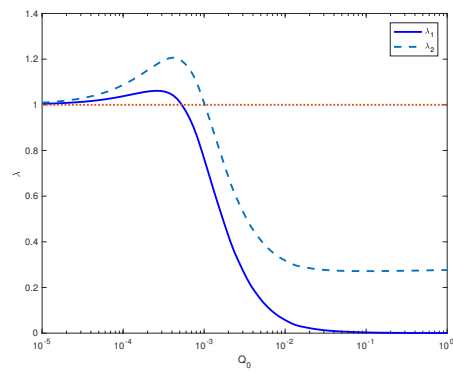
(b) $V = 50$.

(c) $V = -60$.

(d) $V = -110$.

Figure 5.1: $\lambda_1$ and $\lambda_2$ are plotted as functions of $Q_0$, with boundary values of the system (5.5) chosen as $L = 0.008$, $R = 0.001$, and $V = 10, 50, -60$, or $-110$.

- If $-18.97 < V < 18.97$, $\lambda_1 < 1 < \lambda_2$,

- If $V < -18.97$, $\lambda_1 < \lambda_2 < 1$.

These conclusions have been verified in Fig. 5.1a and Fig. 5.1d.

For large $Q_0$, the trend of $\lambda_1$ and $\lambda_2$ is an indication of the analytical works in [84]. One can relate this to Section 5.3.3 and get an insight of Fig. 5.3.

## 5.3.2    Dependence of $\lambda_1$ and $\lambda_2$ on $V$ for fixed $Q_0$

We now examine the dependence of $\lambda_1$ and $\lambda_2$ on $V$ for several fixed values of $Q_0$. In Fig. 5.2, they are plotted as functions of $V \in [-110, 40]$ for $Q = 0.0001, 0.00037, 0.00062$, and $0.04$.

We comment that $J_k = 0$ if $z_k V_k + \ln L - \ln R = 0$, independent of $Q_0$. For $L = 0.008$ and $R = 0.001$, $V_1 = -2.07944$ and $V_2 = 2.07944$. As remarked in [54], in this case, $\lambda_k(Q_0, V_k)$ should not be set to 1. Instead, the value of $\lambda_k(Q_0, V_k)$ should be determined by requiring $\lambda_k(Q_0, V)$ to be continuous at $V = V_k$ and, as expected, the value depends on $Q_0$ (see Fig. 5.2).

**Monotonicity in $V$ for small $Q_0$.** From Fig. 5.2a one can see that for very small $Q_0 = 0.0001$, $\lambda_1$ and $\lambda_2$ are monotone. This is consistent with the theoretical prediction made in [43] and the intuition that the flux ratios are dominated by the effects of $V$ when $Q_0$ is small. The $V$-intercepts with $\lambda_1$ and $\lambda_2$ are close to the theoretical values obtained in [43], i.e., $V_q^1 = 18.97$, and $V_q^2 = -18.97$ (cf. Section 5.3.1).

**Saddle-node bifurcations of $\lambda_k = 1$.** As $Q_0$ increases to $Q_0 = 0.00037$ and $0.00062$, as shown in Fig. 5.2b and Fig. 5.2c, respectively, $\lambda_1$ and $\lambda_2$ become non-monotone in $V$ and can pass the value 1 multiple times. This behavior is not predicted by the analysis in [43]. As a matter of fact, it is basically impossible to determine the arrange of $Q_0$ for which the analysis of [43] for small $Q_0$ is valid. As we will show later in Section 5.3.3, this range of $Q_0$ varies with $L$ and $R$.
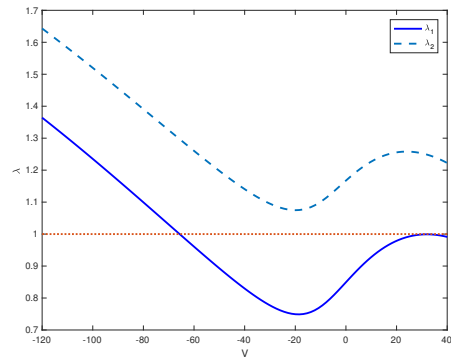
Moreover, $Q_0 = 0.00037$ for Fig. 5.2b is near a saddle-node bifurcation value for the relation $\lambda_2(V, Q_0) = 1$ in the sense that, for $Q_0 < 0.00037$, there are two values of $V$ so that $\lambda_2(V, Q_0) = 1$ while for $Q_0 > 0.00037$, there is no value of $V$ so that $\lambda_2(V, Q_0) = 1$. Similarly, $Q_0 = 0.00062$ for
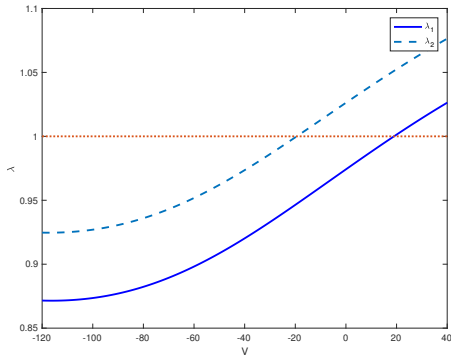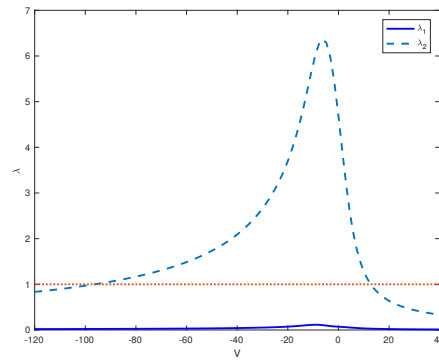
(a) $Q_0 = 0.0001$
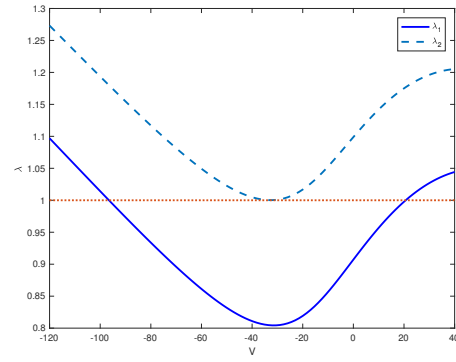
(b) $Q_0 = 0.00037$

(c) $Q_0 = 0.00062$

(d) $Q_0 = 0.04$

Figure 5.2: $\lambda_1$ and $\lambda_2$ are plotted as functions of $V$, with boundary values of the system (5.5) chosen as $L = 0.008$, $R = 0.001$, and different values of $Q_0$.

Fig. 5.2c is near a saddle-node bifurcation value for the relation $\lambda_1(V, Q_0) = 1$.

**A selectivity regime.** It is also interesting to see that in Fig. 5.2d ($Q_0 = 0.04$), $\lambda_1$ is close to zero, indicating that large positive permanent charges inhibit the flow of cation. On the other hand, for $V \in [-90, 15]$, $\lambda_2 > 1$ so the anion flux is enhanced, and otherwise, $\lambda_2 < 1$ so the anion flux is reduced (even if $Q_0$ is positive and relatively large). This observation should be compared with the behavior in Fig. 5.2c for $Q_0 = 0.00062$ where $\lambda_2 > 1$ for $V \in [-110, 40]$. Moreover, around $V = -5$, say $V \in [-15, 0]$, $\lambda_2$ is much greater than 1, which shows strong selectivity for anion.

### 5.3.3 A Complete bifurcation diagram

We now are ready to study a complete bifurcation diagram of $\lambda_1$, $\lambda_2$, interacting with $Q_0$ and $V$ together, with fixed boundary conditions, as seen in Fig. 5.3. The domain of $(Q_0, V) \in (0, 3) \times (-110, 70)$ is divided into the regions with $1 < \lambda_1 < \lambda_2$, $\lambda_1 < 1 < \lambda_2$, and $\lambda_1 < \lambda_2 < 1$. Particularly, the curves labelled with $C_1$ to $C_5$ are the parametric boundaries defined by either $\lambda_1 = 1$ or $\lambda_2 = 1$.

We first remark that Fig. 5.3 is consistent with the theoretical analysis described in Section 5.2. In particular, for small $Q_0$, the situation switches from $1 < \lambda_1 < \lambda_2$ to $\lambda_1 < 1 < \lambda_2$ as $V$ decreases and passes $V_q^1 = 18.97$ and from $\lambda_1 < 1 < \lambda_2$ to $\lambda_1 < \lambda_2 < 1$ as $V$ further decreases and passes $V_q^2 = -18.97$. This is confirmed numerically in Fig. 5.3. Moreover, we recall that $\lambda_1 = \lambda_2 = 1$ for $Q_0 = 0$ and all $V$. The numerical results show that $V \to V_q^1$ along the curves $C_1$ ($\lambda_1 = 1$) as $Q_0 \to 0$. Similarly, $V \to V_q^2$ along $C_2$ ($\lambda_2 = 1$) as $Q_0 \to 0$. Furthermore, the curves $C_1$ to $C_5$ can be treated as contour maps $\lambda_1(V, Q_0) = 1$ and $\lambda_2(V, Q_0) = 1$. Particularly, $C_1$ along with the $V$-axis makes a $\lambda_1 = 1$ contour map while $C_2$ along with the $V$-axis makes a $\lambda_2 = 1$ contour map.

As mentioned in Section 5.2, there exist critical potential values such that $V$ will converge to along the parametric boundaries $\lambda_2 = 1$. More importantly, this observation provides predictable boundaries of the range of the permanent charge that enhances $J_2$. This property has been demonstrated in Fig. 5.3. Because we have applied regularization (5.9) and (5.10), while the analytical works in [43] and [84] have been based on non-smooth permanent charges and channel shape as in (5.7) and (5.8), the critical potentials that we have obtained in computation are slightly different
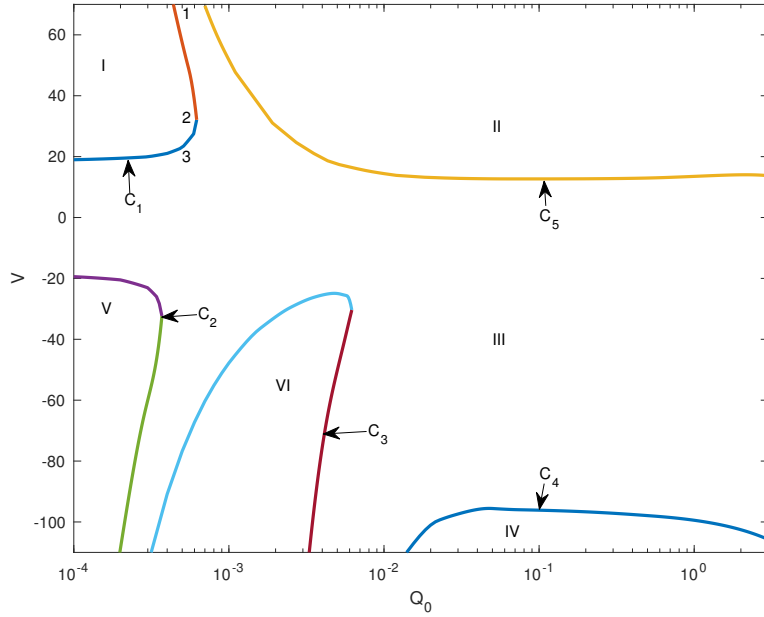
Figure 5.3: A complete bifurcation diagram for the case with the boundary conditions $L = 0.008$ and $R = 0.001$. Region I and VI: $1 < \lambda_1 < \lambda_2$; Region II, IV, and V: $\lambda_1 < \lambda_2 < 1$; Region III: $\lambda_1 < 1 < \lambda_2$.

the analytical results. We remark that it is possible to have smooth channel shape and permanent charge in practice, and Fig. 5.3 still demonstrate the limiting properties, and is a reliable reference for ion species selectivities with large permanent charge densities.

It is impressive how complexly the domain is partitioned into the regions $1 < \lambda_1 < \lambda_2$, $\lambda_1 < 1 < \lambda_3$, and $\lambda_1 < \lambda_2 < 1$. Multiple bifurcations on the curves $\lambda_1 = 1$ and $\lambda_2 = 1$ can be observed, which are consistent with the diagrams in Section 5.3.2. In fact, if we treat $\lambda_k$ as functions of the variables $Q_0$ and $V$, and the $Q - V$ space in Fig. 5.3 as a domain of the functions $\lambda_k(Q_0, V)$, Figures 5.1 and 5.2 can be treated as curves obtained by cutting through the surfaces $\lambda_k(Q_0, V)$ vertically along $Q_0$ axis direction or $V$ axis direction. For example, Fig. 5.2b essentially shows the intersecting curves of $\lambda_k(Q_0, V)$ and the plane $Q_0 = 0.00037$. Corresponding to the observation that $Q_0 = 0.00037$ is approximately the tangent line of the curve $C_5$ (on which $\lambda_2 = 1$) in Fig. 5.3, the curve $\lambda_2 = 1$ in Fig. 5.2b is tangent to the horizontal line $\lambda = 1$. In other words, with $Q_0 = 0.00037$, $\lambda_2 \geq 1$, since the line $Q_0 = 0.00037$ completely lines in a region where $\lambda_2 \geq 1$, and the equality only happens at the bifurcation near Point 5 as shown in Fig. 5.3.
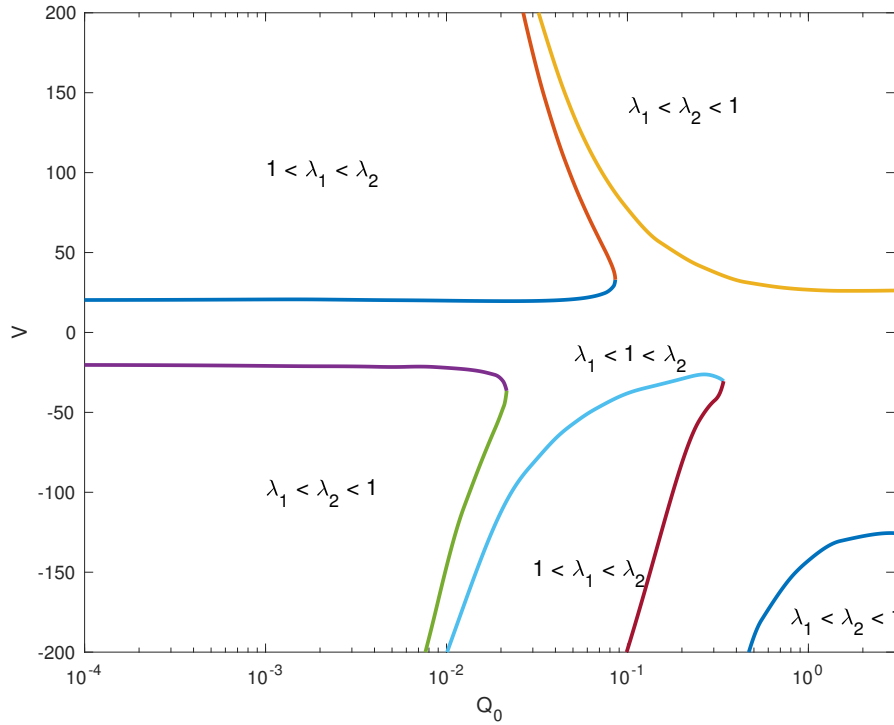
Figure 5.4: A complete bifurcation diagram for the case with the boundary conditions $L = 0.5$ and $R = 0.1$.

Further studies, both biological and mathematical, on the cause of the bifurcation are highly demanded. We remark that we have not particularly chosen any boundary values to obtain such bifurcations. Indeed, it has been observed that properties of Fig. 5.3 have been preserved with other boundary conditions. Fig. 5.4 shows the complete $Q - V$ diagram obtained with $L = 0.5$ and $R = 0.1$. Despite the difference in the quantities, one can observe the same bifurcation and limiting properties as in Fig. 5.3.

### 5.3.4  Internal dynamics and $J - V$ Relation

A reasonable approach to the cause of the bifurcations in Fig. 5.3 is to investigate the channel dynamics when the pair $(Q_0, V)$ passes the bifurcation. For this purpose, we present the numerical results of the channel dynamics at the Point 1, 2, and 3 in Fig. 5.3. However, it is very difficult to obtain an observation from the flux dynamics that could be related to the cause of the bifurcation or non-monotone features of $\lambda_k$. We look forward to any further studies on this topic.

In Fig. 5.5a-5.5c, 5.5d-5.5f, 5.5g-5.5i, and 5.5j-5.5l, we present the flux and the current, the electrochemical potential, the concentration of each species, and the electric potential, respectively, at Point 1 $(0.0005, 67)$, Point 2 $(0.0005, 33)$, and Point 3 $(0.0005, 20)$ in Fig. 5.3. One can observe from Fig. 5.3 that these three points are on a path where $\lambda_1$ is first less than 1, then greater than 1, then less than 1 again.

In Fig. 5.5a-5.5c, we have observed that as $V$ increases, both the positive and negative species are enhanced. While we know that $\lambda_1 > 1$ at Point 2 while $\lambda_1 < 1$ at Point 1 and 3, this trend is not demonstrated in the trend of the flux. To further study the trend of the flux-$V$ relation, we present the plots of $J_1$ and $J_2$ as functions of $V$ in Fig. 5.6a and Fig. 5.6b, where $Q_0 = 5 \times 10^{-4}$ and 0.003, respectively. We can see that for small $Q_0$ value such as $Q_0 = 5 \times 10^{-4}$, the fluxes are almost linear in $V$. However, as we increase $Q_0$ to $Q_0 = 0.003$, the fluxes are not linear in $V$, as shown in Fig. 5.6b. This observation is consistent to the linear $I - V$ relation for small permanent charge densities and the saturation effect for large permanent charge densities. Moreover, because $J_1$ and $J_2$ are linear when $Q_0 = 0$, the nonlinearity as shown in Fig. 5.6b is consistent to the fact that $\lambda_1$ and $\lambda_2$ are not monotone with respect to $V$.

In Fig. 5.5d-5.5f, we observe that the voltage enhances the electrochemical potentials of both species. In Fig. 5.5g-5.5i and Fig. 5.5j-5.5l, sharp layers of $\phi$ and $c_k$ are demonstrated at the edge of neck of the channel.

### 5.3.5 The Hard-Sphere Case

So far we have treated ions as permanent charges and assumed the excess component $\mu_k^{ex} = 0$. However, ions have positive volumes, and can have large influence on channel selectivity especially when they have large sizes and density. The excess potential $\mu_k^{ex}$ typically contains two components: the hard-sphere component $\mu_k^{HS}$ and the excess electrostatic component. In this section, we apply a Local Hard Sphere (LHS) PNP model [68], derived by taking Taylor expansions of the excess chemical potential of the Hard-Sphere(HS) model, which has been obtained based on Rosenfeld's fundamental measure theory (FMT) [70].
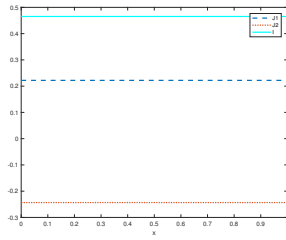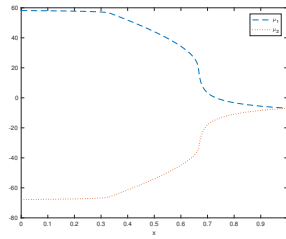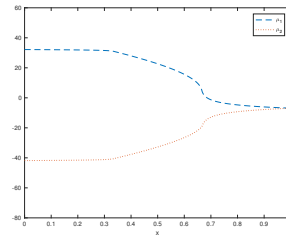
(a) $J_1$, $J_2$, and $I$ at Point 1 in Fig. 5.3.
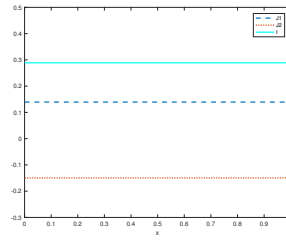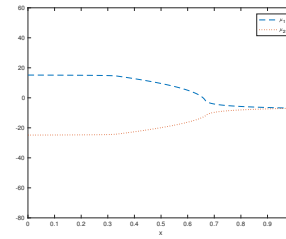
(b) $J_1$, $J_2$, and $I$ at Point 2 in Fig. 5.3.
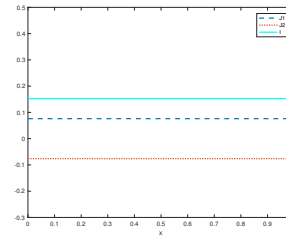
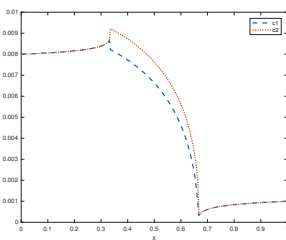(c) $J_1$, $J_2$, and $I$ at Point 3 in Fig. 5.3.

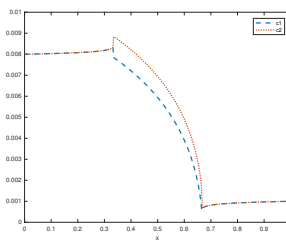(d) $\mu_1$ and $\mu_2$ at Point 1 in Fig. 5.3.

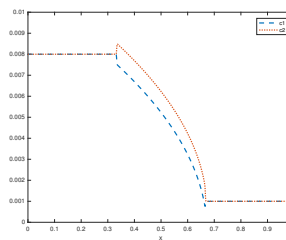(e) $\mu_1$ and $\mu_2$ at Point 2 in Fig. 5.3.

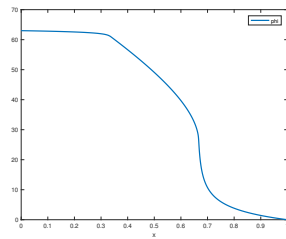(f) $\mu_1$ and $\mu_2$ at Point 3 in Fig. 5.3.

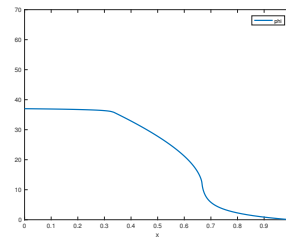(g) $c_1$ and $c_2$ at Point 1 in Fig. 5.3.

(h) $c_1$ and $c_2$ at Point 2 in Fig. 5.3.
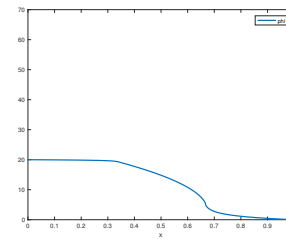
(i) $c_1$ and $c_2$ at Point 3 in Fig. 5.3.

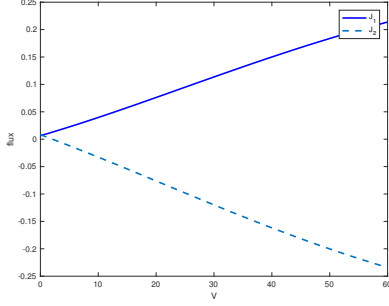(j) $\phi$ at Point 1 in Fig. 5.3.

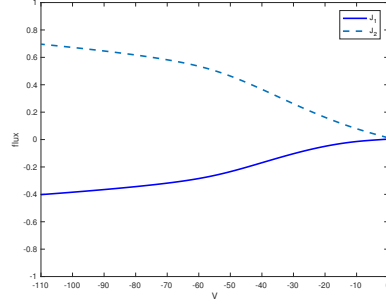(k) $\phi$ at Point 2 in Fig. 5.3.

(l) $\phi$ at Point 3 in Fig. 5.3.

Figure 5.5: Internal dynamics at Point 1 $(0.0005, 67)$, Point 2 $(0.0005, 33)$, and Point 3 $(0.0005, 20)$ in Fig. 5.3.

(a) $Q_0 = 5 \times 10^{-4}$.

(b) $Q_0 = 0.003$.

Figure 5.6: $J_1$ and $J_2$ as functions of $V$ with $Q_0 = 5 \times 10^{-4}$ and $Q_0 = 0.003$.

We now have

$$\bar{\mu}_k = \mu_k^{id} + \mu_k^{LHS},$$

where $\mu_k^{LHS}$ is given by

$$
\begin{aligned}
\mu_k^{LHS}(x) = &-\ln\left(1 - \Sigma_j \frac{4}{3}\pi R_j^3 c_j(x)\right) + \frac{R_k \Sigma_j 4\pi R_j^2 c_j(x)}{1 - \Sigma_j \frac{4}{3}\pi R_j^3 c_j(x)} \\
&+ \frac{4\pi R_k^2 \Sigma_j R_j c_j(x)}{1 - \Sigma_j \frac{4}{3}\pi R_j^3 c_j(x)} + \frac{4}{3}\pi \frac{R_k^3 \Sigma_j c_j(x)}{1 - \Sigma_j \frac{4}{3}\pi R_j^3 c_j(x)},
\end{aligned}
\tag{5.19}
$$

where $R_1$ and $R_2$ are the radii of the three-dimensional hard sphere particle of the species.

In Fig. 5.7b, we present the $Q - V$ bifurcation diagram with boundary conditions $L = 0.008$ and $R = 0.001$ and the radii of the species chosen as $R_1 = 0.2$ and $R_2 = 0.4$. Fig. 5.7b is almost identical to Fig. 5.7a, which is associated to $\mu^{ex} = 0$. If we change the boundary conditions to be $L = 0.5$ and $R = 0.1$, and compare the $Q - V$ bifurcation diagrams obtained with and without excess component, we can easily observe difference in quantities, but same bifurcation properties, as shown in Fig. 5.8. This result is expectable, since when concentration is large, more collision will happen between ions, in which case the effects of the ion sizes play a more important role.

To quantify the effects of the ion sizes, we present the plots of the term $\Sigma_j \frac{4}{3}\pi R_j^3 c_j(x)$, the ideal component $\mu_k^{id}$, and the excess component $\mu_k^{ex}$, in Fig. 5.9 and Fig. 5.10, with different boundary conditions. As one can observe, $\Sigma_j \frac{4}{3}\pi R_j^3 c_j(x)$ is almost negligible compared to 1 in Fig. 5.9a, with $L = 0.008$, $R = 0.001$, $V = 30$, and $Q_0 = 0.05$, and is relatively large in Fig. 5.10a, where
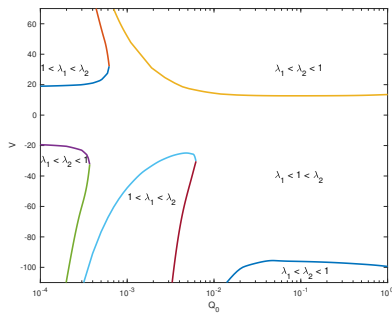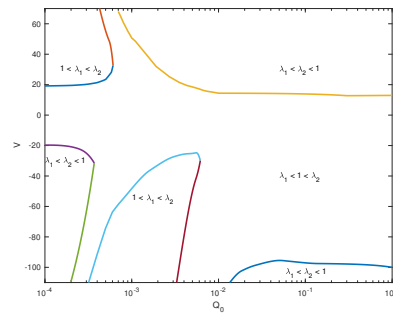
(a) $\mu^{ex} = 0$        (b) $\mu^{ex}$ chosen as in (5.19)

Figure 5.7: Comparison of bifurcation diagrams with $\mu^{ex} = 0$ and $\mu^{ex}$ chosen as in (5.19), with $L = 0.008$ and $R = 0.001$.



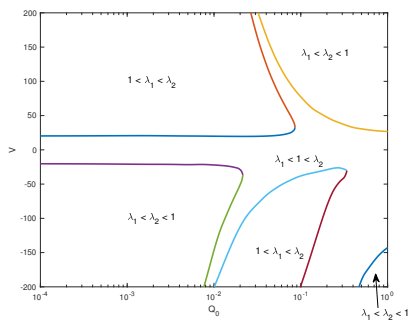(a) $\mu^{ex} = 0$        (b) $\mu^{ex}$ chosen as in (5.19)
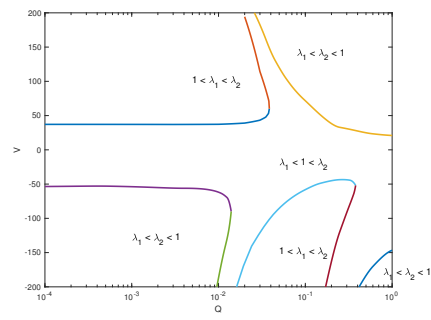
Figure 5.8: Comparison of bifurcation diagrams with $\mu^{ex} = 0$ and $\mu^{ex}$ chosen as in (5.19), with $L = 0.5$ and $R = 0.1$.

$L = 0.5$, $R = 0.1$, $V = 30$, and $Q_0 = 1$. As a result, $\mu_k^{ex}$ in Fig. 5.9c is small compared to the ideal component $\mu_k^{id}$ as shown in Fig. 5.9b, and not making a significant difference in the flux ratio. As a contrast, $\mu_k^{ex}$ in Fig. 5.10c is relatively large, correspondingly, with the same boundary conditions $L = 0.5$ and $R = 1$, one can observe that the LHS term has made a difference in the flux ratio diagram, as shown in Fig. 5.8. A great deal of efforts have been made on deriving the excess
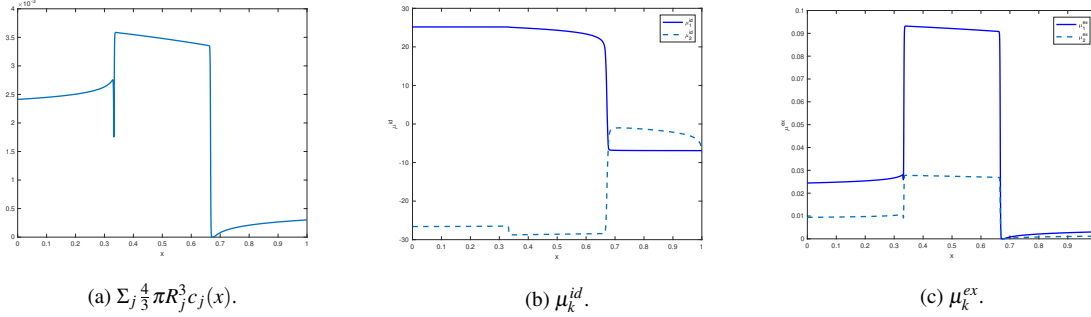


(a) $\Sigma_j \frac{4}{3}\pi R_j^3 c_j(x)$.      (b) $\mu_k^{id}$.      (c) $\mu_k^{ex}$.

Figure 5.9: $\Sigma_j \frac{4}{3}\pi R_j^3 c_j(x)$, $\mu_k^{id}$ and $\mu_k^{ex}$, with $L = 0.008$, $R = 0.001$, $V = 30$, and $Q_0 = 0.05$.



(a) $\Sigma_j \frac{4}{3}\pi R_j^3 c_j(x)$.      (b) $\mu_k^{id}$.      (c) $\mu_k^{ex}$.
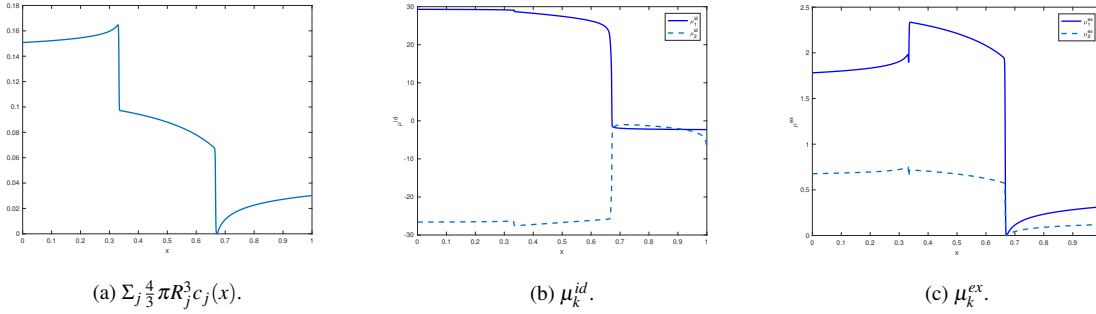
Figure 5.10: $\Sigma_j \frac{4}{3}\pi R_j^3 c_j(x)$, $\mu_k^{id}$ and $\mu_k^{ex}$, with $L = 0.5$, $R = 0.1$, $V = 30$, and $Q_0 = 1$.

component $\mu^{ex}$. The uniform size modified Poisson-Boltzmann (SMPB) equation has been brought up in. Modeling of the excess electrostatic component component $\mu_k^{ex}$ is rather challenging, and various approximations have been obtained [7, 8, 18, 21].

## 5.4 Conclusions

In this chapter, we have studied the effects of permanent charge along with boundary conditions on ionic flows, via a quasi one-dimensional PNP model. We have given a complete diagram, divided

into different regions of the permanent charge density and the boundary condition of the electrical potential, that have verified and connected the existing analytical results. We have observed unexpected bifurcations, which might be useful reference in practice, and hopefully will bring up interesting objects for the future studies. Moreover, we have provided the bifurcation diagrams corresponding to the quasi one-dimensional PNP model with the LHS (local hard sphere) modeling of the excess electrochemical potential. Same bifurcation properties and difference in quantities have been observed. The MMPDE strategy has been applied in purpose of resolving the discontinuity of the solutions at endpoints of the "neck" of the channel. It remains an open question how the bifurcations have been generated, and further studies in mathematics as well as biology are highly demanded.

# Chapter 6

# Conclusions and Future Work

In this work, we have described the mathematical characterization, as well as detailed formulation and numerical integration of the MMPDE method. The MMPDE method is a PDE based adaptive mesh method that is used to properly treat the sharp fronts that occur in the solutions of differential equations. It has been shown that the MMPDE method has the advantage of not requiring a large mesh size, adaptively relocating the mesh elements to sharp fronts of the solution and thus increasing the accuracy, as well as stable non-singularity in regular and even non-convex and non-simply connected domains. As examples of application of the MMPDE method, three models arising from the physical background as well as image segmentation have been investigated.

The Ambrosio-Tortorelli functional is a phase-field approximation of the Mumford Shah functional, which has been proposed as a variational approach to image segmentation. We have presented an asymptotic analysis to investigate the influence of the regularization parameter to the segmentation capability of this functional, based on which a practical parameter selection strategy for numerical computation has been derived. This approach can be used as an image preprocessing tool, and is good at dealing with complicated images with high level noise. One possible improvement is to couple this strategy with a procedure of labelling the objects in the objective image. Moreover, the Ambrosio-Tortorelli functional is a special example of phase-field models, and we hope that the analysis and the selection strategy for the regularization parameter can apply to the underway phase-field investigations.

The MMPDE method has been applied to investigate the contact sets of the micro-electro mechanical systems (MEMS), which has verified the asymptotic analysis developed to locate the possible contact sets as described in Section 4.2. In order to improve the accuracy of the solution,

as well as the performance of the MMPDE method in general, future studies could be carried on to investigate the strategies of moving mesh nodes along curvy boundaries. Moreover, studies on different types of micro-electro mechanical systems can be interesting and highly desired in the nanotechnology industry.

We have carried on a numerical investigation of the influence of permanent charge density along with voltage on flux ratios. The flux ratio has been brought up to quantify the effects of the permanent charge on the flux selectivity in an ion channel. Our numerical results as shown in Section 5.3 validate the existing analytical results, for both small and large permanent charge densities. More importantly, we take the advantage of numerical approach, to bridge the two extrema and get a general characterization of the flux ratio, in order to fully understand and quantify the flux selectivity. We have observed the occurrence of bifurcations in the diagram of the flux ratios. Studies on the cause of such bifurcations are highly desired.

# References

[1] L. Ambrosio and V. M. Tortorelli. On the approximation of free discontinuity problems. *Boll. Un. Mat. Ital. B*, 6:105–123, 1992.

[2] M. J. Baines. *Moving Finite Elements*. Oxford University Press, Oxford, 1994.

[3] M. J. Baines, M. E. Hubbard, and P. K. Jimack. Velocity-based moving mesh methods for nonlinear partial differential equations. *Comm. Comput. Phys.*, 10:509–576, 2011.

[4] V. Barcilon. Ion flow through narrow membrane channels: Part I. *SIAM J. Appl. Math.*, 52: 1391- 1404, 1992.

[5] R. C. Batra, M. Porfiri, and D. Spinello. Review of modeling electrostatically actuated microelectromechanical systems. *Smart Mater. Struct.*, 16:R23–R31, 2007.

[6] G. Bellettini and A. Coscia. Discrete approximation of a free discontinuity problem. *Numer. Funct. Anal. Optim.*, 15:201–224, 1994.

[7] L. Blum. Mean spherical model for asymmetric electrolytes. *Mol. Phys.*, 30: 1529-1535, 1979.

[8] L. Blum and J. S. Høye. Mean spherical model for asymmetric electrolytes. 2. Thermodynamic properties and the pair correlation function. *J. Phys. Chem.*, 81: 1311- 1316, 1977.

[9] B. Bourdin, G. A. Francfort, and J. J. Marigo. Numerical experiments in revisited brittle fracture. *J. Mech. Phys. Solids*, 48:797–826, 2000.

[10] C. J. Budd, V. Galaktionov, and J. F. Williams. Self-similar blow-up in higher-order semilinear parabolic equations. *SIAM J. Appl. Math.*, 64:1775–1809, 2004.

[11] C. J. Budd, W. Huang, and R. D. Russell. Adaptivity with moving grids. *Acta Numer.*, 18:111–241, 2009.

[12] C. J. Budd and J. F. Williams. Parabolic Monge-Ampére methods for blow-up problems in several spatial dimensions, *J. Phys. A*, 39:5425–5444, 2006.

[13] C. J. Budd and J. F. Williams. Moving Mesh Generation Using the Parabolic Monge-Ampére Equation, *SIAM J. Sci. Comput.*, 31:3438–3465, 2009.

[14] C. J. Budd and J. F. Williams. How to adaptively resolve evolutionary singularities in differential equations with symmetry *J. Eng. Math.*, 66:217–236, 2010.

[15] H, D. Ceniceros and Thomas Y. Hou. An efficient dynamically adaptive mesh for potentially singular solutions, *J. Comput. Phys.*, 172:609–639, 2001.

[16] K. L. DiPietro and A. E. Lindsay. Monge-Ampére simulation of fourth order PDEs in two dimensions with application to elastic-electrostatic contact problems. *J. Comput. Phys.*, 349:328–350, 2017.

[17] E. De Giorgi, M. Carriero, and A. Leaci. Existence theorem for a minimum problem with free discontinuity set. *Arch. Rational Mech. Anal.*, 108:195–218, 1989.

[18] H. T. Davis. *Statistical Mechanics of Phases, Interfaces, and Thin Films.* VCH Publishers, New York, 1996.

[19] B. Eisenberg and W. Liu, Poisson-Nernst-Planck systems for ion channels with permanent charges. *SIAM J. Math. Anal.* **38** (2007), 1932-1966.

[20] B. Eisenberg, W. Liu, and H. Xu, Reversal permanent charge and reversal potential: case studies via classic Poisson- Nernst- Planck models. *Nonlinearity* **28** (2015), 103–127.

[21] A. Ern, R. Joubaud, and T. Lelièvre. Mathematical study of non-ideal electrostatic correlations in equilibrium electrolytes. *Nonlinearity.*, 25: 1635- 1652, 2012.

[22] L. C. Evans. *Partial Differential Equations*. American Mathematical Society, Providence, Rhode Island, 1998. Graduate Studies in Mathematics, Volume 19.

[23] X. Feng and A. Prohl. Analysis of gradient flow of a regularized Mumford-Shah functional for image segmentation and image inpainting. *M2AN Math. Model. Numer. Anal.*, 38:291–320, 2004.

[24] G. A. Francfort and J. J. Marigo. Revisiting brittle fracture as an energy minimization problem. *J. Mech. Phys. Solids*, 46:1319–1342, 1998.

[25] A. Friedman and L. Oswald. The blow-up time for higher order semilinear parabolic equations with small leading coefficients. *J. Diff. Eq.*, 75:239–263, 1988.

[26] V. Galaktionov. Five types of blow-up in a semilinear fourth-order reaction-diffusion equation: an analytical-numerical approach. *Nonlinearity*, 22:1695–1741, 2009.

[27] V. A. Galaktionov and J.-L. Vázquez. The problem of blow-up in nonlinear parabolic equations. *Dis. Cont. Dyn. Sys.*, 8:399–433, 2002.

[28] S. González-Pinto, J. I. Montijano, and S. Pérez-Rodríguez. Two-step error estimators for implicit Runge-Kutta methods applied to stiff systems. *ACM Trans. Math. Software*, 30:1–18, 2004.

[29] E. Hairer and G. Wanner. *Solving Ordinary Differential Equations. II*, Volume 14 of *Springer Series in Computational Mathematics*. Springer-Verlag, Berlin, second edition, 1996. Stiff and differential-algebraic problems.

[30] A. L. Hodgkin and R. D. Keynes, The potassium permeability of a giant nerve fibre. *J. Physiol.* 128: 61-88, 1995.

[31] T.-L. Horng, T.-C. Lin, C. Liu, and B. Eisenberg, PNP Equations with Steric Effects: A Model of Ion Flow through Channels. *J. Phys. Chem. B* 116: 11422-11441, 2012.

[32] W. Huang. Variational mesh adaptation: isotropy and equidistribution. *J. Comput. Phys.*, 174:903–924, 2001.

[33] W. Huang. Metric tensors for anisotropic mesh generation. *J. Comput. Phys.*, 204:633–665, 2005.

[34] W. Huang and L. Kamenski. A geometric discretization and a simple implementation for variational mesh generation and adaptation. *J. Comput. Phys.*, 301:322–337, 2015.

[35] W. Huang and L. Kamenski. On the mesh nonsingularity of the moving mesh PDE method. *Math. Comp.*, in press. (DOI: 10.1090/mcom/3271)

[36] W. Huang and R. D. Russell. *Adaptive Moving Mesh Methods*. Springer, New York, 2011. Applied Mathematical Sciences Series, Vol. 174.

[37] Y. Hyon, J. Fonseca, B. Eisenberg, and C. Liu, A new Poisson-Nernst-Planck equation (PNP-FS-IF) for charge inversion near walls. *Biophys. J.* , 100: 578a, 2011.

[38] Y. Hyon, B. Eisenberg, and C. Liu, A mathematical model for the hard sphere repulsion in ionic solutions. *Commun. Math. Sci.* 9: 459-475, 2010.

[39] Y. Hyon, J. Fonseca, B. Eisenberg, and C. Liu, Energy variational approach to study charge inversion (layering) near charged walls. *Discrete Contin. Dyn. Syst. Ser. B.*, 17: 2725-2743, 2012.

[40] Y. Hyon, B. Eisenberg, and C. Liu. An energetic variational approach to ion channel dynamics. *Math. Methods Appl. Sci.*, 37: 952-961, 2014.

[41] Y. Hyon, J. Fonseca, B. Eisenberg, and C. Liu, Energy variational approach to study charge inversion (layering) near charged walls. *Discrete Contin. Dyn. Syst. Ser. B* 17: 2725-2743, 2012.

[42] S. Ji, B. Eisenberg, and W. Liu, Flux Ratios and Channel Structures. *J. Dynam. Differential Equations*, to appear (Online ID: DOI 10.1007/s10884-017-9607-1).

[43] S. Ji, W. Liu, and M. Zhang. Effects of (small) permanent charge and channel geometry on ionic flows via classical Poisson-Nernst-Planck models. *SIAM J. Appl. Math*, 75: 114-135, 2015.

[44] R. Kobayashi. Modeling and numerical simulations of dendritic crystal growth. *Physica D*, 63:410–423, 1993.

[45] S. Krylov and N. Dick. Dynamic stability of electrostatically actuated initially curved shallow micro beams. *Continuum Mech. Therm.*, 22:445–468, 2010.

[46] S. Krylov, B. R. Ilic, and S. Lulinsky. Bistability of curved microbeams actuated by fringing electrostatic fields. *Nonlinear Dyn.*, 66:403–426, 2011.

[47] S. Krylov, B. R. Ilic, D. Schreiber, S. Seretensky, and H. Craighead. The pull-in behavior of electrostatically actuated bistable microstructures. *J. Micromech. Microeng.*, 18:055026, 2008.

[48] F. Lin and Y. Yang. Nonlinear non-local elliptic equation modelling electrostatic actuation. *Proc. R. Soc. London Ser. A*, 463:1323–1337, 2007.

[49] A. E. Lindsay. An asymptotic study of blow up multiplicity in fourth order parabolic partial differential equations. *Dis. Cont. Dyn. Sys. Ser. B*, 19:189–215, 2014.

[50] A. E. Lindsay. Regularized model of post-touchdown configurations in electrostatic MEMS: bistability analysis. *J. Eng. Math.*, 99:65–77, 2016.

[51] A. Lindsay and J. Lega. Multiple quenching solutions of a fourth order parabolic pde with a singular nonlinearity modeling a MEMS capacitor. *SIAM J. Appl. Math.*, 72:935–958, 2012.

[52] A. Lindsay, J. Lega, and K. Glasner. Regularized model of post-touchdown configurations in electrostatic MEMS: Equilibrium analysis. *Physica D*, 280/281:95–108, 2014.

[53] A. E. Lindsay, J. Lega, and F. J. Sayas. The quenching set of a MEMS capacitor in two-dimensional geometries. *J. Nonlinear Sci.*, 23:807–834, 2013.

[54] W. Liu, A flux ratio and a universal property of permanent charges effects on fluxes. *Comput. Math. Biophys.* **6** (2018), 28-40.

[55] W. Liu, One-dimensional steady-state Poisson-Nernst-Planck systems for ion channels with multiple ion species. *J. Differential Equations* **246** (2009), 428-451.

[56] C. Liu and J. Shen. A phase field model for the mixture of two incompressible fluids and its approximation by a Fourier-spectral method. *Phys. D*, 179:211–228, 2003.

[57] W. Liu and B. Wang. Poisson-Nernst-Planck systems for narrow tubular-like membrane channels. *J. Dynam. Differential Equations*, 22: 413-437, 2010.

[58] G. Malandain and S. Fernández-Vidal. Euclidean skeletons. *Image Vis. Comput.*, 16:317–327, 1998.

[59] S. May, J. Vigonellet, and R. de Borst. A numerical assessment of phase-field models for brittle and cohesive fracture: Γ-covergence and stress oscillations. *European J. Mech. A/Solids.*, 52:72–84, 2015.

[60] C. Miehe, F. Welschinger, and M. Hofacker. Thermodynamically consistent phase-field models of fracture: Variational principles and multi-field FE implementations. *Int. J. Numer. Meth. Eng.*, 83:1273–1311, 2010.

[61] D. Mumford and J. Shah. Optimal approximations by piecewise smooth functions and associated variational problems. *Commun. Pure Appl. Math*, 42:577–685, 1989.

[62] W. Nonner and R. S. Eisenberg. Ion permeation and glutamate residues linked by Poisson-Nernst-Planck theory in L-type Calcium channels. *Biophys. J.*, 75: 1287-1305, 1998.

[63] T. T. Nguyen, J. Yvonnet, M. Bornert, C. Chateau, K. Sab, R. Romani, and R. Le Roy. On the choice of parameters in the phase field method for simulating crack initiation with experimental validation. *Int J Fract*, 197:213–226, 2016.

[64] J. A. Pelesko. Mathematical modeling of electrostatic MEMS with tailored dielectric proper-ties. *SIAM J. Appl. Math.*, 62:888–908, 2002.

[65] J. A. Pelesko and D. H. Bernstein. *Modeling MEMS and NEMS*, Chapman Hall and CRC Press, 2002.

[66] K. Pham, H. Amor, J.-J. Marigo, and C. Maurini. Gradient damage models and their use to approximate brittle fracture. *Int. J. Damage Mech.*, 20:618–652, 2011.

[67] G. A. Philippin. Blow-up phenomena for a class of fourth-order parabolic problems. *Proc. Amer. Math. Soc.*, 143:2507–2513, 2015.

[68] Yu Qiao, Xuejiao Liu, Minxin Chen, and Benzhuo Lu. A Local Approximation of funda-mental measure theory incorporated into three dimensional Poisson-Nernst-Planck equations to account for hard sphere repulsion among Ions. *J Stat Phys.*, 163:156-174, 2016.

[69] J. Qiu, J. H. Lang, and A. H. Slocum. A curved-beam bistable mechanism. *J. Microelec-tromech. Syst.*, 13:137–146, 2004.

[70] Y. Rosenfeld. Free-energy model for inhomogeneous hard-sphere fluid mixture and density-functional theory of freezing. *Phys. Rev. Lett.*, 63: 980-983, 1989.

[71] Courtesy of Sandia National Laboratories, SUMMiT(TM) Technologies,
`www.mems.sandia.gov`.

[72] Z. Schuss, B. Nadler, and R. S. Eisenberg. Derivation of Poisson and Nernst-Planck equations in a bath and channel from a molecular model. *Phys. Rev. E*, 64: 1- 14, 2001.

[73] J. Shen and X. Yang. Decoupled energy stable schemes for phase-field models of two-phase complex fluids. *SIAM J. Sci. Comput.*, 36:B122–B145, 2014.

[74] J. Shen, X. Yang, and H. Yu. Efficient energy stable numerical schemes for a phase field moving contact line model. *J. Comput. Phys.*, 284:617–630, 2015.

[75] T. Tang. Moving mesh methods for computational fluid dynamics flow and transport. In *Recent Advances in Adaptive Computation (Hangzhou, 2004)*, Volume 383 of *AMS Contemporary Mathematics*, pages 141–173. Amer. Math. Soc., Providence, RI, 2005.

[76] N.-C. Tsai and C.-Y. Sue. Review of MEMS-based drug delivery and dosing systems. *Sens. Actuators A Phys.*, 134:555–564, 2007.

[77] J. T. M. van Beek and R. Puers. A review of MEMS oscillators for frequency reference and timing applications. *J. Micromech. Microeng.*, 22:013001, 2012.

[78] H. H. Ussing, The distinction by means of tracers between active transport and diffusion. *Acta Physiol. Scand.* 19: 43-56, 1949.

[79] J. Vignollet, S. May, R. de Borst, and C. V. Verhoosel. Phase-field models for brittle and cohesive fracture. *Meccanica*, 49:2587–2601, 2014.

[80] A. A. Wheeler, B. T. Murray, and R. J. Schaefer. Computation of dendrites using a phase field model. *Physica D*, 66:243–262, 1993.

[81] T. P. Witelski and A. J. Bernoff. Dynamics of three-dimensional thin film rupture. *Phys. D*, 147:155–176, 2000.

[82] G. W. Wei, Q. Zheng, Z. Chen, and K. Xia, Variational multiscale models for charge transport. *SIAM Review* 54: 699-754, 2012.

[83] X. Yang, J. J. Feng, C. Liu, and J. Shen. Numerical simulations of jet pinching-off and drop formation using an energetic variational phase-field method. *J. Comput. Phys.*, 218:417–428, 2006.

[84] L. Zhang, B. Eisenberg, and W. Liu, An effect of large permanent charge: Decreasing flux with increasing transmembrane potential. *Euro. Phys. J. Special Topics*, accepted.

[85] R. Zhang and L. Cai. On the semi linear equations of electrostatic NEMS devices. *Z. Angew. Math. Phys.*, 65:1207–1222, 2014.